REVIEW

NANO · MICRO small

www.small-journal.com

Nanoparticle Assembly: From Self-Organization to Controlled Micropatterning for Enhanced Functionalities

*Sayli Jambhulkar, Dharneedar Ravichandran, Yuxiang Zhu, Varunkumar Thippanna, Arunachalam Ramanathan, Dhanush Patil, Nathan Fonseca, Sri Vaishnavi Thummalapalli, Barath Sundaravadivelan, Allen Sun, Weiheng Xu, Sui Yang, Arunachala Mada Kannan, Yuval Golan, Jessica Lancaster, Lei Chen, Erina B. Joyee, and Kenan Song**

Nanoparticles form long-range micropatterns via self-assembly or directed self-assembly with superior mechanical, electrical, optical, magnetic, chemical, and other functional properties for broad applications, such as structural supports, thermal exchangers, optoelectronics, microelectronics, and robotics. The precisely defined particle assembly at the nanoscale with simultaneously scalable patterning at the microscale is indispensable for enabling functionality and improving the performance of devices. This article provides a comprehensive review of nanoparticle assembly formed primarily via the balance of forces at the nanoscale (e.g., van der Waals, colloidal, capillary, convection, and chemical forces) and nanoparticle-template interactions (e.g., physical confinement, chemical functionalization, additive layer-upon-layer). The review commences with a general overview of nanoparticle self-assembly, with the state-of-the-art literature review and motivation. It subsequently reviews the recent progress in nanoparticle assembly without the presence of surface templates. Manufacturing techniques for surface template fabrication and their influence on nanoparticle assembly efficiency and effectiveness are then explored. The primary focus is the spatial organization and orientational preference of nanoparticles on non-templated and pre-templated surfaces in a controlled manner. Moreover, the article discusses broad applications of micropatterned surfaces, encompassing various fields. Finally, the review concludes with a summary of manufacturing methods, their limitations, and future trends in nanoparticle assembly.

1. Introduction

Nanoparticles (NPs) have captured considerable interest due to their exceptional properties and diverse applications in the field of nanotechnology. Achieving multifunctionality requires the precise assembly of nanoparticles onto surfaces and interfaces in well-organized patterns.[1] The NP's functional properties may depend on their size, shape, patterns, and surface functionalities to utilize their full potential to produce high-performance materials. For example, zero-dimensional (0D) NPs (e.g., nanospheres (NS), nanodots), one-dimensional (1D) NPs (e.g., nanorods (NRs), nanowires (NWs), nanotubes (NTs)), and two-dimensional (2D) NPs (e.g., nanoflakes and nanosheets) display intriguing functional properties including mechanical strength, thermal dissipation, electrical conductivity, and optical properties.[2–6] Thus, NPs create unique nanodevices and nanosystems suitable for applications in diverse fields, such as structural protection, thermal energy management,[7,8] microelectronics,[9,10] metasurfaces,[11,12] quantum science,[13,14] nanorobotics,[15,16] and pharmaceutical

---

S. Jambhulkar, W. Xu
Systems Engineering
School of Manufacturing Systems and Networks (MSN)
Ira A. Fulton Schools of Engineering
Arizona State University (ASU)
Mesa, AZ 85212, USA

The ORCID identification number(s) for the author(s) of this article can be found under https://doi.org/10.1002/smll.202306394

DOI: 10.1002/smll.202306394

D. Ravichandran, Y. Zhu, V. Thippanna, A. Ramanathan, D. Patil, N. Fonseca, S. V. Thummalapalli
Manufacturing Engineering
School of Manufacturing Systems and Networks (MSN)
Ira A. Fulton Schools of Engineering
Arizona State University (ASU)
Mesa, AZ 85212, USA
B. Sundaravadivelan
Department of Mechanical and Aerospace Engineering
School for Engineering of Matter, Transport & Energy
Ira A. Fulton Schools of Engineering
Arizona State University (ASU)
Tempe, AZ 85281, USA

engineering.[17–19] However, discontinuous, disordered, powder-like NPs do not display their theoretical properties during practical applications.[1–3] Thus, long-range ordered structures are mandatory to exploit the functional properties of NPs in practical products and systems.

As one solution for ordered structures, self-assembly and directed self-assembly can form complex and functional architectures from smaller subunits to a wide range of dimensions from 10 nm to a few centimeters. Nanoparticle assembly arises from the interplay of particle-particle interactions (such as depletion attraction, capillary forces, dipole-dipole attraction, or their combinations) and particle-environment interactions (including physical confinement and external field manipulations). These interactions work together to achieve thermodynamic equilibrium and minimize the overall energy of the system.[21–24] In addition, these nanoparticle assembly methods have the capacity for precise positioning and preferential orientation essential for high-performance applications where packing periodicity and special alignment affect property and functionality.[25–27] Although effective in nanoscale morphology control, self-assembly still has a few challenges, such as balancing surface patterning scalability with acceptable processing precisions, fabrication rates, defect control, and nanosystem property maintenance or in-situ quality management.[28] Different approaches involving a variety of materials and techniques, such as general NPs, DNA,[29,30] or functional polymers[31,32] organized via external fields,[26,33,34] patterned templates,[35,36] fluidic flow,[24,37,38] surface modification,[39,40] and NPs interactions,[20,41] have been successfully utilized to fabricate 1D, 2D, and 3D complex structures assembled from various NPs. However, conventional processing usually accumulates defects with increased material or structure size that will deteriorate device properties.

The template-based directed assembly (TDA) can effectively eliminate or minimize random or defective structures. The interactions between the NPs and the template lead to the arrangement of NPs into predefined structures depending on the shape of the templates (**Figure 1**). A broad range of objects serving as scaffolds (e.g., 1D, 2D, and 3D confined environments to anchor carbon nanotubes (CNT),[42,43] block copolymers (BCP),[32,44] viruses,[45–47] liquid crystals,[48,49]l and DNA molecules[30,50]) can be used as templates for NPs organization. Small molecules contain a limited number of deposition sites while soft macromolecules are too compliant to environmental influences, which may cause the NP aggregation. Thus, their utilization as a template in scalable processing is challenging. As a comparison, hard and rigid templates are more applicable for TDA because of their capability for defined structure of assembly for large-area patterning with controlled periodicity. Different nanomanufacturing methods for template manufacturing include lithography-based writing and etching (e.g., electron beam lithography (EBL),[51,52] ion beam lithography,[53] optical lithography (OL),[54,55] soft lithography,[56,57] direct write lithography, nanoimprint lithography)[58] and vapor deposition-based protocols (e.g., physical vapor deposition (PVD), chemical vapor deposition (CVD),[59] atomic layer deposition (ALD),[60] plasma-enhanced CVD [61]). These methods can generate high-resolution (down to <10 nm) features with either high precisions or structural diversity. Additionally, a wide variety of other techniques, such as 3D printing,[62] micro-molding,[63] polymer grafting,[64] and wrinkling,[65] are studied for template fabrication. Therefore, the self-assembly and multiscale pattern formation of NPs on top of or within hard templates (e.g., confined geometries, interfaces) are also described in this work.

Although there are some literature reviews in the nanoparticle assembly field, there have not been many focusing on the surface template effects on nanoparticle assembly, especially the enabling techniques of template generation, the combinational template effects in NP processing methods, or the practical applications above the microscale. For example, i) Y. Li et al. summarized the nanoparticle assembly only at liquid-air interfaces,[66] ii) T.P. Russell et al. reviewed the nanoparticle assembly only at liquid-liquid interfaces,[67] iii) E. Kumacheva et al. had an overview of nanoparticle assembly only directed by external fields (e.g., electrical fields, magnetic fields, ultrasound fields, light fields),[68,69] iv) L. M. Liz-Marzan et al. recapped different methods for directed self-assembly of nanoparticles by either changing

---

A. Sun
Department of Chemistry
Stony Brook University
Stony Brook, NY 11794, USA

S. Yang
Materials Science and Engineering
School for Engineering of Matter
Transport and Energy (SEMTE)
Arizona State University (ASU)
Tempe, AZ 85287, USA

A. M. Kannan
The Polytechnic School (TPS)
Ira A. Fulton Schools of Engineering
Arizona State University (ASU)
Mesa, AZ 85212, USA

Y. Golan
Department of Materials Engineering
and the Ilse Katz Institute for Nanoscale Science and Technology
Ben-Gurion University of the Negev
Beer Sheva 8410501, Israel

J. Lancaster
Department of Immunology
Mayo Clinic Arizona
13400 E Shea Blvd, Scottsdale, AZ 85259, USA

L. Chen
Mechanical Engineering
University of Michigan-Dearborn
4901 Evergreen Rd, Dearborn, MI 48128, USA

E. B. Joyee
Mechanical Engineering and Engineering Science
University of North Carolina, Charlotte
9201 University City Blvd, Charlotte, NC 28223, USA

K. Song
School of Environmental, Civil, Agricultural, and Mechanical Engineering (ECAM)
College of Engineering
University of Georgia (UGA)
Athens, GA 30602, USA
E-mail: kenan.song@asu.edu

K. Song
Adjunct Professor of School of Manufacturing Systems and Networks (MSN)
Ira A. Fulton Schools of Engineering
Arizona State University (ASU)
Mesa, AZ 85212, USA

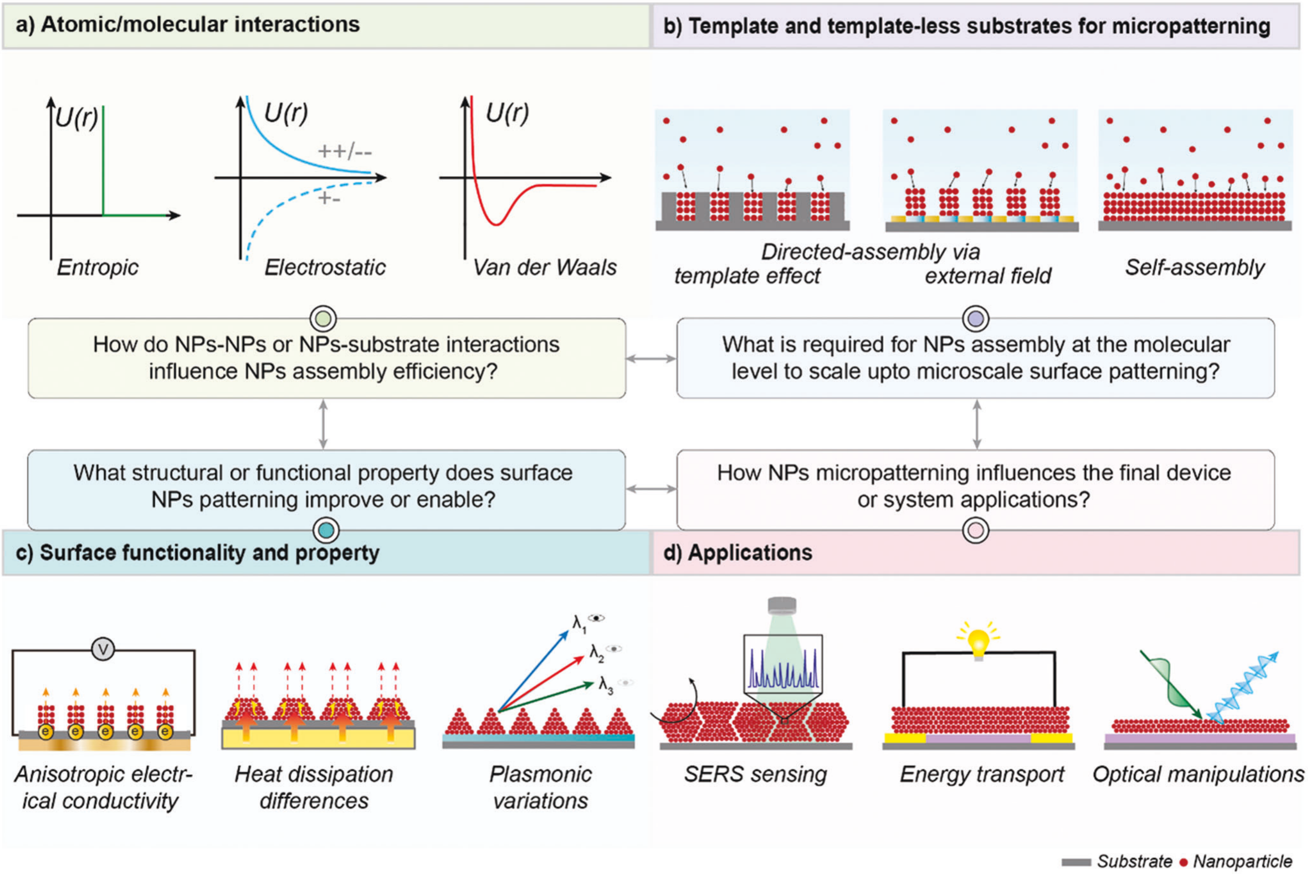

Figure 1. The integration of templated/template-less substrates and suspension-based deposition for surface micropatterning of nanoparticles (NPs). a) Effective molecular interactions (e.g., entropic, electrostatic, and van der Waals) may facilitate NP self-assembly on the substrate surfaces b) via directed assembly on templated/patterned substrates or self-assembly without templated surface. Micropatterned NPs display unique surface functionalities and properties, e.g., c) anisotropic electrical conductivity, directional heat dissipation, and heterogeneous plasmonic effects for applications, including but not limited to the d) surface-enhanced Raman spectroscopy (SERS) sensing, energy transport, and optoelectronics.

the energy or entropy landscapes by using templates or applying external fields,[20] v) Y. T. Chun et al. overviewed technologies for micro-to-nanometer patterning of solution-based materials for a wide range of practical applications in electronics and optoelectronics fields.[70] vi) T. Xu et al. reported the overview on assembly and applications of only anisotropic nanomaterials,[21] vii) H. Zhang et. introduced different methods for assembly of 2D nanosheets into 1D microstructures for potential application in energy storage, electronic devices, and sensors,[71] viii) H. N. Alshareef et al. outlined the printing and advanced coating techniques for complex micropatterning of only MXene nanoparticles,[72] ix) Y. L. Kong et al. briefed patterning of nanoparticles during 3D printing obtained by leveraging mechanical, electrical, magnetic, thermal, or optical phenomena,[73] x) P. A. Levkin et al. reported surface micropatterning only by the formation of 2D droplet microarrays on predesigned and chemically modified surfaces for high-throughput applications, including cell-based screening, controlled particle deposition, (bio)sensor fabrication, and chemical synthesis in droplets,[74] xi) A. V. D. Berg et al. recapitulated only the nanomanufacturing of templates by top-down (i.e., nano-machining) and bottom-up (i.e., self-assembly and chemical vapor deposition) methods,[75] xii) J. Thomson et al. reiterated the physicochemical mechanism of nanoparticle self-assembly and their practical application in nanofabrication for photonic crystal dye laser, three-dimensional nanocrystal (NCs) and nanowire architectures, antibacterial silver Bragg mirror, and dye-anchored mesoporous metal oxide electroluminescent devices,[76] and xiii) G. Wilde et al. summarized template-based surface nano-patterning only by three template preparation techniques, namely, ultrathin aluminum membranes, monolayer polystyrene spheres, and block copolymer patterns.[77]

Current reviews have summarized the fundamentals of thermodynamic and kinetic mechanisms during NP self-assembly, the physiochemical mechanism of patterning of solution-based nanomaterials, techniques of complex template fabrication and surface micropatterning, and directed assembly of nanoparticles in the presence of an external field. However, the state-of-art in processing methods and their principles are poorly understood. As a result, this review will summarize nanoparticle self-assembly and directed assembly only in the absence of an external energy source (e.g., electrical field,[78] magnetic stimuli,[34] mechanical stretching,[79] optical manipulations[80]) for surface micropatterning purposes (**Figure 2**). This review will

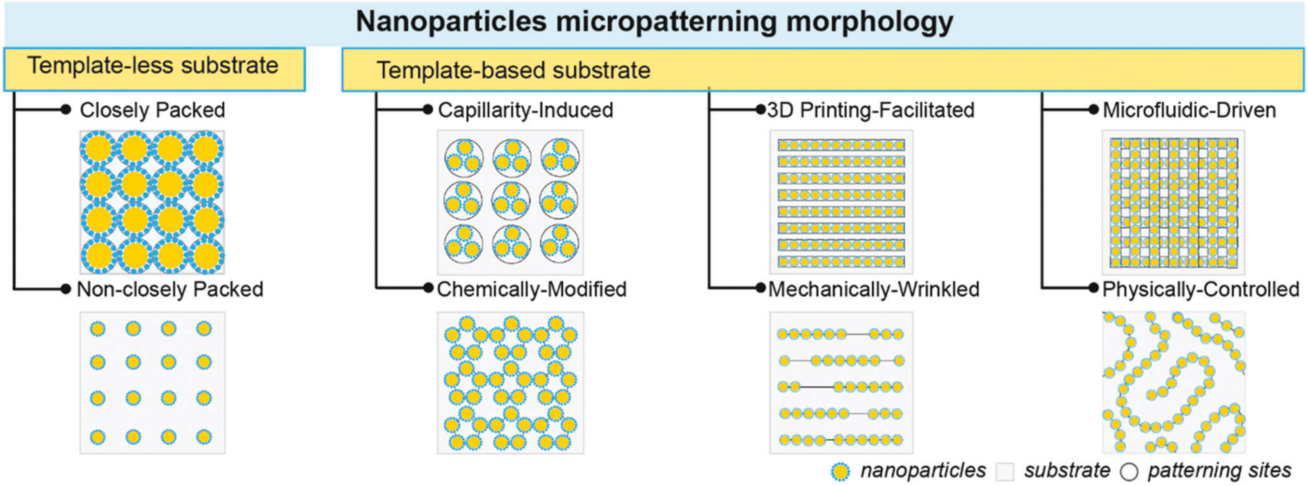

Figure 2. Categories of surface micropatterning techniques via nanoparticle assembly for micro- and macroscale deposition depending upon varying NP-template interactions. Micropatterning is differentiated based on template-less (i.e., closely and non-closely packed) and template-based (i.e., capillary induced, chemically modified, 3D printed, wrinkled, microfluidic driven, physically controlled) substrates.

first summarize the template-less approaches conventionally used for NP self-assembly as a contrast. The patterning diversity in continuous and noncontinuous styles will be correlated to their fabrication procedures and structural orders. Subsequently, the template effects (e.g., predefined topographic structures of grooves, micro mold, and trenches) and surface influences will be elaborated in template-assisted methods.[81–84] The template effects will focus on the nanomanufacturing methods and their processing mechanisms with the micro and nanoscale nanoparticle-nanoparticle or nanoparticle-template interactions. For example, the assembled NPs with 2D topology or 3D architectures will be achieved by i) template fabrications or ii) functionalizing surfaces, followed by iii) leveraged interparticle forces.[85] Note that although most nanoparticles in colloids and surface science studies from other reviews involve 0D spheres (e.g., polymers of polystyrene (PS), silica (SiO_2), gold (Au), iron oxide (Fe_3O_4)) due to the dimensional straightforwardness and momentum simplicity, this review will diversify the demonstration examples and discuss the case studies in 1D and 2D NPs.[20,24,86] These 1D NPs include whiskers (e.g., silver (Ag), halloysite, CNTs), and 2D planes include MXene or graphene. In addition, many literature studies have reviewed the soft matter and biomaterial patterning, covering cells, DNAs, tissues, and proteins, which will thus be excluded from our focus.[87–90] The discussion of nanoparticle manipulations and the micropatterned surface properties with a few enclosed micropatterns for the functional applications, such as microelectronics, optoelectronics, plasmonics, anticounterfeiting, magnetic devices, and biological will be introduced before the conclusion/outlook.

2. Nontemplate-based Nanoparticle Assembly

The self-assembly of NPs is the spontaneous organization of nanoparticles into organized and stable structures.[20] Different substrates have been used for directing the self-assembly of NPs, e.g., non-templated (e.g., flat, featureless) or templated (e.g., with grooves, trenches, pillars, traps) surfaces.[85] Two categories of NP patterns can be manufactured on the planar substrates (non-templates): continuous & closely packed patterns and non-continuous & non-closely packed patterns. In continuous patterns, NPs are closely packed structures in the form of a monolayer or multilayered thin film where NPs are in contact with each other. This pattern possesses highly packed, long-range ordered NPs (e.g., hexagonal for monolayer and other crystals of body-centered cubic, face-centered cubic, and hexagonal closed packed for multilayers) self-assembled as 2D films or coatings with minimum interparticle distance.[91,92] In non-continuous patterns, NPs are separated by different spacings and can form different surface patterns, such as linear, cubic, wavy, and concentric geometries.[93]

2.1. Continuous, Closely Packed Nanoparticle Patterns

Evaporation-mediated or thermodynamics-controlled drying has been widely used for NP assembly into continuous thin-film structures because of the simple, efficient, and fast procedure. The continuous NPs deposition on centimeter-sized templates can be obtained by different techniques of dip coating, spin coating, spray coating, droplet casting, Langmuir-Blodgett (LB), and interfacial assembly for a variety of NPs and varying substrates (**Table 1**).[22,70,94] The most straightforward approach to assembling NPs on the flat (e.g., glass, silicon wafer) substrate is drop-casting of NPs dispersion with subsequent solvent evaporation.[95] This drying method patterned NPs as a “coffee-ring” microstructure when the solvent in a drop of suspension is evaporated. During evaporation on a flat surface, the radially outward flow of solvent due to the surface tension gradient carries NPs toward the edge of the droplet, where string-like particles are deposited (**Figure 3**a$_1$). This “coffee ring” effect during manufacturing has been known to reduce effective interfacial contact due to non-uniform NPs deposition, which deteriorates the electrical properties of processed devices.[96,97] The NPs arrangement

Table 1. Summary of the coating techniques for non-templated (planar) patterning.

Substrate material	NPs	NP size [µm]	Assembly technique	Scalability [cm^2]
Glass	SiO$_2$	0.36	Langmuir-Blodgett	63[103]
Glass	PS	1.1	Doctor blade coating	4[104]
Glass	Latex	0.18–1.15	Inclined drop-casting	1.25[105]
Glass	PS	0.2	Self-assembly	1[106]
Glass	Halloysite	2	Spray coating	1950[107]
Glass	SiO$_2$	2	Dip-coating	0.165[108]
Silicon	SiO$_2$	0.27	Convective self-assembly	4[109]
Silicon	SiO$_2$	2	Dip coating	0.3[110]
Silicon	SiO$_2$	0.1, 0.5, 1	Dip coating	2.25[110]
Silicon	SiO$_2$	0.21 – 2.1	Dip coating	0.25[111]
Silicon	MXene	1.5	Langmuir–Blodgett	60–705[112]
PVC	SiO$_2$	0.97	Langmuir-Blodgett	925[113]
PET	SiO$_2$	0.4	Scalable printing	30[114]
Sapphire	SiO$_2$	0.3	Spin coating	20.3[115]
Soda-Lime Glass	MXene	1.5	Spin coating	6.45[116]
ITO-Coated Silicon	MXene	2	Spray coating	4.2 – 243[117]

Abbreviations: ITO, indium tin oxide; PET, polyethylene terephthalate; PS, polystyrene; PVC, polyvinyl chloride; SiO$_2$, silica; silicon, silicon wafer.

can be modified from a "spot-inside-ring" pattern to a more "homogenous" film by an increase in surface roughness, surface free energy, adhesion force, contact angle hysteresis, and droplet size of the dual surface-architectonics (SA) substrate.[97,98–100] For example, to address this, Minori's group has shown uniform deposition of Au NPs on the ultraviolet (UV)-irradiated and alkali-washed dual surface-architectonics (DSA)-based substrates without severe coffee ring effect and central spot (Figure 3a$_2$).[101] The high surface free energy and strong adhesion force of the modified substrate surface hindered the radial flow of NPs and a homogeneous deposition of NPs was obtained. In addition, superhydrophobic surfaces (i.e., polydimethylsiloxane (PDMS)) also prevented "coffee ring" formation due to a higher contact angle, which lowers the contact between specific NPs colloids and substrate, retaining the droplet shape during evaporation.[102]

The closely packed, continuous NP assembly can be formed at the liquid/liquid or liquid/liquid/air interface after the evaporation of the solvent. For example, the LB-based self-assembly method is a thin-film processing approach where the NPs dispersed in volatile and water-immiscible solvents are spread on the water surface to create the monolayer that can be transferred from the liquid-air interface to the solid substrate.[113,121] LB forms a nanostructured thin film with a unique microstructure and thickness control for various applications. However, some NPs must be surface treated to avoid dissolution in solvents to obtain stable LB film. A typical example is metal NPs coated with polyvinylpyrrolidone (PVP). To address this problem of intermixing, J. Huang et al. have studied the ability of electrospray to spread the aerosolized solvent droplets from a few millimeters in diameter to the micron- and sub-micron scale. The reduced size of spreading droplets would not be significantly affected by gravitational force. It would be completely consumed during the initial spreading, which avoids intermixing, leaving only NPs on the water surface (Figure 3b$_1$-b$_2$). During the demonstration, the spreading solution was prepared by dispersing 300 nm 0D PS nanospheres in ethanol and water as a stock solution before spreading it on the water surface to create closely packed monolayers over large areas.[118] Figure 3b$_3$-b$_5$ shows the SEM morphology of the zoomed-in OM regions (Figure 3b$_4$) of the PS bead monolayer collected on the Si wafer obtained by combining E-spreading with LB assembly. This hybrid manufacturing exhibited the massive potential to standardize and scale up for facile and quick processing of bulk nanostructures.

Self-assembly of 1D NRs is complex compared to 0D NS because of the anisotropy, high aspect ratio, and high surface area.[122] Many studies have demonstrated the anisotropic particle alignment in a continuous way using simple dip-coating and evaporation-induced nanoparticle assembly on a planar substrate.[48,123] The 1D NPs are transported to the confined meniscus by the convective flow at the air-liquid-solid interface leading to the orientation of NRs parallel to the interface through self-assembly.[124,125] Imai et al. have demonstrated the importance of liquid flow for forming 2D nematic monolayers by comparing the calcite NPs' self-assembly behaviors (Figure 3c$_1$).[119] The prolonged recession rate (40 nm s^{-1}) of the ethanol without evaporation showed the random distribution of colloidal nanorods (CRs) on the substrate. When the ethanol dispersion was evaporated at the same recession rate (40 nm s^{-1}), the direction of calcite NRs was organized parallel to the air-liquid-solid interface line (Figure 3c$_2$). The crystallographic orientation of the nanorod was within 20° of the air-liquid-solid interface with a highly ordered arrangement compared to assembled films without solvent evaporations (Figure 3c$_3$). Additionally, a variety of particles of silica, WO$_{2,}$ and CeO$_2$ were deposited into $_{an}$ ultrathin, uniform, and defect-free monolayer on the 1.5 × 1.5 cm^2 Si substrate to demonstrate the general particle compatibility with this simple processing.[110,126]

Although many techniques have been utilized for fabricating ultrathin patterns with an ordered assembly of 0D and 1D NPs, precise assembly of 2D NPs on desired templates could be challenging due to the flexibility and low bending modulus for the 2D particle conformation.[71] For example, 2D graphene monolayers are thermodynamically unstable at room temperature, leading to rippling morphology.[127] Thus, most techniques would cause crumpled structures due to lower entropy, especially when liquid flow is involved.[71] Experimentally, spray and spin coating can produce thin film coatings from 2D NPs; however, they usually lead to the "island" formation when the dispersion is dilute, which would deteriorate the thin film functionality. Nevertheless, the fabrication of self-assembled 2D NPs into a nanometer-scale thin film with the interfacial self-assembly approach has been reported. For example, C. W. Ahn et al. showed that the thin MXene (Ti$_3$C$_2$) layer was formed by spreading MXene/water/ethyl acetate droplets on the water surface (Figure 3d$_1$). The evaporation of ethyl acetate caused turbulence in the MXene solution through Rayleigh-Benard convection, followed by exposing the water layer on the surface.[120] Due to the Marangoni effect, the MXene flakes were self-assembled

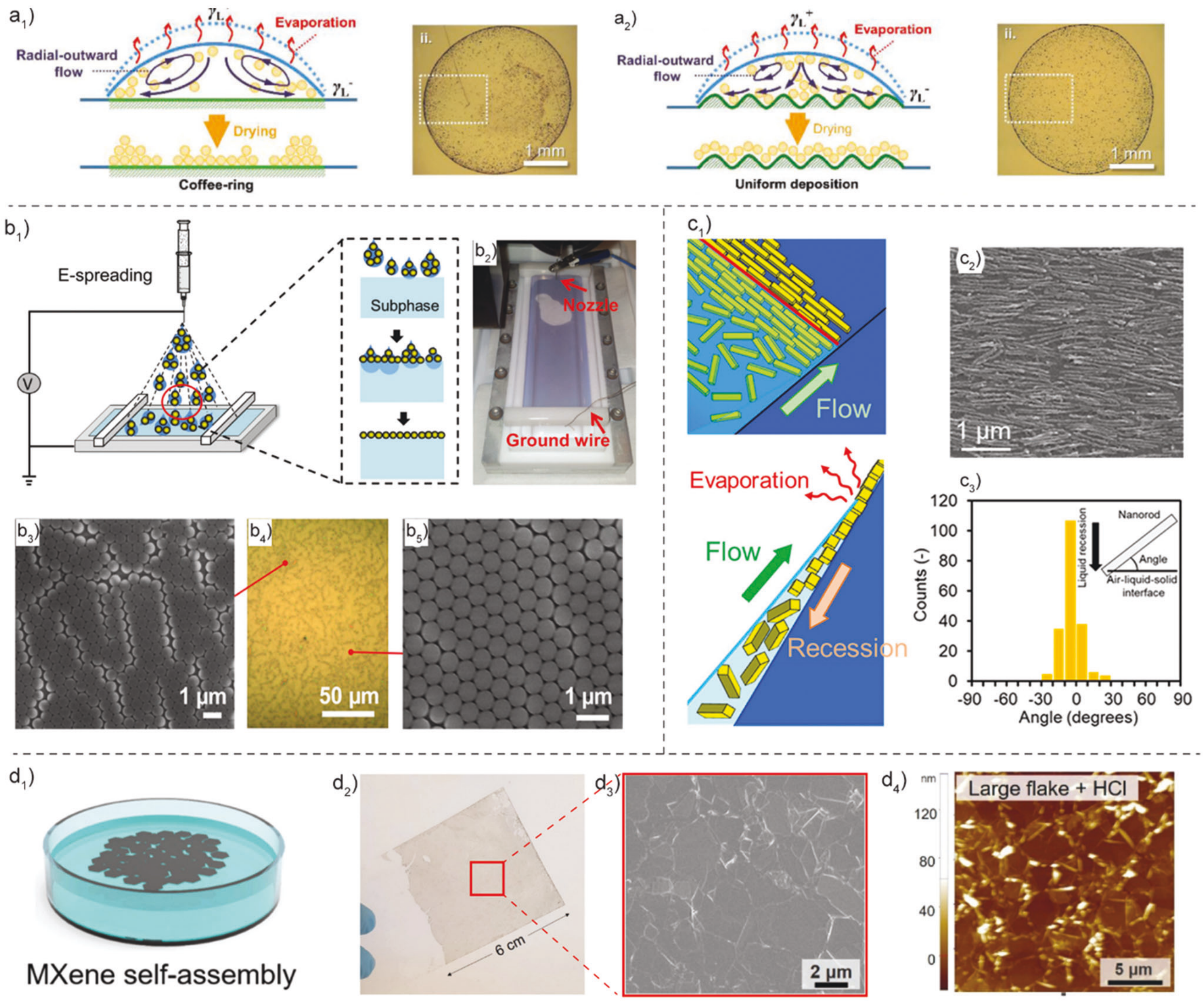

Figure 3. The schematics and optical microscopy (OM) images show the solute evaporation and surface morphology evolution of drying dispersions (i.e., 0D gold (Au) NPs) for different coffee-ring films formed by a_1) surface-architectonics (SA) and a_2) dual surface-architectonics (DSA) substrates. Reproduced with permission.[101] Copyright 2021, Wiley-VCH. b_1) The electrospray (E-spray) schematic demonstrates how small-volume microdroplets can be effectively dispersed on the water surface, thereby preventing intermixing issues, b_2) digital photograph shows the high efficiency of electrospray-deposited 0D NPs on the water surface for large-area assembly (2.5 × 13 cm), and b_3-b_5) scanning electron microscopy (SEM) and OM images confirm the formation of a closely packed monolayer of the 0D PS NPs (300 nm) on the Si substrate. Reproduced with permission.[118] Copyright 2015, American Chemical Society. c_1) A schematic illustration of the assembly mechanism of a stabilized monolayer of 1D calcite nanorods (NRs) obtained by the evaporation of the dispersion and recession of the liquid-air contact line, with the c_2) zoomed-in SEM image of a millimeter scale substrate (≈5 × 10 mm) and c_3) the alignment angle distribution (angular deviation is within 20^0) of a self-assembled 2D nematic monolayer of 1D calcite NRs obtained after the evaporation of the solvent. Reproduced with permission.[119] Copyright 2021, American Chemical Society. d_1) Schematic showing the interfacial self-assembly mechanism for manufacturing ultrathin (nm-scale) 2D Ti_3C_2 MXene films, with the d_2) digital image of 2D MXene-composed film transferred onto a PET substrate demonstrating large area patterning (6 × 6 cm^2), and d_3) SEM & d_4) atomic force microscope (AFM) images showing surface topography of 2D Ti_3C_2 MXene films. Reproduced with permission.[120] Copyright 2019, American Chemical Society.

into the closely packed thin film at the water-air interface.[120] The assembled film was then transferred onto a PET substrate which displayed uniform surface morphology of the thin film over a considerably large area with good plane-to-plane adherence of 2D sheets (Figure 3d_2-d_4). Additionally, multilayer films can be transferred onto the target substrate from a single batch solution showing reproducibility and efficient use of raw nanomaterials.

2.2. Noncontinuous or Non-Closely Packed Nanoparticle Patterns

The lack of control over nanoparticle-substrate interfaces usually leads to the randomly oriented NP assembled on the substrate without any particular order. Manipulating NP shapes, sizes, and surface functionalization can be efficient in tuning interfacial interactions with substrates. For example, the controlled substrate

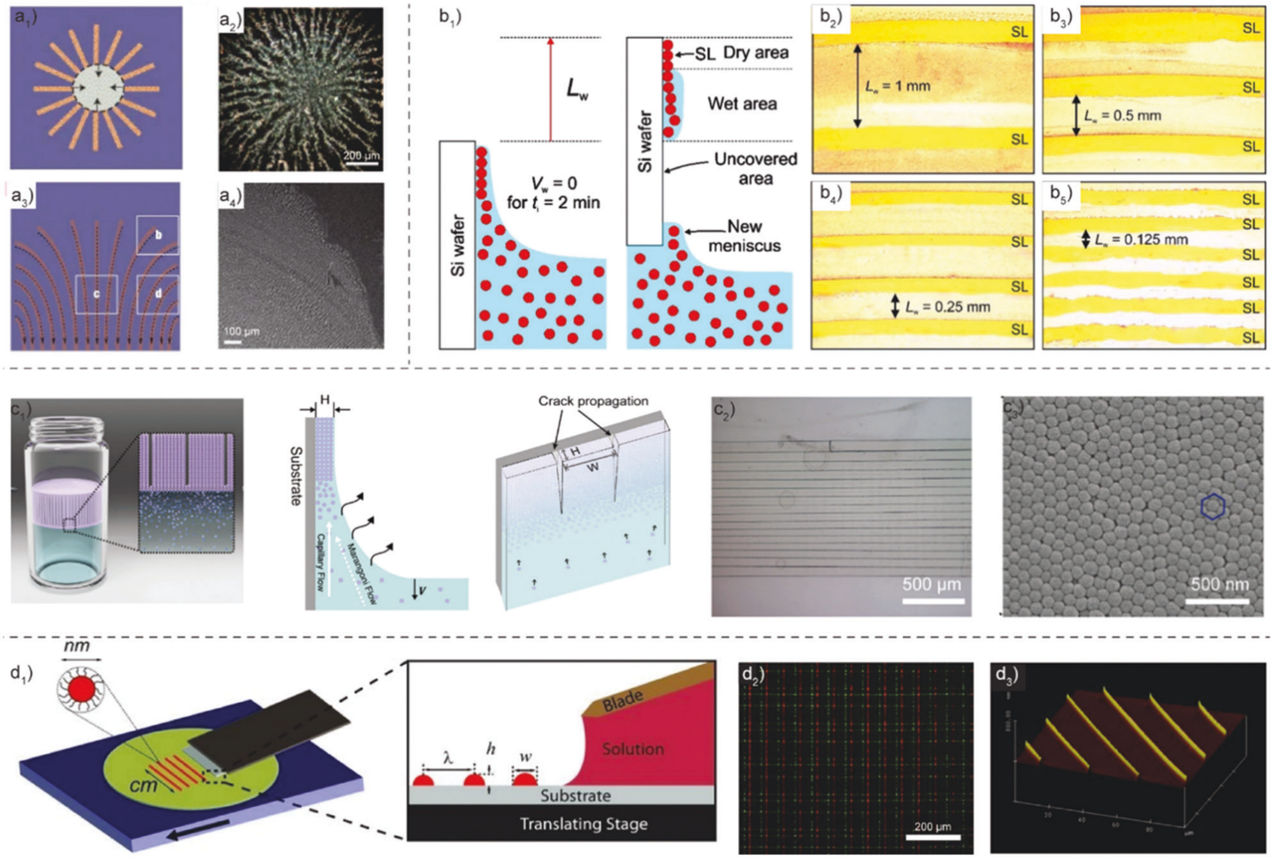

Figure 4. a_1-a_2) A schematic drawing and the optical image showing the formation of spoke patterns (propagating inward along the arrows) of ≈100 nm 0D Au NPs on hydrophilic SiO_2/Si substrate, a_3-a_4) a schematic and the SEM image showing the stripe pattern of 0D Au NPs formed by the moving contact line, with the arrows indicating the withdrawal direction of the meniscus as the substrate was pulled out of the dispersion. Reproduced with permission.[129] Copyright 2005, Nature. b_1) 2D schematic illustration of the dip-coating setup for the self-assembling 1 μm 0D silica (SiO_2) nanospheres (NS) into stripes via layer-by-layer procedures, which were conducted at a substrate temperature = 70 °C, substrate withdrawal speed (V_w) = 1.3 μm s^{-1}, withdrawal angle = 0°, and withdrawal step length (L_w) at b_2) 1 mm, b_3) 0.5 mm, b_4) 0.25 mm, and b_5) 0.125 mm, respectively. Reproduced with permission.[110] Copyright 2018, American Chemical Society. c_1) A schematic illustrating the silica rod assembly with the mechanism of crack engineering via a "tear of wine" phenomenon, with c_2) an optical image showing assembled silica rods of 110 nm 0D SiO_2 NPs on a glass vial wall during crack propagations, and c_3) the SEM image of zoomed-in silica rods showing deposited NPs in a close-packed, hexagonal-like structure. Reproduced with permission.[130] Copyright 2021, Wiley. d_1) A schematic of the flow-coating apparatus for generating simple stripe and complex grid patterns of CdSe quantum dots (QDs) on a silicon wafer, d_2) an AFM image of simple QD stripe patterns with ridge-like surface morphology was obtained by using a programmed distance of 20 μm and a holding time of 1 sec, and d_3) a fluorescent microscopy image of complex grid patterns generated by a three-step flow-coating process via rotating the blade to 90° after each coating (three times) for homo- or hetero-junction configurations at each cross-point. Reproduced with permission.[131] Copyright 2010, Wiley-VCH.

dewetting can lead NP dispersions to form well-aligned micropatterns, other than a continuous thin film, with tunable orientation, thickness, and periodicity on the planar substrate.[128] During one demonstration, Yang et al. reported the formation of the unique spoke-like radial pattern by rearranging Au (∼100 nm) and Ag (∼50 nm) NPs at the retreating waterfront of a dilute LB film on a hydrophilic substrate. The NPs aggregated at the solvent-substrate interface (spoke tips), which acted as a site for accumulating nanoparticles during evaporation.[129] **Figure** 4a_1-a_2 shows the inwards deposition of NPs leading to the formation of a spoke-like pattern (arrows) and its microstructure deposited on the substrate. The convective flow of the NPs from the solvent to the accumulation sites generated the elongated fingertips pattern. As compared to the LB method, dip-coating is another convenient method for controlling the dewetting of the meniscus, where the retreating meniscus is moved upward along the substrate pulling direction. The highly oriented stripe patterns with uniform thickness and inner stripe distance were formed for Ag and Au NPs (Figure 4a_3-a_4). This approach of this solution dewetting-induced NP assembly is a rapid and inexpensive bottom-up process for selective positioning and patterning of NPs into islands, stripes, and continuous film morphology over a large-area substrate.[128,129]

The self-assembly of NPs into regulated patterns (e.g., wavy bands, rings, strips, and rods) is essential for applications requiring anisotropic material distributions or stepwise loading/release behavior. Among these shapes, linear strips/gratings have attracted attention due to their diverse application in drug delivery, microelectronics, photonics, sensors, batteries, and catalysis.[109,129,132] The most straightforward way to obtain linear band-like patterning morphologies is by "dip-coating" with proper control of process parameters, such as the withdrawal speed (V_w), dip time, and hold time (Figure 4b$_1$). The mechanism of band formation depends on the "stick and slip" motion, where the density and spacing of the band were controlled by sticking time and slipping distance, respectively.[132] During one demonstration, Dahiya et al. showed the formation of periodic stripes of silica NS by increasing V_w by three orders of magnitude faster than the downshift speed of the meniscus (V_m) used for continuous deposition.[110] Figure 4b$_2$-b$_5$ shows the uniform dimensions of stripe width and stripe-to-stripe spacing, where the inter-strip spacing depended on withdrawal distance (L_w = 1, 0.5, 0.25, and 1.25 mm). At the meniscus pinned region (i.e., wet), the NPs were deposited, but when the substrate was pulled out of the solution, the uncovered region (i.e., dry) was formed due to a higher withdrawal rate than the evaporation rate at the meniscus. The excellent dimensional control of patterning morphology can be achieved through the easy, rapid, and scalable evaporation-based assembly for developing optical grating, filters, and polarizers.[133]

Self-assembly of NPs in a specific desired shape may be feasible at the nanoscale; however, centimeter-scale patterning has been challenging. Templates with specific surface properties, usually requiring delicate processing and costly equipment, are common.[36,134] Contrarily, the assembly of NPs into uniform and centimeter-scale patterns without template effects would be more facile. Recently, Deng et al. developed a unique strategy to assemble colloidal silica NPs into centimeter-long lines using crack engineering without template assistance (Figure 4). The undesirable cracks favored uniform colloidal line formation, and their dimensions were tailorable by solvent compositions, suspension descending rates, and NP volume fractions. The particle flux is expressed as $j_p = N_p{*}V_p{*}v_p$, where N_p is the number of particles per unit volume, V_p is the volume of a single particle, and v_p is the mean velocity of suspended particles.[130] The value of j_p increased with evaporation rates; thus, ethanol was added to water/silica dispersions to enhance solvent evaporation rates. The increased j_p with higher N_p and evaporation rates led to wider and thicker vertical lines. The water/ethanol mixture facilitated the "tear of wine" phenomenon, where a tiny droplet was dragged by gravity back into the suspension, leading to crack formation and propagation as the solvent evaporated (Figure 4c$_1$). After water/ethanol evaporations, the self-assembled silica rods (e.g., 1 cm long) were patterned between two adjacent cracks with highly uniform width/thickness (Figure 4c$_2$-c$_3$).

The patterning via mere solution evaporations (e.g., a stick-and-slip motion in dip coating or LB methods) requires precise control over substrate features or NP morphology due to the instability generated during solvent evaporations. To address this, the A. J. Crosby et al. team has confined the deposition solution to a restricted geometry via a flow coating technique to improve the patterned feature regularity.[131] Figure 4d$_1$ shows the flow coating apparatus consisting of a blade attached above the flat substrate to create the restricted geometry for simultaneous NPs deposition. The NP solution was trapped between the two plates by capillarity, and the evaporation of the solvent caused the outward flow of NPs, leading to the strip formation composed of vinyl benzene-functionalized CdSe QDs (~3 nm).[131] The spacing between the neighboring stripes was controllable by the moving translation stage. As the meniscus was stretched during the movement, the contact angle decreased below the critical contact angle when capillary forces exceeded the pinning forces.[131] This deposition mechanism generated line and grid patterns by rotating the stage to 90° to perform the second cycle flow coating of red QDs over green QDs (Figure 4d$_2$-d$_3$).

3. Template-directed Nanoparticle Assembly

Unlike existing literature reviews in the field of nanoparticle assembly, this review article takes a distinct approach by focusing specifically on the effects of surface templates on nanoparticle assembly processes (Section 3). While previous reviews have covered various aspects of nanoparticle assembly, they often do not delve into the systematic processing of templates using different manufacturing techniques. This review addresses this gap by providing a comprehensive overview of template-based nanoparticle assembly, highlighting the techniques employed to generate templates, and their synergistic effects in nanoparticle processing methods, which will be elaborated in Section 3. Unlike other reviews with specific thematic focuses, such as assembly at liquid interfaces,[38,135] external field-directed assembly,[136,137] or specific nanomaterials,[138,139] this review offers a comprehensive and organized examination of the role of templates across diverse areas of nanoparticle assembly. Additionally, our review extends its scope to practical applications beyond the microscale, showcasing the broader implications of template-based nanoparticle assembly in fields such as electronics, optoelectronics, and more, which will be elaborated in Section 4. This approach provides readers with a comprehensive understanding of how different template-based assembly techniques can contribute to versatile nanoparticle patterning for various applications.

3.1. Capillarity-Induced Nanoparticle Assembly

NP patterning based on natural forces is attractive because it can occur spontaneously without external field effects. In suitable environments, natural evaporative forces, such as capillary, London, and van der Waals, originate from the dispersion interaction between the NPs and the wetting substrate.[140] Among these naturally occurring forces, capillary forces have been widely studied as an efficient method for assembling micro-and nanoscale objects on various topological surfaces from its aqueous or organic solvent-based colloidal suspensions.[141] Capillary force-driven assembly is a dewetting process during which the meniscus of the evaporating droplet containing nano/microscale particles drags over a templated surface, thus having predefined sites or confined dimensions.[85,142,143] The template defines the space, location, or direction in which the NPs are deposited in continuous or noncontinuous format for diverse assembly patterns. In previous research, conventional template manufacturing approaches have been studied for patterning NPs of different shapes on predetermined sites via capillary guided assembly, as listed in **Table 2**. The capillary interactions between the fluid-substrate appear when the interfaces are subjected to evaporation, boundary formation, and movement of

Table 2. Conventional template manufacturing methods for capillary-effect-assisted NP assembly.

NPs	Template fabrication methods	Template materials	Capillary-assisted Assembly mechanism	Pattern resolution [nm]
0D	Replicated from master template	PMMA	Meniscus-dragged accumulation	400-800[151]
	E-beam lithography	PMMA	Site-directed assembly	35[155]
	Soft lithography	PDMS	Trap-directed assembly	1200[156]
	Direct laser writing + reactive ion etching	Silicon	Capillary bridge-driven NP deposition	4000[122]
	UV photolithography	PFPE	Vacuum-assisted evaporation	16-10[58]
1D	Photolithography	PS	Evaporation- and curvature-driven transport	223 ± 24[157]
	E-beam lithography	PMMA	Site-directed assembly	40[155]
	Microfabrication	Si/Cr oxide	Dielectrophoresis	3000[158]
	UV lithography	Au coated Si	Template-directed assembly	40[159]
	Soft lithography	PDMS	Convective flow due to solvent evaporation	200[160]
2D	E-beam lithography	Silicon	Collapse lithography	70[161]
	Thermal evaporation, spin coating	Au Silicon, PLLA	Hydrophobic interaction	500[162]
	Microcontact printing	Silicon	Surface wettability	23.4[163]
	Roll-to-roll	PMMA	Flow-enabled assembly	2000[164]
	Soft lithography	PDMS	Interfacial interaction	3000[134]

Abbreviations: 0D, zero-dimension; 1D, one-dimension; 2D, two-dimension; Au, Gold; Cr, Chromium; PDMS, polydimethylsiloxane; PFPE, perfluoropolyether; PLLA, poly(L-lactic acid); PMMA, poly(methyl methacrylate); PS, polystyrene; Si, silicon; UV, Ultraviolet.

fluids.[144,145] Capillary force-driven self-assembly has different advantages, for example, low cost, processing simplicity, general material compatibility, and high precision.[94,146,147] The different nanoparticles, such as polymeric,[148,149] ceramic,[150] metallic,[143,151] semiconductor,[78,152] and biological[153,154] have been deposited on a broad range of templates with evaporative capillarity assistance.

The mechanism of NP assembly via capillary assembly involves specific steps (**Figure** 5a$_1$), such as trapping NPs into compliant sites, resisting receding suspension front, and drying residual solvent.[165] First, the accumulation zone near the meniscus is created via convective flow in capillary assembly, which minimizes surface-free energy.[165] During the evaporation of the solvent, long-range force brings NPs toward the meniscus to direct the NPs toward the specific template locations (e.g., low surface energy and affinity to nanoparticle surfaces).[166] Once the NPs are trapped inside these patterned regions, short-range forces (e.g., capillarity) and confinement effects are responsible for permanent particle placement. As the meniscus evolves and moves over the template, pinning-depinning occurs repetitively at trapped locations, generating large-volume or large-area depositions.[156] For example, Au NRs were trapped within predefined sites with vertical barriers along the single edge of the trap (Figure 5a$_2$).[165] Also, the positional accuracy and alignment of these AuNRs measured from the angular distribution showed a narrow distribution range (<2.04°) due to superior assembly performance (Figure 5a$_3$).

A sandwich-shaped patterning approach called the capillary bridge manipulation method would include a flat substrate, an aqueous solution of dispersed nanoparticles, and templates with periodically arranged microfeatures.[167] For example, Jiang's group demonstrated long-range patterning of $BaTiO_3$ NCs by the confinement of liquid on top of micropillars (MPs) with the template fabricated by lithography and reactive ion etching (Figure 5b$_1$).[168] The lyophilic micropillar tops served as high adhesion sites for regulating the position, size, and geometry of capillary bridge formation and $BaTiO_3$ NCs deposition. As a result, the capillary bridge manipulation improved the directional capillary flow to generate the fluidic flow and mass transport at the micro/nanoscale with high precision (Figure 5b$_2$).[168] The pinning of a meniscus, solvent evaporation, and capillary flow of nanocrystals led to the formation of nanocrystal superlattices on a target substrate.[168] Different shapes, such as circles, squares, pentagons, hexagons, and crosses have been fabricated by controlling the shape of a capillary bridge depending on the surface dimensions of micropatterned templates (Figure 5b$_3$).

Capillary assembly requires a delicate surface design, usually accompanied by UV lithography and plasma etching, which is costly and labor-intensive. To solve this problem, Wu et al. reported elastocapillary interaction and femtosecond-laser printing to produce scalable fibrillar assemblies (Figure 5c$_1$).[33] The patterns with elliptical MPs displayed anisotropic capillary forces that could direct the development of ordered complicated structures via collapsing.[33] The self-assembled structure depends on the capillary force (F_c) and standing force (F_s) between MPs; when $F_c > F_s$, the pillar collapses, and assemblies will be formed, as shown in (Figure 5c$_2$). The success rate (%) of collapsing the pillars relied on the dimensions (e.g., thickness, height, width) of pillars, spacing between pillars, and contact angle of the liquid on pillars (Figure 5c$_3$). A higher aspect ratio of MPs increased the difference between F_s and F_c, which would cause the easier collapse of two pillars.[169] These capillary-driven self-assembled structures resulted in solution-evaporation-driven self-assembly of microparticles, such as NaCl, glucose, and $CaCO_3$, in between cells (Figure 5c$_4$), for chemistry, biomedicine, and microfluidic engineering.[33]

The swarm intelligence-inspired self-assembly strategy for polystyrene and silver NPs into predesigned pillar-patterned silicon templates is reported by Y. Song et al.[171] This process

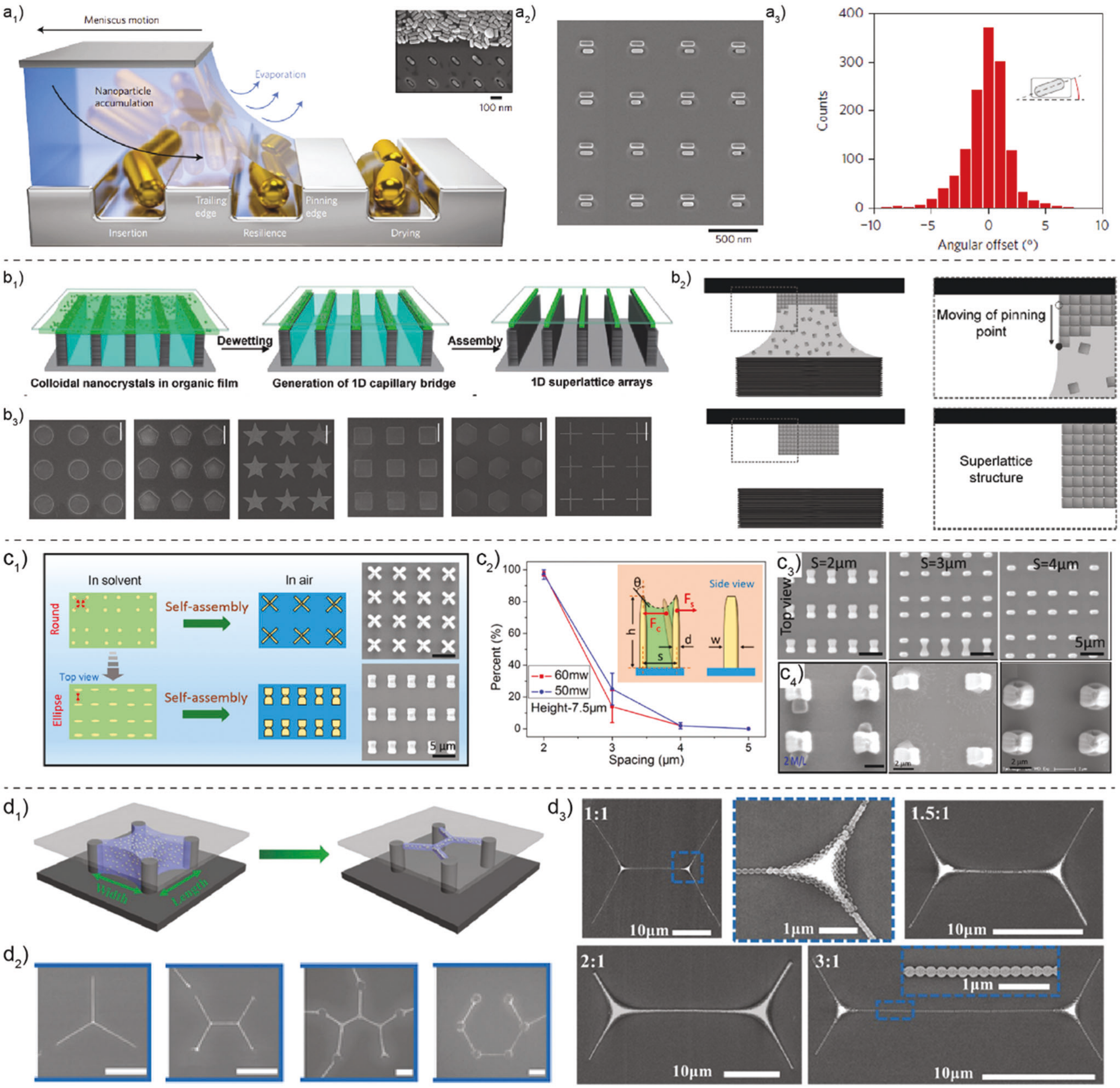

Figure 5. Natural force-assisted nanoparticle assembly: a_1) a schematic illustration of capillarity-induced nanoparticles assembly onto the topographical sites, with a_2) electron microscopy imaging of Au nanorods (NRs) assembled in an array of traps fabricated by lithography, and a_3) the histogram showing a narrow angular distribution when NRs were assembled with highly aligned orders. Reproduced with permission.[143] Copyright 2017, Springer Nature. b_1) Schematic illustration of the fabrication procedure of $BaTiO_3$ nanocrystal (NC)-formed arrays via the two-step dewetting and assembly processing, with b_2) schemes showing capillary bridge formation and dewetting of $BaTiO_3$ ink in an individual capillary bridge, and b_3) SEM images of $BaTiO_3$ assembled NCs in superlattice structures with the shape of a circle, pentagon, star, square, hexagon, and cross (scale bar 20 μm). Reproduced with permission.[168] Copyright 2017, Wiley-VCH. c_1) Micropillars (MPs) with different cross-section designs (e.g., round or ellipse) and their self-assembly via asymmetric capillary force, with c_2) a plot showing the influence of spacing on the self-assembly, c_3) SEM images showing the assembly of elliptical MPs at different spacing distances (S = 2,3, and 4 μm) (scale bar 5 μm), and c_4) micrographs of entrapped NaCl, $CaCO_3$, and glucose microparticle arrays (scale bar 5 μm). Reproduced with permission.[169] Copyright 2015, American Chemical Society. d_1) Swarm intelligence-inspired assembly of NPs into shortest interconnect by spontaneous droplet manipulation via capillary confinement, formation of arrays of a liquid bridge, evaporation of the solvent, and alignment of NPs, d_2) NP assembly for shortest interconnect patterns between 3, 4, 5, and 6 MPs (scale bars 20 μm), and d_3) Ag NP assembly among four nodes of rectangles with different length-to-width ratios (blue box indicates enlarged views of straight line and triple junction). Reproduced with permission.[170] Copyright 2017, Wiley-VCH.

enabled the production of various interconnect designs (e.g., Steiner tree) without the need for complex and vacuum-requiring manufacturing processes such as photolithography and metal sputtering. Figure 5d_1 scheme represents the assembly process of NPs via droplet evolution by manipulating the solid/liquid/gas three-phase contact line (TCL) with the patterned MPs. The MPs array generated the capillary force between the pillar and substrate and drove the AgNPs suspension to fill in the pillar gaps. The MPs ruptured the AgNP's suspension and evaporation of solvent spread and contracted the TCL along a designed direction which formed 3 μm wide liquid bridge arrays of certain geometric configurations.[171] The liquid bridge obeyed the area-minimizing principle to form gradually reduced confined spaces for nanoparticle aggregation and assembly.[171] Through similar mechanisms, four, five, and six MPs formed the shortest interconnecting patterns of one, two, three, and zero Streiner trees, respectively, with the minimum surface energy indicating the thermodynamic stable state (Figure 5d_2). Figure 5d_2 shows the Streiner tree distribution (1:1, 1.5:1, 2:1, and 3:1 length-to-width ratios) by adjusting the length-to-width ratio of pillar patterns on the template from 10 mg mL^{-1} concentration. The SEM shows the enlarged view of a triple junction and straight lines with single nanoparticle patterning (Figure 5d_2). This swarm intelligence-inspired capillary-driven assembly technique shows a promising application in the formation of minimum network high-performance electronics, optics, and other devices.

3.2. 3D Printing-Facilitated Nanoparticle Assembly

3D Printing is an advanced manufacturing technique that translates computer-aided design (CAD) 3D models into physical objects via a layer-by-layer (LbL) addition.[172] The most widely used 3D printing techniques are stereolithography (SLA),[173] digital light processing (DLP),[174] fused deposition melting (FDM),[175] liquid deposition modeling,[176] direct ink writing (DIW),[177] powder bed fusion (e.g., selective laser melting/sintering (SLM/S)),[178] inkjet (e.g., multi-jet fusion, polyjet),[179] sheet lamination,[180] and electron beam melting.[181] Different polymeric materials used in 3D printing include monomers for thermosets, thermoplastics, elastomers, polymer composites, and nanoparticle colloids.[1] Various studies reported the alignment and assembly of nanoparticles using FDM, SLA, DIW, and inkjet techniques in bulk composites.[97,183–185] These printed composite structures have demonstrated enhanced mechanical performance[26,33] with imparted thermal,[186,187] electrical,[188–190] optical,[191,192] and intelligent functions[193,194] from reinforcement fillers to 3D devices or systems. Combining functional properties via assembled nanoparticles and the versatility of different 3D printing techniques can enable the fabrication of highly complex, heterogeneous, and hierarchical 3D architectures.

Previous reviews have summarized 3D printing for rapid prototyping of multi-materials (e.g., polymers and particles) at multiple scales (e.g., nanoscale morphologies and macroscale structures).[195] Additionally, these multi-material systems displayed nanoparticle alignment in 3D printing mechanisms that can lead to selective deposition and preferential orientation of nanoparticles.[180] However, integrating NP assembly via deposition techniques, such as evaporative-induced assembly, microfluidic transport, and external fields, into 3D printing for nanomanufacturing for 3D architectures remains a relatively unexplored area.[26,62,196] Some interparticle forces, including van der Waals attractions, steric repulsions, capillarity, convective forces, and electrophoretic and magnetophoretic interactions, can facilitate the long-range and short-range NP assemblies.[197] On the one hand, 3D printing can enable flexible customization of templates with unique topologies and morphologies, in contrast to conventional template manufacturing approaches, which require molds, dies, and masks with delicate polymer chemistry to control processing precisions, leading to a reduction in development time and high cost.[198,199] The multiscale NP self-assembly on 3D printed templates can also enable tunable features, dimensions, and functions. On the other hand, 3D printing with nanoparticle deposition capabilities can also selectively organize their location and orientation on 2D surfaces or in 3D spaces. The 3D printing-facilitated nanoparticle patterning is a new approach with limited research. Thus, some of these 3D printing methods and nanoparticles are summarized in **Table 3**.

The photopolymerization-based approaches (e.g., two-photon polymerization (2PP), muti-photon polymerization (MPP), SLA, DLP, and micro-continuous liquid interface production (μCLIP) techniques) are helpful for template fabrications due to their comparatively higher resolutions than other 3D printing methods.[212,213] One study of the μCLIP demonstrated a continuous generation of polymer surfaces with a feature resolution below 100 μm via photo-polymerizing monomer resins. This fast and continuous production in μCLIP is due to creating the "dead zone" between the UV image projection window and the polymerizing part, inhibiting the resin's photopolymerization.[214] Song's group has used this μCLIP for micropatterned templates before direct ink writing of MXene (Ti_3AlC_2) flake suspensions. Subsequently, the capillary-induced deposition organized NPs into linear and complex geometries (**Figure 6**a_1).[62] These templates had microchannels that confined MXene inks, whereas microfluidic forces (i.e., capillary, van der Waals, gravity) facilitated the LbL addition of these flakes.[62] The patterned structures showed well-aligned, high-resolution, and high aspect-ratio patterning of MXene flakes with in-plane and out-of-plane alignment (Figure 6a_2-a_3). The patterned MXene lines displayed multifunctional properties, i.e., anisotropic conductivity and piezoresistive sensing with a wide sensing range, high sensitivity, fast response time, as well as enhanced mechanical durability.[62]

One-dimensional nanoparticles are more typical in NP assembly because of their anisotropic nature and uniform surfaces. Song's group used 3D printing and conventional nanoparticle processing to demonstrate assembly efficiency. First, SLA was used to 3D print templates with different cross-sectional profiles (e.g., triangular grooves). Then, conventional LbL assembly was achieved via dip-coating for micropatterning of 1D Carbon nanofibers (CNF) (Figure 6b_1).[209] CNFs were dispersed in tetrahydrofuran for suitable dispersions, and the presence of surface microfeatures directed the CNF anchoring and accumulations. Specifically, the interactions between the template microfeatures and dispersion meniscus manipulated the CNF deposition sites to initiate the packing of more NPs. The LbL processing parameters also influenced NP assembly morphologies (e.g., from the aligned straight lines via horizontal dipping, to

Table 3. 3D printing-facilitated NP assembly.

3D printing method		NP assembly mechanism	Micropattern morphology	Pattern resolution [µm]	Ref.
Feedstock	3D printing				
Monomers for surface topology design	2PP	electrodeposition	conical cavities	1.42	[56]
	MPP	surface functionalization	scaffolds	1	[200]
	Confined electrodeposition	e-beam vapor deposition	large circuit pattern	150	[201]
	DLP	acoustic field	parallel lines	50	[202]
	3D optical printing	electrochemical deposition	microfish	30	[203]
	SLA	e-field	Microcones arrays	50	[204]
Inks	Inkjet	solvent evaporation	QR codes	50	[179]
	Screen Printing	direct deposition	integrated circuits	200	[205]
	Pen-based writing	direct writing	concentric patterns	300	[206]
	DIW	direct deposition	mesh, concentric	50	[207]
	EHD	e-field	circuit patterns	45	[208]

Abbreviations: 2PP, two-photon polymerization; 3D, three-dimensional; DLP, digital light processing; EHD, electrohydrodynamic; MPP, muti- photon polymerization; QR, quantum rod; SLA, stereolithography.

wavy bands, to randomly oriented films via vertical dipping) (Figure 6b$_2$). The NP assembly showed well-aligned and closed-packed microstructures formed via repetitive LbL deposition to yield nano-mesoscale hierarchies.[209,215] The fabricated composites displayed directional electronic conductivity, high sensitivity, and mechanical robustness, demonstrating their applications as gas, strain, and pressure sensors.[209]

Apart from the surface patterning function similar to capillary effects, other 3D printing can be promising for direct NP assembly. For example, electrohydrodynamic (EHD) is capable of 50 nm-precision depositions of nanoparticles to form 2D or even 3D functional structures. Bhaskaran et al. used the EHD to self-assemble a monolayer of AuNPs via layer additions without conventional lithography.[62] First, the electrostatically attractive ink of (3-aminopropyl)triethoxysilane (APTES) was EHD printed onto a substrate to pattern intricate structures as a functional monolayer. The positive charges were to drive the NP self-assembly from colloids via evaporative and electrostatic forces (Figure 6c$_1$). These monolayers formed high-resolution, stable structures across large scales with a resolution of 7 µm in width, 75 µm pitch between individual lines (Figure 6c$_2$) with the finest feature of 300 nm (Figure 6c$_3$). EHD shows enormous potential for precise and low-cost surface patterning with a high-resolution assembly of general NPs useful for applications in sensors, actuators, robotics, electronics, antennas, and metasurfaces.[196]

3D printing of multi-materials is unfolding more potential of NPs patterns. However, they often require multi-nozzles and inorganic solvents for dispersing nanomaterials, limiting their practical uses. To address this, R. Spolenak et al. reported a multiscale, multi-material 3D printing technique called electrohydrodynamic redox printing (EHD-RP), which enabled direct printing and mixing of multiple, high-quality metals from a single nozzle.[211] In this work, electrochemistry was utilized to synthesize metallic NPs deposits by situ dissolutions of the metal anode (M^0) and generated metal ions (M^{z+}) inside the nozzles that were ejected toward the substrate to form metallic deposits (M^0) after the reduction (Figure 6d$_1$).[211] The fast switching of the deposited metals allowed 3D printing of chemically heterogeneous Ag and Cu NPs (Figure 6d$_2$-d$_3$). Additionally, the printed features via EHD-RP were within sub-micron ranges with complex microstructures, such as overhangs of up to 90^{0}C printed by point-by-point strategy and more out-of-plane sine waves by LbL strategy (Figure 6d$_4$). These high spatial-chemical resolutions of printed microstructures showed crystalline and dense morphologies with a high strength of 1-1.5 GPa for Cu pillars. Thus, the EHD-RP possesses the potential for the bottom-up fabrication of chemically distinct 3D devices with locally tuned functional properties for application in catalysis, robotics, and cellular design.[216,217]

3.3. Microfluidic-Driven Nanoparticle Assembly

Microfluidic assembly with precise fluid control has attracted interest in the delivery and patterning of NPs into long-range microstructures. Microfluidic devices consisting of microchannels are used as templates for area selective patterning of 0D, 1D, and 2D NPs depending on the channels and NPs interactions.[1–3] The simultaneous use of geometric patterns (critical dimensions of less than 1 mm) and NPs dispersion provides a rapid, economical, and scalable fabrication method for micropatterning of NPs by microfluidic assembly approach. At this scale, researchers can benefit from physical phenomena for example rapid diffusion,[220] laminar flow,[221] Dean flow,[222] and rapid thermal transport[223] with a large surface area relative to the volume.[224] Due to various benefits, the microfluidics approach displayed applications in many fields including analytical chemistry,[223] nanoparticle synthesis,[56] energy generation,[225] micropatterning,[62] cell separation,[222] and molecular biology.[226] G. V. Jensen's review paper has summarized different techniques for fabricating microfluidic devices, such as micromachining, photolithography, cleanroom fabrication (i.e., wet etching and reactive ion etching), injection

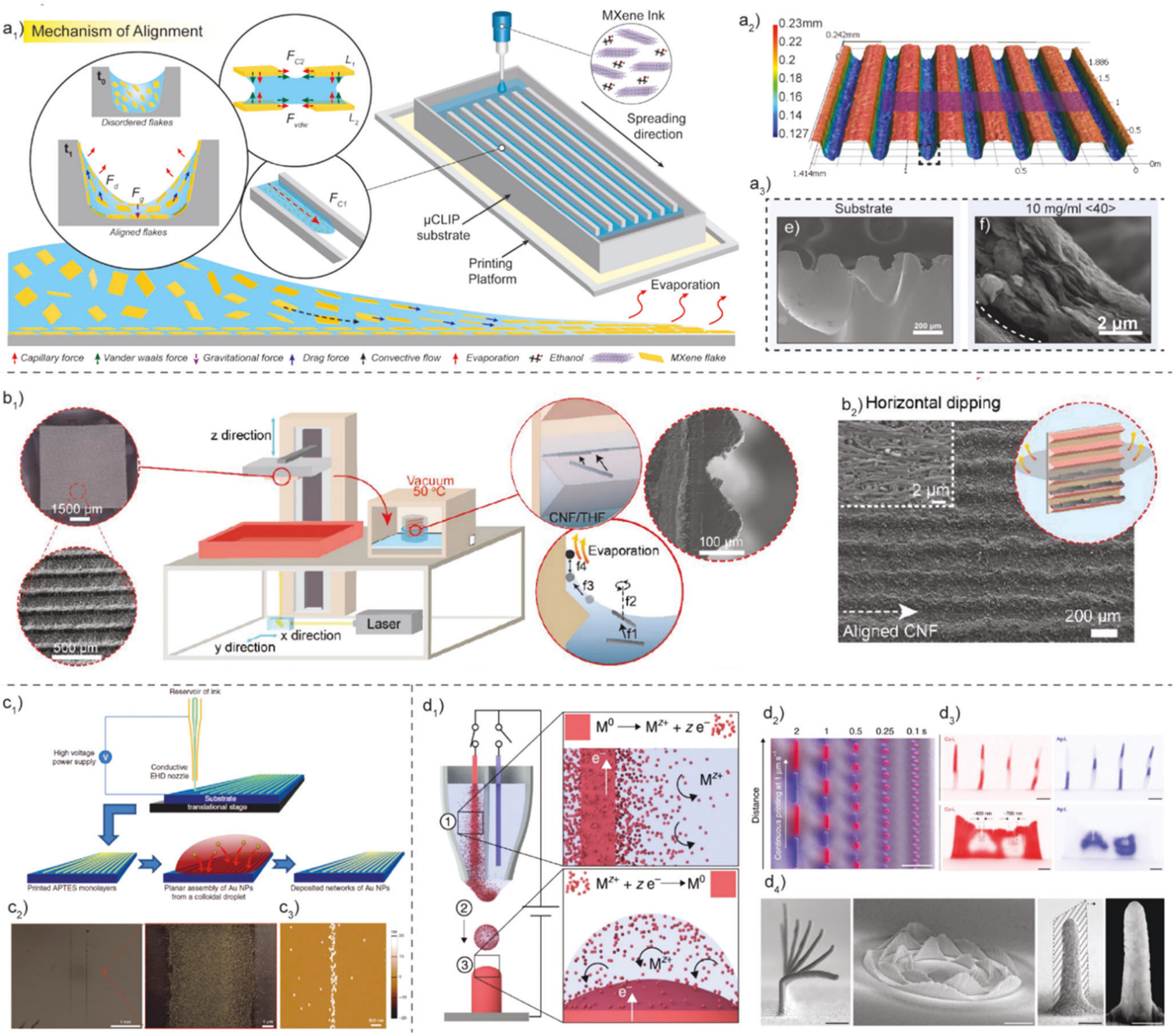

Figure 6. 3D printing-facilitated nanoparticles assembly: a$_1$) a schematic showing the alignment mechanism of 3D printed patterning and aligning of 2D Ti_3AlC_2 MXene nanoparticles via hybrid 3D printing approaches (i.e., micro-continuous liquid interface production (μCLIP) and direct ink writing (DIW)), with a$_2$) μCLIP-printed surface topography for a$_3$) DIW-patterned MXene lines with SEM images showing LbL stacking of MXene flakes along the cross-sections. Reproduced with permission.[62] Copyright 2021, American Chemical Society. b$_1$) NP assembly mechanisms of micropatterned trenches having triangular features for patterning 1D carbon nanofibers (CNFs) via hybrid manufacturing (i.e., stereolithography (SLA) with dip coatings), and b$_2$) surface topography of uniformly deposited CNF bands with unidirectionally aligned features obtained via horizontal dipping, while vertical dipping showed different surface resolutions. Reproduced with permission.[209] Copyright 2020, American Chemical Society. c$_1$) Process of electrohydrodynamic (EHD) jet of functional monolayers of (3-aminopropyl) triethoxysilane (APTES) for patterning of Au nanoparticles, with c$_2$) SEM images showing Au assembled on APTEs arrays with 7 μm densely packed layers across the surface (scale bar 1 mm and 1 μm), and c$_3$) AFM images showing the Au NP lines of delicate features of 300 nm-wide bands (scale bar 500 nm). Reproduced with permission.[210] Copyright 2017, Springer Nature. d$_1$) The schematic showing the working principle of electrohydrodynamic redox printing, with energy dispersive spectroscopy (EDS) mapping showing the capability of d$_2$) fast switching between the two metals (i.e., Cu-L signal, red and silver (Ag)-L signal, blue), d$_3$) printing at a different location with Cu and Ag metals (e.g., alternating pillars and wall with embedded "Ag" letter), and d$_4$) SEM images of as-printed microstructure in complex geometries, e.g., overhand structure, out of plane sine waves, and pillars (scale bars of 1, 2, 200 nm). Reproduced with permission.[211] Copyright 2019, Springer Nature.

molding, and, most recently, additive manufacturing.[227,228] The direct and replication approaches depending on the nature of the manufacturing process are categorized in **Table 4**. Note that the 3D printing methods listed are mainly for microfluidic devices to facilitate NP assembly, different from the direct nanoparticle deposition and organization in Section 3.2. The chemical processing is primarily lithography or other chemistry-based methods involving monomer polymerizations under EUV or oxidation/reduction reactions, different from the surface functionalization in Section 3.4. Mechanical processing lists the

Table 4. The classification of microfluidic device fabrication techniques.

Process Type	Technology
Additive manufacturing	FDM,[229,230] SLA,[230,231] μCLIP,[62,232] MJP,[233,234] SLM,[235] 2PP[236,237]
Chemical processing	UV lithography,[238,239] EBL, nanoimprinting lithography,[240,241] soft lithography,[227,242] wet etching[243,244]
Mechanical processing	Micro-milling,[245,246] micro-grinding,[228] micro abrasive water jet machining,[247] CNC machining,[248,249] ultrasonic machining,[250] injection molding,[251] hot embossing,[251,252] replica molding,[253,254] casting[242,255]
Other energy-intensive physical processing	Laser writing,[256,257] laser ablation,[258] laser microcladding,[259] FIB,[53,260] EDM,[261,262] optical waveguide writing,[263] laser-induced forward transfer,[264] laser micro-fabrication with masks,[265,266] laser-induced electro-less plating[267,268]

Abbreviations: CNC, computer numerical controlled; EBL, E-beam lithography; EDM, electro discharge machining; FIB, focused ion beam; MJP, multiJet printing.

conventional machining methods, including turning, milling, drilling, reaming, grinding, and polishing, which will be different from, though relevant to, Section 3.5.

The microfluidic devices use capillary actions to manipulate the NP deposition into a patterned region. The capillary effect is governed by intermolecular interaction between the liquid and geometry, and its magnitude is inversely proportional to capillary radius or feature size.[269] The capillary force can be improved by ten times the atmospheric pressure for the feature size of the sub-100 nm range.[270] As given below, the capillary force for driving the solution inside the microfluidic channels is the Laplace pressure (P_L).

$$P_L = \frac{2\gamma\cos\theta}{r} \tag{1}$$

Here, γ is the liquid-air surface tension, θ is the wetting angle of the liquid on the capillary wall surface, and r is the capillary radius. Also, the Reynolds number (Re) for the suspension fluids must be small (i.e., $Re << 1$) for a laminar flow within the channel. This laminar flow is critical in forming uniform-aligned morphology in NP patterns.[218,271]

$$Re = \frac{\rho v L}{\mu} \tag{2}$$

Here, Re is the Reynolds number, ρ is the density of suspension fluids, v is the velocity of the fluid, L is the characteristic length, and μ is the fluid's viscosity. The evaporation thermodynamics and capillary kinetics of polymeric solutions and nanoparticle dispersions depend on the kind of capillaries, such as those channels with two-side-open, on-side-open, channel-surface-open, spiral-shaped, or straight-line-shaped.[140] A few examples of these types are explained in the following sections.

The conventional imprinting method involves a two-side-open channel for the capillary to pattern and orient nanoparticles via fluid transport and confinement effectively. For this approach, a PDMS template with a microchannel structure was placed on the flat substrate, and nanoparticle dispersion was deposited close to one end of the PDMS microchannel, as shown in **Figure 7**a$_1$. Owing to capillary force, the colloid liquid guided into the microchannels, and the gradual evaporation of the solvent deposited the nanoparticles into the confined region. As one demonstration, H.B. Sun et al. studied the assembly of gold nanoparticles into aligned and densely packed straight, curved, and network structure micro/nanowires with a uniform width and smooth surface (Figure 7a$_2$-a$_4$). Due to high capillarity, the colloidal transported into microchannels, and liquid evaporation led to the deposition of nanoparticles on the sidewalls of microchannels. Because the sidewalls of the microchannels acted as a deposition site, the evaporation of water molecules in gold NP dispersions generated the micro/nanowires on both sides of the microchannels (Figure 7a$_5$). This conventional imprinting approach extends its range of practical applications by coupling with the external fields, such as centrifugal force, acoustic energy, and electric field, for large-scale production.[238,272]

Some external field-driven self-assembly processes required specific material properties (i.e., electric, dielectric, magnetic responsiveness) and complex experimental procedures to control the assembly of the NPs suspended in solution.[275–277] In comparison to these external field-directed techniques, T. K. Seo et al. designed a microfluidic device coupled with the centrifugal force for the chemical synthesis and physical assembly of various core-shell type nanoparticles (Figure 7b$_1$-b$_2$).[248] For example, a Pd-nanocube-core with an Au/Pt-shell was synthesized by sequentially transporting Pt^+, Pd^+, and Au^{3+} solutions into the reaction chamber with different rotational directions and speeds (Figure 7b$_3$-b$_5$). The injected solution into the reservoir was equally and automatically transported into 60 reaction chambers via centrifugal force. By changing the molar ratio between Au and Pt, 60 different kinds of Pd@AuPt core-shell NPs (particle diameter 10–12 nm) are synthesized within minutes (Figure 7b$_6$). Thus, this centrifugation-microfluidic method for nanocatalysis could be used over conventional batch reactions because of various advantages, namely, complete parametric studies, fast reaction kinetics, precise flow manipulation, low consumption of reagents, and automation.[278]

The capillary flow generated within open microfluidic channels confines the liquid between the side walls, and NPs settle down in the LbL fashion due to the gravity effect and hydrodynamic forces (different from the natural forces-assisted assembly reviewed in Section 3.1). For example, X.J. Zhang et al. studied the in-situ patterning of Ag nanoparticles into open microchannels fabricated with photolithography (Figure 7c$_1$). They investigated the influence of microchannel geometry (e.g., spiral, contraction and expansion, side chamber, and hexagonal shape) on the patterning of nanoparticles. Simulation and experimental results showed that spiral shape geometry has uniform velocity profiles and shear stress distribution along the flow direction (Figure 7c$_2$), which would benefit the patterning uniformity. In other geometries, regions with higher and lower velocities along the flow direction introduced the disturbance to flow and

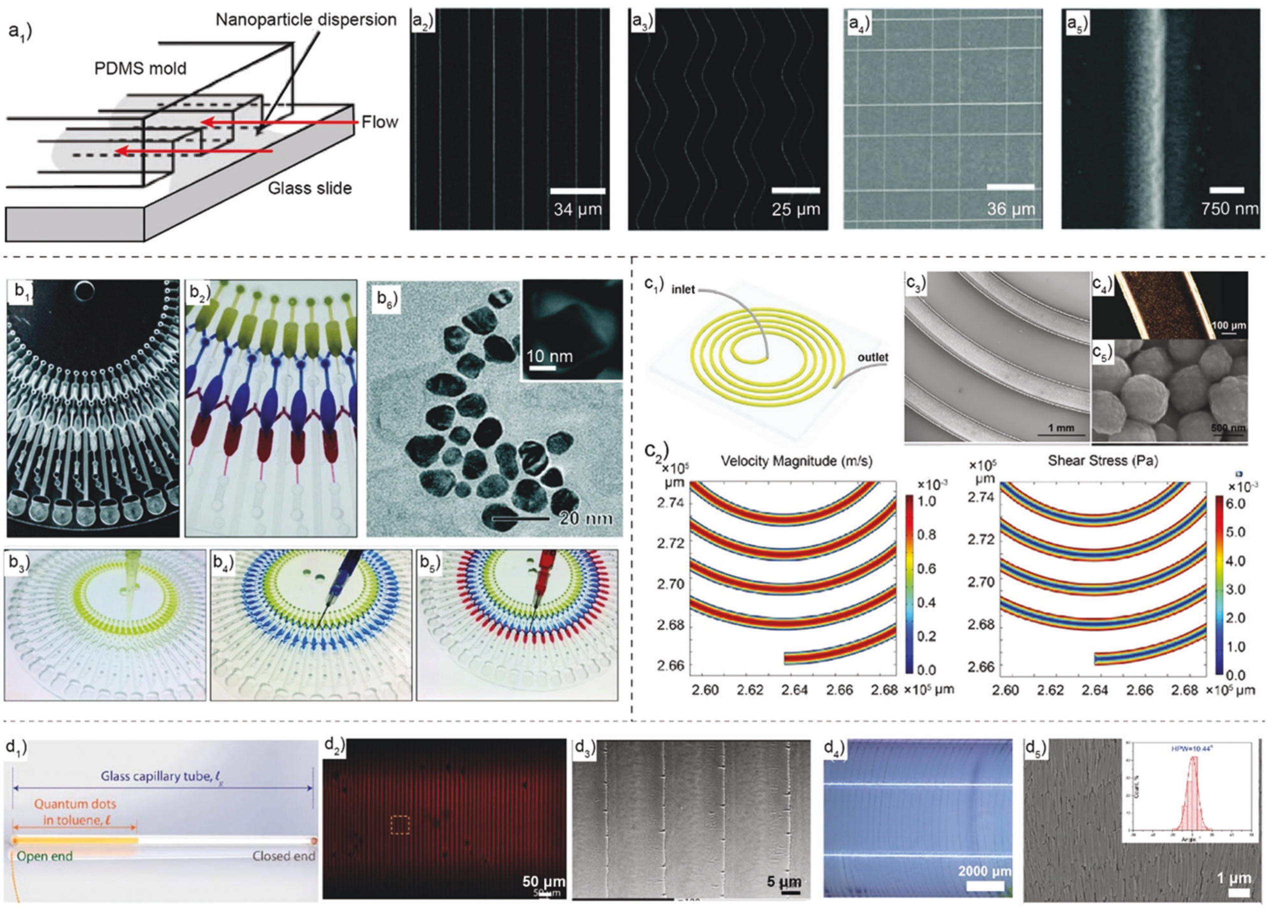

Figure 7. Microfluidic-driven NP assembly: a_1) schematic showing the mechanism of nanoparticle patterning using a micromold-based micro-imprinting technique, with different arrays of a_2) straight, a_3) wavy, a_4) network structures, and a_5) a high-magnification image of patterned gold nanoparticles with open-end capillarity. Reproduced with permission.[273] Copyright 2019, The Royal Society of Chemistry. b_1) A digital image of a microfluidic device fabricated via a computer numerical control (CNC) machine, with b_2) a zoomed-in digital image of the device injected with three metallic solutions (Au^{3+} = yellow, Pd-cubes = blue, and Pt^{2+} = red), b_3-b_5) the manual injection of the metallic solutions (Au^{3+}, Pd and, Pt^{2+}) into reservoir showing automatic filling of the zigzag microchannels with the single shot, and b_6) a transmission electron microscopy (TEM) image of synthesized Pd@AuPt core-shell nanoparticles with a proper molar ratio of Au/Pt (particle diameter 10–12 nm). Reproduced with permission.[248] Copyright 2020, American Chemical Society. c_1) The design of the microfluidic device for silver NP deposition into a spiral-shaped pattern, c_2) simulation results of the velocity and shear stress distribution profile at a flow rate of 10 µL $\min^{-1}$ formed inside the microfluidic channels, c_3-c_5) SEM and dark-field optical images of silver NPs showing uniform deposition within the spiral contour. Reproduced with permission.[219] Copyright 2021, American Chemical Society. d_1) Schematic of capillary glass tube loaded with CdSe/ZnS/toluene-based QDs suspensions (i.e., the tube is placed on a horizontal surface with the right end of the tube sealed), d_2) a confocal microscopy image of QDs band arrays along the tube with a 0.05 mg mL^{-1} concentration, d_3) SEM image shows the morphology of band arrays with a bandwidth of 5 µm. Reproduced with permission.[274] Copyright 2015, American Chemical Society. d_4) An optical image of stripe patterns composed of halloysite nanotubes (HNTs) formed along the capillaries with d_5) an SEM image of HNT patterns shows ordered stripes formed from HNTs suspensions at a concentration of 10%HNTs and the inset histogram showing the small angular distribution of 10.44°, suggesting overall preferential alignment of HNTs. Reproduced with permission.[255] Copyright 2016, American Chemical Society.

caused nonuniform patterning of silver NPs. The improper geometry would form aggerates of random size and morphology, with lower resolution control over nanostructures that could negatively affect fabricated device performance. Among many other parameters, the channel geometry played an essential role in the successful patterning of Ag NPs, e.g., the spiral-shaped microchannel explored in this work enhanced the pattern quality and showed potential in surface-enhanced Raman spectroscopy (SERS) sensing applications (Figure 7c_3-c_5).

Different NPs dispersions, such as halloysite,[219,255] gold,[279] tobacco viruses,[280] and quantum dots[274] (Figure 7d_1) were loaded into the capillary tube and evaporated to generate distinct deposition patterns due to subsequent pinning and depinning from the contact line. In H.A. Stone's work, a concentric ring-like pattern with the banding structure of QDs was deposited on the surface of the capillary tube upon evaporation (Figure 7d_2).[274] The coating morphology of different widths and spacing was tuned depending on the speeds of evaporation and nanoparticle concentrations (Figure 7d_3). Similarly, C. Zhou et al. showed 1D HNT deposition inside the capillary, leading to long-range-ordered HNTs with highly preferential alignment after the evaporation (Figure 7d_4).[255] The 1D HNTs were aligned in the direction parallel to the tube edge with an angular orientation of 10.44° (Figure 7d_5). The parallel orientation was caused by the development of flow-induced (van der Waal's) torque on the nanotube when one of the ends is pinned at the contact line. These patterned surfaces within confined geometry possess high roughness, which could capture the tumor cell compared to bare glass surfaces in biomedical applications. The emergence of capillary-driven microfluidic devices has shown exciting possibilities in drug delivery, biosensor, nanomedicines, diagnosis, cell culture, and cancer-related therapeutical applications.[281–284]

3.4. Chemically Modified Surfaces for Nanoparticle Assembly

The patterned templates with asymmetric chemical structure or wettability can induce NP assembly depending on the different surface free energy of the patterned surface.[285,286] The difference in surface free energy manipulates the behavior of the TCL formation and directs the NPs to flow toward the designated region via convection.[287] For example, the generation of hydrophilic and hydrophobic patterns on the substrates would control the pinning patterns (i.e., confinement) and solution properties (i.e., capillarity) of the NP colloids.[288] This interfacial manipulation strategy initiates the self-assembly patterning of NPs via nucleation and crystallization into well-ordered structures (e.g., dots, lines, and stars). Previous chapters have detailed the dispersion of NP colloids onto the patterned template surface using straightforward coating methods including droplet casting, doctor blade coating, dip coating, spin coating, and brushing.[289] The coating approaches offer facile operation, minimum equipment requirements, and large area patterning of NPs with well-controlled 3D morphology of NP assembly for fabricating complex electronic devices.

Constructing controlled 3D self-assembled architectures in a simple and cost-efficient manner is challenging. Y. Song et al. proposed a strategy for patterning NPs into 3D architectures from a single droplet via ink writing.[290] In **Figure 8**a, the microdroplet containing poly(styrene-methyl methacrylate-acrylic acid) NPs were dropped on the template surfaces with different surface wettability. The difference in surface energy of hydrophobic and hydrophilic regions forced the three-phase contact line to slide along a surface with low surface energy and pinned at the region of high surface energy.[290] This assembly procedure involves the driving force ($F_{\Delta RCA}$) and the resistance force ($F_{\text{resistance}}$). First, the $F_{\Delta RCA}$ generated by surface free energy difference to manipulate the TCL formation is given by[291]

$$F_{\Delta RCA} = \Delta l_1 \gamma \cos\theta_{R1} - \Delta l_2 \gamma \cos\theta_{R2} \tag{3}$$

Here γ is the surface tension of the NP dispersions, θ_{R1} and θ_{R2} receding contact angle of dispersion with the hydrophilic and hydrophobic patterned area, respectively. Δl_1 and Δl_2 are the effective lengths of different wettability. Second, the resistance force ($F_{\text{resistance}}$) is generated from Equations (4) and (5) (i.e., the adhesion force between NPs and substrate (F_{PS}) & TCL asymmetric retraction (ΔP)), which is expressed as[292,293]

$$F_{\text{resistance}} = A\Delta P + F_{PS} \tag{4}$$

$$F_{\text{resistance}} = A \int_{w1}^{w2} \gamma \left(\frac{1}{r} + \frac{1}{R}\right) dw + 6\pi R_{PS} \sqrt{\frac{G*}{E*} \Delta\gamma} \tag{5}$$

Here, A is the contact area on the substrate, w is the width of the liquid film, w_1 and w_2 are the stopping and starting positions of TCL, respectively, and r/R are local radii influenced by film width. R_{PS} is NP radius, G^*/ E^* is the average shear modulus/Young's modulus, and $\Delta\gamma$ surface energy of the particle and substrate.

The patterning morphology of NPs was obtained by balancing the driving ($F_{\Delta RCA}$) and resistance forces ($F_{\text{resistance}}$) dependent on the surface tension and nanoparticle ink concentration.[290] The diversified morphologies (e.g., line, triangle, square, hexagon, and octagon-shaped) were deposited on one single pinning pattern (Figure 8a$_1$). Figure 8a$_2$-a$_3$ shows the arrayed patterning of triangular-shaped microcolloidal crystals formed by three hydrophilic pinning points due to the asymmetric dewetting on the hydrophobic surface. The pinning of TCL at the hydrophilic region induced capillary flow from the hydrophobic to the hydrophilic region, which transported nanoparticles to pinning points (Figure 8a$_4$). The confinement of liquid formed the hexagonal and closely packed structures of NPs, which could yield higher functional properties during practical applications (Figure 8a$_5$-a$_6$).

The practical application of self-assembled patterns is limited because of the lower resolution. To address this, T. Manari et al. reported a high-resolution self-assembly strategy for Au metallic ink on a DSA template inspired by the Tokay gecko.[101] They have developed a two-step process via sequential photoirradiation and alkali rinsing to create hydrophilic regions on a hydrophobic polymeric substrate with enhanced surface properties (Figure 8b$_1$). The three main criteria for high-resolution self-assembly of NPs on DSA substrate include the following. i) The pristine substrate should repel the fluidic ink, ii) the ink should flow to the designated area, and iii) the ink should be firmly pinned onto the designated regions.[101] To deposit the NPs in designated regions, the interfacial free energy between the repellent region (E_A) and the designated region (E_B) should satisfy Equations 6 and 7.[1,2]

$$\Delta E = E_A - E_B > 0 \tag{6}$$

$$\Delta E = \left(\gamma_{AV} - \gamma_{LV} \cos\theta_A\right) R_{fA} + \left(\gamma_{LV} \cos\theta_B - \gamma_{BV}\right) R_{fB} > 0 \tag{7}$$

Here γAV and γBV are the solid surface energy at the repellent region (A) and designated region (B), respectively, θA and θB are the contact angles of NPs colloid on the corresponding surfaces, γLV is the liquid surface energy, and RfA and RfB are surface roughness at different areas. As per the above equations, the difference in surface energy (ΔE) can be increased by maintaining high surface roughness (R_f) for both regions and by decreasing the contact angle of the designated region (θ_B), which would improve the flow of NPs colloids towards the designated area.[101] For example, photoirradiation would improve surface energy to guide fluidic flow toward the modified surface, and alkali treatment would enhance the force of adhesion to strengthen the pinning effect for nanoparticle assembly. The π-junction Au metallic ink was swiped above the flexible DSA substrate using a coating bar and Au NPs were self-assembled on the designated region of the flexible substrate, as shown in Figure 8b$_2$. After the ink

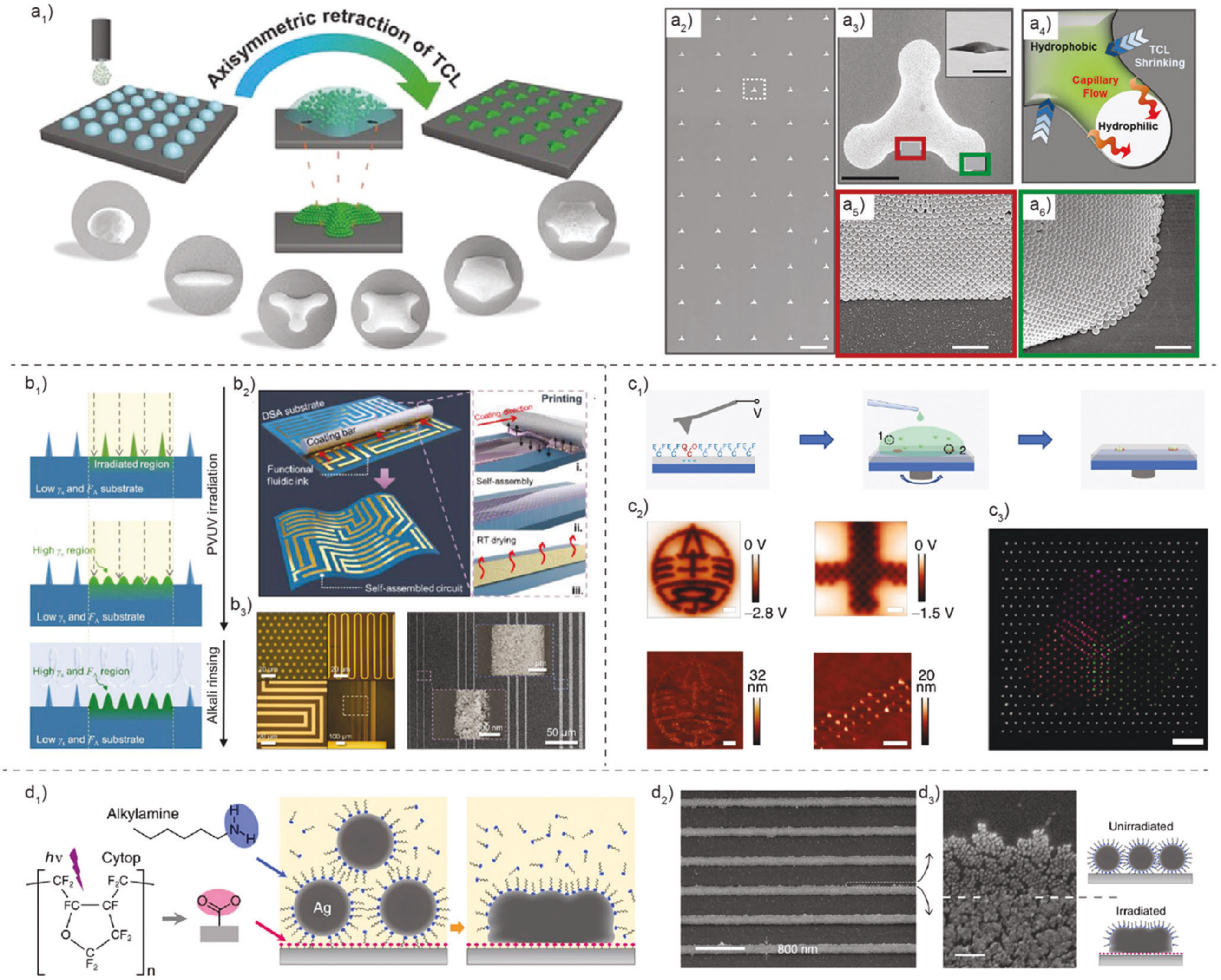

Figure 8. Assembly by chemically modified surfaces: a$_1$) schematic shows the strategy for manipulating poly(styrene-methyl methacrylate-acrylic acid) (P(St-MMA-AA)) microcolloidal crystal for surface patterning through hydrophilic and hydrophobic surface functionalization-induced asymmetric dewetting, a$_2$) the morphology of 3D microcolloidal crystal deposition (scale bar 200 μm), a$_3$) SEM imaging showing a top view of completely assembled patterns (scale bar 20 μm), a$_4$) the patterning mechanism for effective NP assembly, and a$_5$-a$_6$) the high-quality assembly of NPs at hydrophilic and hydrophobic regions (scale bars 10 μm). Reproduced with permission.[290] Copyright 2015, Wiley-VCH. b$_1$) Schematic of sequential manufacturing of dual surface architectonic (DSA) substrate consisting of parallel vacuum ultraviolet (PVUV) technique and alkali rinsing, b$_2$) schematic of patterning process obtained by bar coating of Au ink for the self-assembled circuits, and b$_3$) optical images showing different forms of the fabricated electrode and selective deposition (scale bars in left images of 20 μm except for the bottom right of 100 μm, and 50 μm for the right image with 3 μm for top inset and 500 nm for bottom inset). Reproduced with permission.[101] Copyright 2021, Wiley-VCH. c$_1$) Schematic illustration of an electric field-assisted surface-sorption nanoimprinting (EFASP) technique involving nanopattern template fabrication by high-voltage writing, surface modification (defluorinated on a fluorinated template), and site-specific NP deposition at defluorinated regions via the electrical trapping, c$_2$) the Kelvin probe force microscopy (KPFM) potential map and corresponding height profile via AFM (scale bars of 2 μm for left and 200 nm for right images, respectively), and c$_3$) the dark field microscopy image shows color pattern comprised of four types of NPs (the white color is γ-Fe_2O_3, magenta is $NaYF_4$:YbEr, green is $CsPbBr_3$ and red is CdSe@ZnS NPs, a scale bar of 10 μm). Reproduced with permission.[294] Copyright 2020, Springer Nature. d$_1$) Schematic of printing conductive NPs by chemisorption method and assembly mechanism, with the d$_2$) SEM imaging of printed patterns ((i.e., parallel lines with a line width of 0.8 μm and a scale bar of 5 μm), and d$_3$) a zoomed-in region of the printed silver line with fused and non-fused AgNPs (scale bar 100 nm). Reproduced with permission.[295] Copyright 2016, Springer Nature.

dried, 5 μm to 600 nm patterns of various shapes, such as dots, lines, and curves, were formed on the substrate with well-defined boundaries in a single printing process (Figure 8b$_3$).

The recent advancement in the colloidal synthesis of metallic, semiconductor, and dielectric NPs is desirable for the colloidal self-assembly of NPs at predefined positions via NP/substrate interactions.[296,297] For the nanopatterning of NPs with high precision requires the long-range particle-substrate attraction to deposit NPs on the substrate. Besides, firm short-range attractions are necessary to improve the adhesion of NPs at the designed location and counter interparticle interactions to avoid deposition at the undesired location.[197] For example, Z. Lu et al.

reported an electric field-assisted surface-sorption nanoimprinting (EFASP) technique that could print functional colloids with a 10–200 nm feature resolution to optimize these interactions.[294] This method used an AFM tip-based high-voltage (−40 to −90 V) writing process that decomposed the fluorine polymer surface and generated de-fluorinated patterns on the fluorinated substrate surface. After the generation of the electrostatic nanopattern, Perovskite $CsPbBr_3$ quantum dots dispersed in a non-polar solvent were applied on the surface by dip coating, spin coating, and brushing (Figure 8c$_1$). The NPs were attracted and adsorbed on the defluorinated surface due to electrostatic trapping and high local surface energy compared to the fluorinated area where no adsorption occurred due to the low surface energy of the fluoride substrate (Figure 8c$_2$). With the long-range electrostatic interaction, short-range surface adsorption, and low surface energy of fluorinated surfaces for NPs, EFASP enabled the site-specific patterning of NPs over a large area. The possibility of NPs adsorption in different areas was calculated using the Boltzmann-Gibbs distribution.[294]

$$P(r) \propto e^{-U(r)/k_{BT}} \tag{8}$$

Here P is the probability of NPs being at location r, U is adsorption energy, T is temperature, and k_B is the Boltzmann constant. This technique also displayed an ability to deposit multiple functional NPs by repeating writing/deposition cycles for photonic applications (Figure 8c$_3$).

Printing-based device production has gained considerable interest in different applications due to its low consumption of time, energy, and resources.[176] Thus, Hasegawa's group studied the technique of printing patterns with higher quality and resolution which was impossible to produce by conventional printing of the fluidic inks (i.e., screen and inkjet printing).[295] This work reported the chemical adsorption of silver (Ag) NPs on the predefined photoactivated region fabricated by masked vacuum ultraviolet (VUV) irradiation and blade coating. For this purpose, low-viscosity silver nanocolloids consisting of AgNPs encapsulated in alkylamine layers were coated on a photoactivate polymeric substrate with a pendant carboxylate group. A thin layer of AgNPs formed on the irradiated region of the polymeric surface after the coating and the unirradiated parts remained bare (Figure 8d$_1$). The silver layer was chemically bonded to the polymer substrate through amine-carboxylate coordination to form the self-fused silver layer. The electronic conductivity (1×10^5 S cm^{-1}) and adhesion strength of AgNPs film with substrate surface (5 MPa) were improved by low-temperature annealing (<80 °C).[295] As a result, the AgNP's density and resolution (800 nm) produced by printing via chemisorption were higher than the conventional physisorption phenomenon of fluidic inks (Figure 8d$_2$-d$_3$). The chemically modified template-based assembly approach could produce high-resolution and large-area electronics (e.g., circuits) with submicron features and robust NP adhesion to the substrate surface.

3.5. Mechanically Wrinkled Surfaces for Nanoparticle Assembly

The chemically modified surfaces for nanopatterning of NPs have many advantages but may suffer from low yield and require subsequent fractionation. However, NP assembly in many applications may demand a simple approach with strict nanoscale precision (e.g., dry processing without chemicals). Commonly in industry, nanoscale resolution surfaces have mature fabrications with nanolithography-based methods, including FIB, E-beam lithography, and nanoimprinting, due to their excellent pattern resolution, reproducibility, and flexibility (Table 4).[298,299] However, these techniques are multistep, costly, and not easily accessible. Alternatively, surface wrinkling is an efficient way to create micro/nanoscale patterned surfaces due to its simplicity, versatility, cost-effectiveness, high throughput, and scalability. For example, surface wrinkling happens when compressive strain (ϵ) > materials critical strain (ϵ_c), without any expensive apparatus and stringent experimental conditions.[300] In addition to above mentioned mechanical pre-straining mechanism, S. G. Lee's review paper has summarized other techniques such as chemical swelling, and thermal annealing to fabricate wrinkled surfaces.[301,302] In chemical swelling, the interaction of chemical solvent with polymeric material induces volumetric phase transition with reversible swelling or shrinking under external conditions, such as temperature or composition of solvents.[303,304] Swelling of the bilayer system generates biaxial residual stress on the surface of the polymeric film which results in the formation of wrinkles.[305] Thermally induced wrinkles are formed on bilayer systems when the thermal stresses are developed due to the difference in thermal expansion coefficient between rigid and elastic layers.[306,307] Thus, the difference in mechanical stiffness, coefficient of thermal expansion, and solvent swelling between rigid and soft bilayers in the presence of external stimuli, such as mechanical stretching/compressing, heating, and solvent treatment, can be utilized to generate the strain mismatch for the surface wrinkling phenomena.[308–310]

In the mechanically induced method, the wrinkled substrate was processable by mechanical stretching and plasma treatment – an elastomeric stamp is stretched by mechanical force and subjected to a plasma treatment, followed by controlled relaxation (**Figure 9**a$_1$).[311] During the tension state, the flat PDMS substrate was treated with oxygen plasma for varying durations resulting in the formation of stiff-oxidized skin, which can be programmable with varying thickness for desirable modulus.[312] The stretched samples were released to induce compressive strain (ϵ) on the oxidized surface, which is more resistant to contraction than the elastomeric substrate below it, forming the sinusoidal-shaped wrinkling surface. A small-level strain formed open channels with specific wavelength and amplitude on the substrate surface. Whereas at a high-level strain, the substrate surface morphology changed from wrinkles to closed folds with nanoscale diameters.[313] The characteristic dimensions of the channels, such as wavelength (λ), amplitude (A), and diameters (d), can be dependent on the duration of oxygen plasma treatment (film thickness) and mechanical strain levels.

The compressive force generated on the top surface of the film (f) having a thickness (h) and width (w) that is strongly attached to the elastomeric substrate (s) is given by[313]

$$F = E_s \left[\left(\frac{\pi}{\lambda}\right)^2 \frac{wh^3}{3\left(1 - \nu_s^2\right)} + \frac{\lambda}{\pi} \frac{E_f\ w}{4\left(1 - \nu_f^2\right) E_s} \right] \tag{9}$$

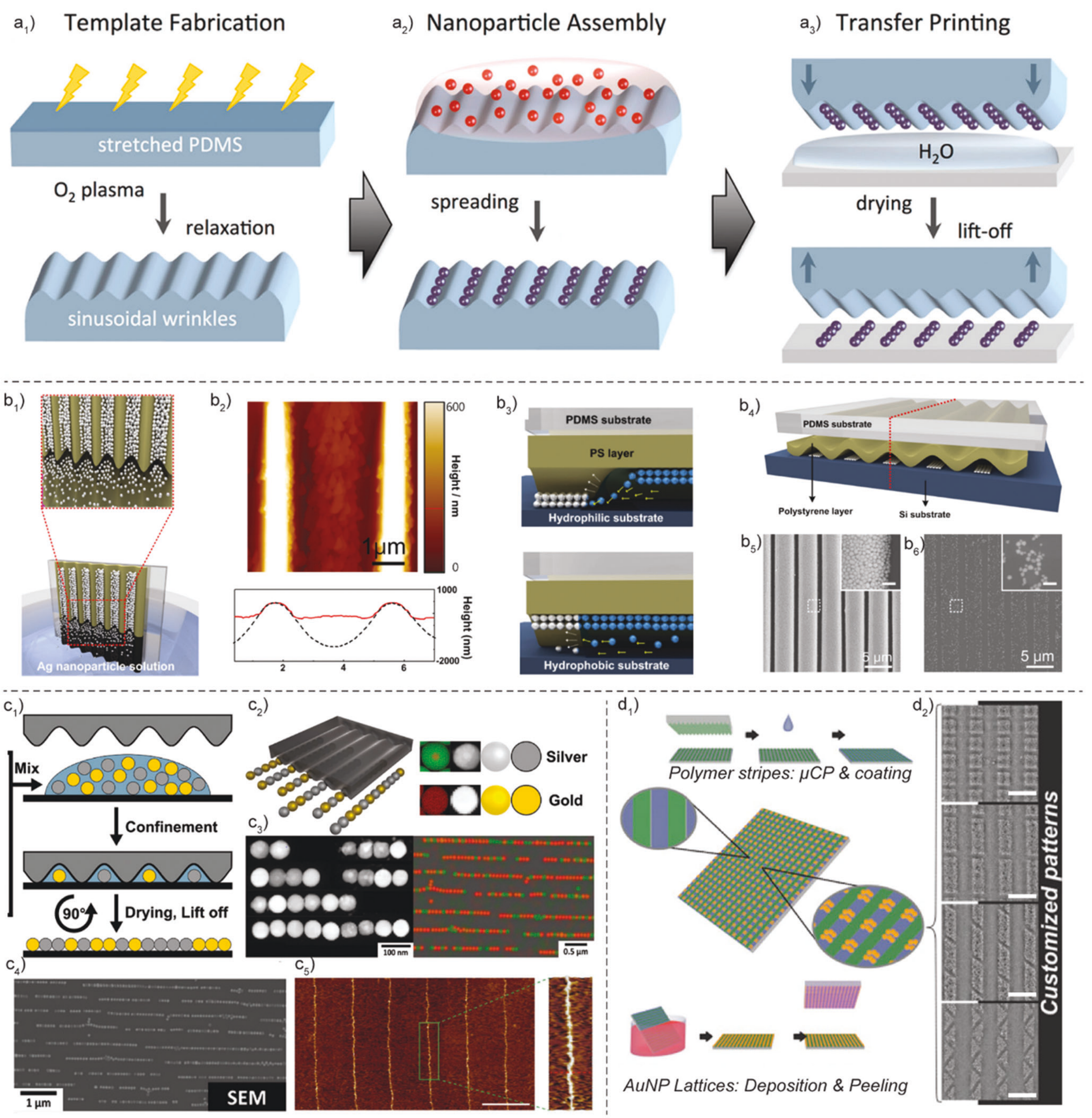

Figure 9. Wrinkled template-based NP assembly: a_1) a schematic representation of wrinkled template fabrication via the plasma oxidation of a stretched PDMS film before the relaxation, a_2) assembly of NP chains at predetermined sites, and a_3) the assembled NPs were transferred onto flat substrates by wet contact printing. Reproduced with permission.[311] Copyright 2014, American Chemical Society. b_1) Schematic illustration of the fabrication process of Ag NP-arrays via the dip-coating process, showing strong capillary forces occurring at the trough of the buckling structure of polystyrene (PS) substrate, b_2) the AFM image of the Ag NP assembled in the trough and its height profiles that show the cross-sectional topography, b_3) schematic showing assembly mechanism of Ag NPs on the hydrophilic and hydrophobic PS surfaces, and b_4) schematic of the transfer process of Ag NP arrays on the flat substrate and SEM images of the Ag NP line transferred on b_5) hydrophilic and b_6) hydrophobic surfaces. Reproduced with permission.[219] Copyright 2021, American Chemical Society. c_1) The assembly of Ag and Au NPs via the confinement of a suspension droplet between the silicon wafer and PDMS wrinkled templates, c_2) stochastic assembly was observed after drying and lifting of templates, c_3) the heterogeneous composition of the Ag-Au NP mapping was observed from scanning transmission electron microscopy (STEM)/SEM/EDS, and c_4) SEM imaging of Ag-Au NP assembly. Reproduced with permission. Copyright 2021, Wiley-VCH. c_5) Directed assembly of DNA molecules into nanowires by wrinkled template-assisted capillary bridging between PDMS template and flat substrate (scale bar 5 µm). Reproduced with permission.[317] Copyright 2022, Wiley-VCH. d_1) Schematic illustration of fabricating Au-NP arrays with microcontact printing (µCP) of a wrinkled PDMS substrate used as a stamp, and d_2) SEM images of Au-NPs patterns of different orientations formed by different peeling angles (all scale bars 2 µm). Reproduced with permission.[318] Copyright 2020, Wiley-VCH.

Here E and ν are Young's modulus and Poisson's ratio of the substrate (s) and film (f), respectively. Equations (10) and (11) of λ and A caused by buckling instability are obtained by minimizing the total energy of the film-substrate system ($(dF/d\lambda) = 0$).[279,280,281]

$$\lambda = 2\pi h \left[\frac{\left(1 - \nu_s^2\right) E_f}{\left(1 - \nu_f^2\right) 3 E_s} \right]^{1/3} \tag{10}$$

$$A = h \left[\frac{\varepsilon}{\varepsilon_c} - 1 \right]^{1/2} \tag{11}$$

The wavelength of the winkle is directly proportional to film thickness and inversely proportional to the substrate stiffness (i.e., E_s). The wrinkle amplitude is dictated by ϵ and h. In addition to the uniaxial compression, the elastomeric film was subjected to isotropic, equi-biaxial compression, and localized strain, which modified the 1D wrinkle morphology to disorder wavy, labyrinths (disordered zigzag wrinkle), herringbones (a periodic array of zigzag wrinkles), checkerboards and spoke/target-like patterns.[310,312]

These wrinkled substrates have been useful for directed self-assembly generated NP deposition in desirable fashions. The NPs can be patterned onto substrate surfaces by solution deposition approaches, including the above-mentioned spin coating, droplet casting, and dip coating. During the evaporation of the solvent, NPs get confined within the wrinkled surface and result in the formation of a sub-monolayer, a monolayer, or a multilayer on the substrate surface (Figure 9a$_2$).[311] These patterned structures were transferrable on the flat substrate to provide access to a wide range of applications (Figure 9a$_3$).[311] For example, T. Lee et al. reported a simple approach to assemble Ag nanoparticles onto the wrinkled substrate by dip coating for optical, electrical, and biosensor applications. Firstly, a wrinkled substrate was prepared by applying uniaxial mechanical stretch on PDMS-PS film, and the surface was treated with oxygen plasma to improve the NPs' adhesion (Figure 9b$_1$).[319] Then, Ag nanoparticles were deposited into the trough of the template due to capillary forces, as shown in the AFM image and cross-sectional height profile in Figure 9b$_2$. The well-defined Ag NP arrays were transferred on the silica substrate with good wettability (contact angle 10°) with the assistance of capillary forces from the water (Figure 9b$_3$). The transferred pattern displayed uniform and periodic width of Ag NPs arrays as compared to the hydrophobic substrate (contact angle 106°) (Figure 9b$_4$-b$_6$).

The wrinkled templates were used for the assembly and patterning of NPs on the flat substrate without the transferring steps, as described in Figure 9c. Here, A. Fery et al. demonstrated the well-aligned assembly of heterogeneous NPs (i.e., Ag-Au) into chains of various lengths via confining suspension of particles at an interface between the PDMS wrinkle template and flat silicon wafer substrate (Figure 9c$_1$).[316] The particle suspension with different ratios of Ag-Au NPs was cast on the substrate. During the drying process, the evaporation-induced and steric forces assembled the NPs into densely packed lines (Figure 9c$_2$-c$_4$). This allowed the assembly of a statistical combination of $>10^9$ NPs into lines with an interparticle distance of <1 nm at the confined regions between the PDMS template and silicon substrate.[316] Similarly, M.W. Moon et al. reported the bottom-up assembling of DNA molecules into 2 nm thin nanowires.[317] They used the wettability contrast methods comprising the super hydrophilic PDMS wrinkled substrate on top of the hydrophobic flat bottom substrate to confine DNA molecules and formed linear structures on a substrate after the evaporation (Figure 9c$_5$). This wrinkled template-assisted self-assembly approach is useful for assembling general organic and inorganic biological particles and developing functional nano or microstructures for plasmonic, optical, and sensing device applications.[301,320]

As an alternative to lithographic techniques, wrinkled stamps show potential for micro-contact printing for patterning NPs without the requirement of sophisticated instruments. For example, A. Boker et al. demonstrated the use of a wrinkled PDMS template as a stamp for patterning nanoparticles with a series of microcontact printing and surface coating steps.[318] This patterning approach consisted of four major steps. i) First, surface patterning of oligomeric PDMS (o-PDMS, which was unreacted PDMS formed during the curing process of PDMS) wrinkled substrate on the Si wafer surface by simple microcontact printing. ii) These periodic stripe hydrophobic patterns were functionalized with the charged hydroxyl functional poly(2-vinyl pyridine) (P2VP-OH) via spin coating, washing, and annealing, which generated alternating hydrophobic (o-PDMS) and hydrophilic (P2VP-OH) stripes with different electrostatic surface potential.[318] iii) Subsequently, negatively charged gold nanoparticles were deposited on partially positively charged P2VP and neutral o-PDMS patterns (Figure 9d$_1$). The PDMS-P2VP patterns fabricated from wrinkled PDMS stamps with precisely tuned groove dimensions served as guiding templates for the assembly of AuNPs, which adhered to the P2VP domains due to electrostatic interactions. iv) Lastly, complex geometries, such as quadrangular or triangular could be achieved by selective peeling of AuNPs using another wrinkled PDMS stamp at different rotation angles (i.e., 45–90°) (Figure 9d$_2$). This approach may serve as a useful tool for fabricating highly sophisticated NPs patterning of various materials, shapes, and functionality for broad applications.

3.6. Physically Controlled Polymer Morphologies for Template Effects

Block copolymer (BCP) assembly offers an interesting strategy to create a pattern of micro to nanometer length scale.[243,321] BCP consists of two or more chemically distinct polymer segments linked by covalent bonds, which are attractive scaffolds for template-based patterning of NPs because they can spontaneously assemble into diverse nanostructures.[322] The BCP forms distinct morphologies, such as layered structures, bicontinuous gyroid structures, hexagonally packed cylinders, and body-centered cubic packed spherical domains depending on the Flory-Huggins interaction parameter and volume fraction of the blocks.[323,324] These surface morphologies are ideal for NPs confinement and patterning for functional nanoscale structures by selective surface modification and removal of one component patterning (**Table 5** includes a few examples of NPs patterning via BCP).[325,326] The NPs patterned using BCP templates via in-situ and ex-situ approaches: in situ approach uses the BCP tem-

Table 5. Summary of block-co-polymer templating techniques for nanopatterning of nanoparticles.

Block copolymer	Morphology	Nanoparticles	Reference
PS-*b*-PMMA	Lamella	Au	[332]
PS-*b*-PMMA	Hexagonal	Au	[44]
PS-*b*-PMMA	Lamella	Co	[333]
PS-*b*-PMMA	Cylinder	CdSe	[334]
PS-*b*-PtBA	Sphere	Pt, Ag, PbS	[335]
PS-*b*-P2VP	Spherical micelles	Au	[336]
PS-*b*-P2VP	Lamella	Fe, Fe-Co, Co-Ni	[337]
PS-*b*-P2VP	Cylinder	Au, Pt, Pd	[338]
PS-*b*-P2VP	Spherical micelles	TiO_2	[339]
PS-*b*-P2VP	Spherical micelles	Pt, Pd, Co, Ni	[322]
PS-*b*-PFEMS	Cylinder	Carbon nanotubes	[340]
PS-*b*-PFEMS	Cylinder	Fe_2O_3	[341]
PS-*b*-PI	Sphere	Metal nanodots	[342]
PMTCDD-*b*-P2NB	Sphere	PbS, CdS	[343]

Abbreviations: Ag, silver; CdSe, cadmium selenide; Co, cobalt; Fe, iron; Fe_2O_3, iron oxide; Ni, nickel; P2NB, poly(substituted-2-norbornene); P4VP, poly(4-vinyl pyridine); PbS, lead sulfide; Pd, palladium; PFEMS, poly(ferrocenylethylmethylsilane); PI, polyisoprene; PMTCDD, poly(methyltetracylododecene); Pt, platinum; PtBA, poly(t-butyl acrylate); TiO_2, titania.

plates for NPs patterning by electrodeposition, ALD, CVD, and plasma reduction approach.[327] In the ex-situ approach, the BCP film is used as a template for NPs deposition from their solution by spray, spin coating, and dip coating, hence the most widely used technique for NPs patterning at pores of BCP films.[328] The NP array generated by the BCP depends on the nature of the template, surface chemistry of nanoparticles, surface tension of the nanoparticle solution, and driving force of assembly.[44] Herein, we described a few techniques as examples, mainly based on BCP to produce functional nanoparticle structures on patterned templates.

The dry etching process is a simple, effective, and anisotropic technique to fabricate the block copolymer templates.[329] The polymer can be easily removed and modified into nanopores and nanochannels without losing the structural integrity, which shows fascinating properties for NPs localization and patterning. For example, T. He et al. showed the combination of top-down and bottom-up strategies for the self-assembly of aqueous Au NRs with plasma-etched polystyrene-b-poly(methyl methacrylate) (PS-*b*-PMMA) BCP template (**Figure 10**a_1).[330] Due to the chemically different structures of the two polymers, the PS-*b*-PMMA was selectively etched with etch selectivity of PS to PMMA ≈2 by air plasma etching technique. After etching, the well-aligned vertical lamellas emerged from copolymer thin films with remaining PS side walls of a 48 nm period (Figure 10a_2). Au NRs solution was spin-coated on the plasma etched block copolymer template, which showed that particles were confined to the topographical pattern of the etched PMMA domain (Figure 10a_3). The obtained NPs array of Au NRs with side-by-side and end-to-end assembly was further transformed into Au nanowires by post-etching of the remaining PS (Figure 10a_4). NPs were deposited into densely packed arrays for large-area patterning via physical confinement and capillary forces. Many nanoscale elements or molecules, such as proteins, DNA, and viruses, rely on an aqueous environment, thus, this approach could be a promising method for nanopatterning and bio-templating.[322,331]

Even though different approaches are being developed for NPs self-assembly with BCP, obtaining patterned regions with desired shapes by approaches other than chemical patterning and localized etching is required. The chemical patterning is a multistep process and localized etching generated undesired resides on the template surface. To address this, R. Shenhar et al. showed the use of topographical features to control the BCP (PS-*b*-PMMA) film thickness which enabled them to create a domain with dual surface morphology (Figure 10b_1).[344] The differential patterning morphology was controlled by the combined effect of strong thickness confinement and substrate sensitivity without any influence of lateral width, which was also proved from simulation studies (Figure 10b_2).[344] Figure 10b_3-b_4 shows the BCP film on the plateaus with a dot pattern and featureless appearance on the trench region of the substrate fabricated with electron lithography. The featureless patterns were formed due to the parallel orientation of lamellae to the trench floor, and further reducing the film thickness, lamellae changed the orientation from parallel to perpendicular to the substrate, which generated dot morphology.[344] Another complex morphology was obtained by changing the orientation of the domain concerning substrate from parallel to perpendicular by incorporating Au NPs into the BCP solution before coating. The combined effect of i) the tendency of the PMMS domain to wet the substrate and ii) the tendency of Au NPs to segregate at the film surface to lower surface energy caused the lamellae to orient along the normal direction to the substrate. Figure 10b_5 shows the patterning of 13 nm thiol-terminated Au-PEO NPs on the patterned PS-*b*-PMMA block copolymer substrate, which showed potential for complex patterning of different types of fillers.

Various advanced techniques were studied in the BCP template-based patterning of NPs. However, it is still challenging to obtain highly ordered, multiscale patterning. Thus, W. Jiang et al. reported a well-controlled arrangement of Au NPs into ordered structures, such as rings, and hexagonal honeycomb structures and their combinations.[345] Here, sheet-like 2D scaffolds of hexagonally packed poly(4-vinyl pyridine) (P4VP) cylindrical nanodomains (Figure 10c_1) were fabricated in polystyrene (PS) matrix by flat emulsion droplet confined assembly. In this approach, the evaporation of chloroform from the BCP/chloroform emulsion droplet caused the collapse of a droplet from a rugged to smooth surface, which generated phase separation of the PS and P4VP domain. The geometry and stability of internal structures of P4VP 2D scaffolds depended on different factors, including an asymmetric collapse of emulsion droplet and reduced interfacial surface energy by the cetyltrimethylammonium bromide (CTAB) surfactant addition, CTAB concentrations, and the block ratios.[345] The prefabricated P4VP scaffolds caused selective adsorption of tetrachlorocuprate trihydrate ($hAuCl_4.3H_2O$) due to electrostatic interaction between Au precursor and P4VP monomers (Figure 10c_2). The Au precursor aqueous solution was adsorbed on BCP sheets by centrifugations followed by electron irradiations to chemically reduce Au precursors into Au NPs. The scanning transmission electron microscopy (STEM)/ transmission electron microscopy (TEM)/ energy dispersive spectroscopy

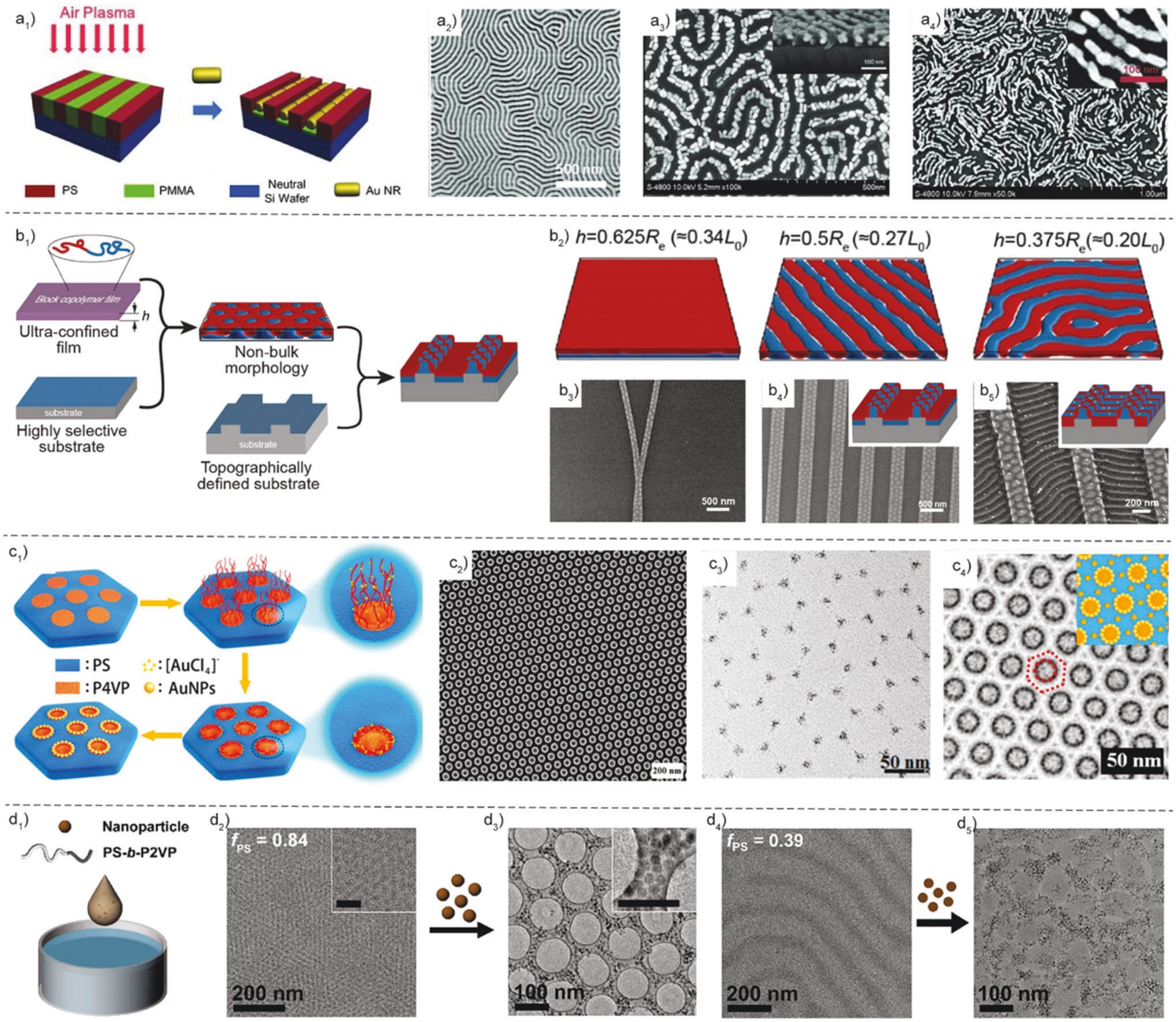

Figure 10. Copolymer template-based NP assembly: a_1) schematic representation showing steps for patterning Au NRs on polystyrene-b-poly(methyl methacrylate) (PS-*b*-PMMA) BCP templates by the plasma etching process and Au NR deposition, SEM images of a_2) PS-*b*-PMMA BCP thin film formed after twice air plasma etching (scale bar 500 nm), a_3) Au NRs deposited on plasma etched PS-*b*-PMMA template from 43 mg mL^{-1} Au NR colloids (scale bar 500 nm) with the insert showing the cross-section morphology (scale bar 100 nm), and a_4) after the post-etching of the template showing continuous, end-to-end assembly for Au NR-composed arrays (scale bar 1 µm). Reproduced with permission.[330] Copyright 2013, Wiley-VCH. b_1) Schematic illustration of the coating process in the ultra-confined regime on selective morphological substrates (PS and PMMA domains are depicted in red and blue, respectively), b_2) simulation results of the assembly morphology of lamellar BCP thin films of different thicknesses (h) with R_e denoting the average end-to-end distance of the copolymer chain, b_3) BCP film assembled on substrates with irregular features, b_4) a dot-patterned region spaced by patternless domains, and b_5) the irregular featured patterns with co-assembled 13 nm thiol-terminated Au-PEO NPs. Reproduced with permission.[344] Copyright 2019, American Chemical Society. c_1) Schematic illustration showing the formation mechanism of the array of the AuNPs nanoring on the polystyrene-block-poly(4-vinyl pyridine) (PS-*b*-P4VP) scaffold surfaces, c_2) a darkfield STEM image showing large-scale assembled arrays of Au nanoring, c_3) a TEM image of the Au-NPs arranged in a long-range hexagonal honeycomb morphology by confined co-assembly, and c_4) a TEM image and an inset cartoon showing a combined structure of hexagonal honeycomb and ring-like morphology of Au-NPs on the BCP scaffold surfaces. Reproduced with permission.[345] Copyright 2019, American Chemical Society. d_1) Schematic illustration of the air-liquid interfacial self-assembly, d_2-d_3) TEM images of the PS-*b*-P2VP (f_{PS} = 0.84) films formed without and with PS nanoparticles, and d_4-d_5) TEM images showing the assembly structure of PS-b-P2VP (f_{PS} = 0.39) films without and with iron oxide (Fe_3O_4) nanoparticles. Reproduced with permission.[346] Copyright 2020, American Chemical Society.

(EDS) imaging showed the formation of reduced Au NPs arranged into nanoring, hexagonal honeycomb, and combined structures with the periodic arrangement (Figure 10c$_3$-c$_4$).

Self-assembly of BCP and NPs at the air-liquid interface generates highly ordered and easily transferable composite film with the functionality of nanoparticles and mechanical stability of the polymer phase.[347] For example, S.J. Park et al. reported the self-assembly of iron oxide and polystyrene-block-poly(2-vinyl pyridine) (PS-*b*-P2VP) at the air-water interface with interestingly nanoscale architectures.[346] Depending on the volume fraction of PS nanoparticles, they were organized into a hexagonal sphere and cylindrical arrays on the water surface, as shown in Figure 10d$_1$. However, when NPs were incorporated into the BC film, the morphology changed between i) the hexagonal sphere to porous honeycomb-like network structure for large volume-fraction of PS (Figure 10d$_2$-d$_3$) and ii) the cylinder to pseudo-spherical arrays for low volume fraction of PS without formation of pores (Figure 10d$_4$-d$_5$). The combined effect of NPs and higher hydrophobic phase in BCP showed the formation of pores lined with hydrophilic P2VP with iron oxide NPs formed in the PS domains (Figure 10d$_3$). The sphere-to-pore transition resulted when a toluene droplet containing NPs and BCP was placed on the water surface, and the evaporation of toluene emerged from the porous NPs network which developed into an ordered honeycomb structure with complete toluene evaporation.[346] This self-assembly approach could be suitable for NPs of different sizes and types, such as quantum dots and quantum rods, for various applications.

4. Applications

NP patterning from template-less self-assembly and template-based directed assembly is an attractive method for fabricating flexible nanoparticle features or matrix/nanoparticle composites. When designing structures, the desired fabrication strategy should have low-cost, high-throughput, minimum feature size, and large-scale production rates to generate desired geometries and functional properties in different applications. For example, accurate patterning of NPs on predetermined sites is crucial for high-performance devices, while customized deposition and transport of NPs with acceptable production rates may be critical for personalized medicine.[35,133,348] Various strategies developed for precisely and flexibly controlling the NP patterning have been described in previous sections. These ordered NP organizations into periodic 1D, 2D, and 3D structures have broad applications, such as microelectronics,[349–352] optoelectronics,[353–357] plasmonics,[68,358–360] anticounterfeiting,[179,361–363] magnetic microstructures,[364–367] energy storage systems,[368–370] sensors,[371–375] biological systems,[376–380] drug delivery,[31,381–383] photocatalysis,[168,384–386] and displays.[9,68,387] Therefore, we selected a few examples to review below.

4.1. Microelectronics

The solution-based deposition of conductive NPs, such as metal NPs, CNTs, CNFs, MXene, reduced graphene oxides (rGO), and their patterned structures, has been exploited for microelectronics applications.[10,70,145,388] For example, T. Minori et al. displayed the assembly of Au NPs on the chemically modified high-resolution circuits for organic thin-film transistor (OTFT) arrays as electrode materials (**Figure 11**a$_1$).[101] The performances of the device depending on the linewidth and ink concentration of assembled structures were investigated (Figure 11a$_2$). They obtained 25 wt.% AuNPs printed lines of 2 μm widths exhibiting the low resistivity (14.1 ± 0.6 μΩ cm) with this property close to pure Au (e.g., in the order of μΩ cm). The performance for the OTFT devices showed the linear relationship of drain-source (D/S) current (I_{DS}) and voltage (V_{DS}) until the saturation with V_{DS} beyond the pinch-off point (Figure 11a$_3$). This behavior suggested the free charge carrier distribution in the OTFT device was uniform with limited charged defects. Another application of densely patterned Ag-coated NP rods fabricated by crack engineering was demonstrated by Xu Deng et al.[130] They used colloidal nanostructures as a probe for signal amplification and detection of trace molecules for SERS detection. The SERS spectra showed the detection of 10^{-8} M Bis-phenol A (BPA) due to the formation of 3D plasmonic structures, which provided abundant hot spots for better SERS performance (Figure 11b$_1$) that is usually related to highly ordered materials or structures.

The traditional organic electrochemical transistor (OECT) devices relied on conductive materials for high sensitivity but ordered metal particles were limited by complex synthesis and modification steps. Hence, R. He et al. have reported the OECT device as a DNA biosensor with the interacted hybridization chain reaction for signal amplification at low cost and easier fabrication.[389] Here, the Au NPs were electrochemically deposited on the Au gate electrode, and negatively charged double-stranded DNA was connected to the gate electrode by hybridization (Figure 11c$_1$). The state and length change of DNA could increase the effective gate voltage offset of the OECT device up to 35 mV (Figure 11c$_2$). Additionally, the device displayed a linear relationship between the effective gate voltage offsets and the target DNA concentration in the range of 0.1 pM to 1 nM with a slope of 42 mV per decade (Figure 11c$_3$).

Another microelectronic application is sodium-ion capacitors (SICs) which are in high demand because it displays the advantages of both sodium-ion batteries and electrochemical capacitors. Y. L. Chueh et al. have reported the fabrication of SIC by assembling Mo_2C nanosheets on the surface of Mo_2C NPs via hydrolysis and calcination methods.[390] The assembled Mo_2C nanosheets as an anode were coupled with commercial activated carbon (AC) cathode (Mo_2C/AC SIC), which delivered a power density of 112 W kg^{-1} at a high energy density of 76.1 Wh kg^{-1} with a wide potential window (0-4.5 V) (Figure 11d$_1$-d$_2$). In addition, SICs displayed excellent cyclic behavior with a retained capacity of 83% after 4000 cycles (Figure 11d$_3$). The improved performance was derived from the well-interconnected structures, which would limit the volume change and increase the number of ion-accessible sites, resulting in improved charge transport kinetics.[390]

Electronic circuits without any semiconducting NPs can be easily created by metal NPs that are suitable for chemical processing and functionalization to achieve the desired functional properties. To demonstrate this, B. A. Grzybowski et al. fabricated a chemoelectrical device by drop casting Au NPs functional-

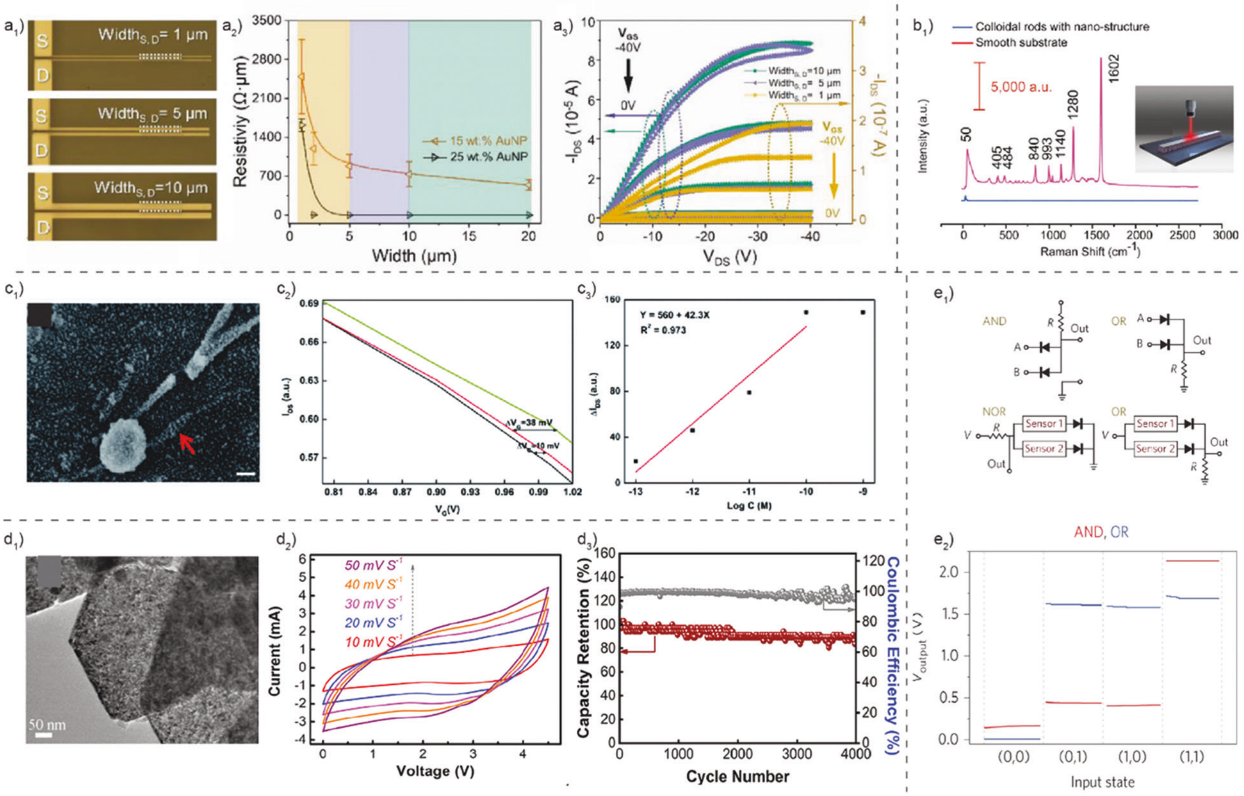

Figure 11. a$_1$) Optical image of Au NPs patterning-based source-drain (S/D) electrode circuits with different electrode widths, a$_2$) the electrical resistivity as a function of the ink concentration and printed line width, and a$_3$) output I-V characteristics of organic thin-film transistor (OTFTs) for different electrode widths. Reproduced with permission.[101] Copyright 2021, Wiley-VCH. b$_1$) Surface-enhanced Raman spectra (SERS) spectra obtained from 10^{-8} M bis-phenol A (BPA) solution on an Ag-coated nanostructured probe. Reproduced with permission.[130] Copyright 2021, Wiley. c$_1$) An SEM image of hybridized DNA on the surface of electrochemically deposited Au NPs on an Au electrode (scale bar 100 nm), c$_2$) effective gate voltage (I-V) offset of organic electrochemical transistors (OECT) corresponding to the target DNA (1 pM, green) and mismatched DNA (1 pM, red) as compared to the control sample (black), and c$_3$) the gate voltage shifts and offsets of the transfer curve based on the concentration of target DNA (from 0.1 pM to 1 nM). Reproduced with permission.[389] Copyright 2021, The Royal Society of Chemistry. d$_1$) A TEM image of lamellar Mo_2C nanosheets, d$_2$) cyclic voltametric (CV) curves of the assembled Mo_2C/activated carbon sodium-ion capacitors (SIC) at different scan rates, and d$_3$) cyclic stability of SIC at a current density of 1 A g^{-1}. Reproduced with permission.[390] Copyright 2019, American Chemical Society. e$_1$) Thermoelectric circuits consisting of Au-deposited resistors, diodes, and sensors with the performance characteristics of AND, OR, and NOR logic gates, and e$_2$) performance characteristics of a device consisting of diode and resistor (i.e., input 0/1 represent 0/2 V and absence/presence of environmental signals, e.g., humidity, gas, and metallic ions). Reproduced with permission.[391] Copyright 2016, Springer Nature.

ized with charged organic ligands from methanolic solution onto an insulted substrate or a metallic electrode.[391] The device consisted of Au NPs components, such as resistors, diodes, and sensors assembled in AND, OR, and NOR logic gates (Figure 11e$_1$). The device responded to environmental conditions (e.g., humidity, gas, and metallic ions) depending on the ionic gradient of the mobile counterions surroundings and provided output characteristics of AND, OR, and NOR circuits.[391] The circuit responded to the output as a “0” state and a high “1” in the absence and presence of the environmental signals, respectively (Figure 11e$_2$).

4.2. Optoelectronics

Nanoparticle patterning has broad applications in optoelectronics, such as photoresistors, phototransistors, photomultipliers, charge-coupled imaging devices, touch screens, liquid crystal displays, photodiodes in solar cells, and light-emitting diodes (LEDs).[353,392–396] Hence, the choice of appropriate patterning and deposition techniques is as important as the nanoparticle itself. Among many optical nanomaterials, quantum dots possess unique optoelectronic properties, such as high brightness, narrow emission spectra, extensive color tunability, high quantum yield, and good stability, thus suitable for next-generation wearable displays, which are required to produce high pixel density due to significant lower viewing distance.[397–400] Thus, Y. S. Jung et al. presented the immersion transfer printing (iTP) techniques for solution-based deposition, patterning, and printing of QDs capped with oleic acid on templates via a programmed wetting/dewetting mechanism.[397] iTP produced a diverse range of QD arrays with different morphologies and resolutions (e.g., single QD resolution, 350–5 μm line width, and the entire film).[397] **Figure 12**a$_1$–a$_3$ shows confocal microscope images of polychromatic QD arrays fabricated by sequential repetition of the iTP process for red, green, and blue pixels using a mask aligner.

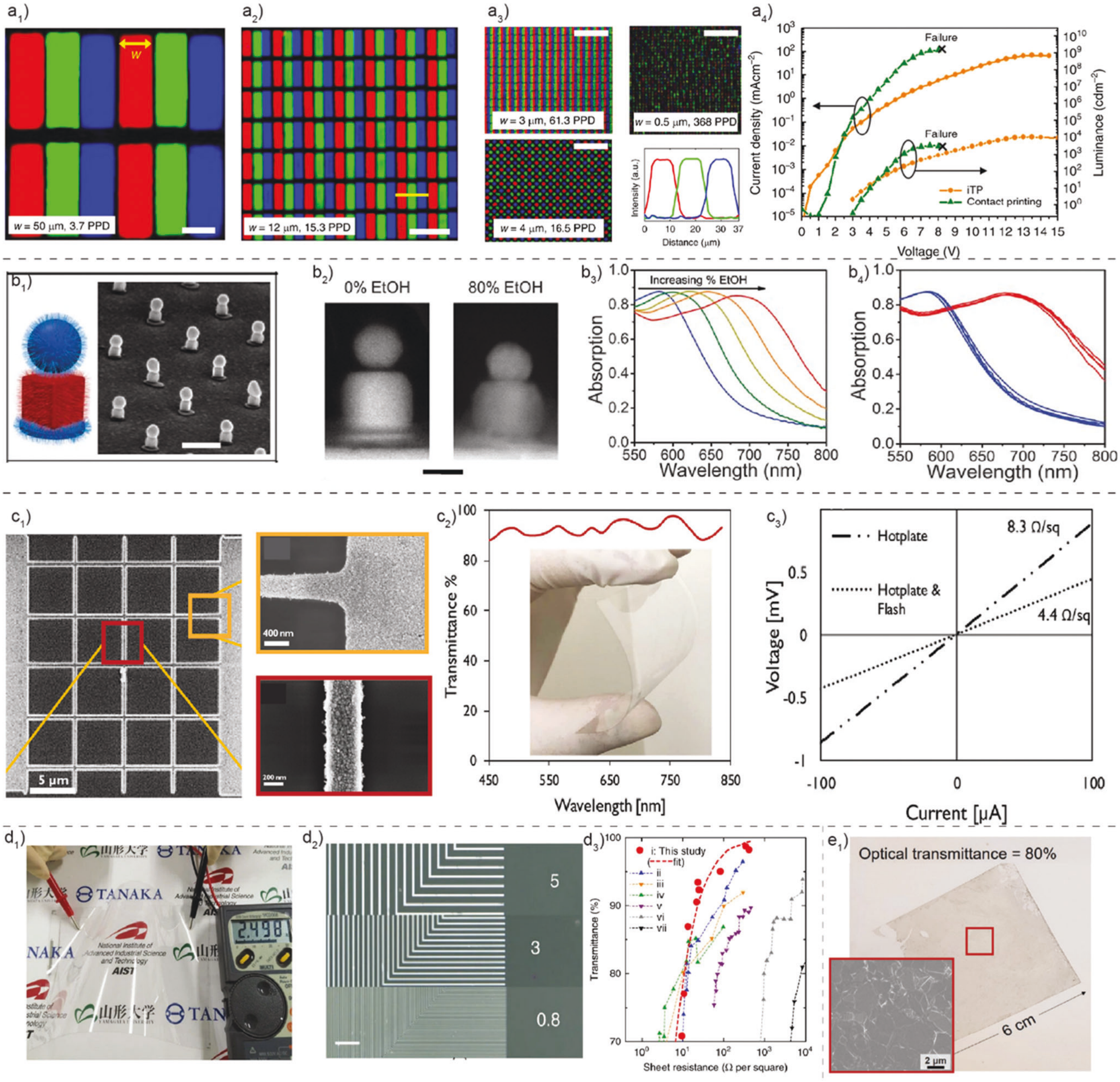

Figure 12. a_1-a_3) Confocal fluorescence images of the patterned red, green, and blue (RGB) arrays with a resolution of 3.7 pixel-per-degree (PPD) with a_3) the RGB intensity profile plotted across a single pixel of the QD array in the sample of a_2) marked with a yellow line (all scale bars 50 µm in a_3, with a wide resolution range from 16.5 to 368 PPD), and a_4) the current density-voltage-luminance characteristics of a monochromatic green light-emitting diodes (LED) device fabricated using iTP. Reproduced with permission.[397] Copyright 2020, Springer Nature. b_1) An SEM image of DNA-functionalized Au NP-containing architecture showing the NPs of controlled size and shape being assembled in a layer-by-layer manner in the order of sphere-cube-disk (scale bar 300 nm), b_2) cross-section SEM images of an Au NPs sphere-cube-disk structure after immersing in 0% and 80% EtOH in H_2O, respectively (scale bar 50 nm), b_3) the absorption spectra for samples immersing with 0–80% EtOH in H_2O, and b_4) five cycles of optical spectra for samples immersing with 0% and 80% EtOH in H_2O. Reproduced with permission.[30] Copyright 2018, Science. c_1) SEM images of micropatterned Ag NPs in nanoscale grid patterns on a glass wafer, c_2) the optical transmittance spectra of the Ag NP-based grid electrode, and c_3) I-V characteristics of the same electrode after sintering with different techniques (i.e., hot plate only and hotplate & flash). Reproduced with permission.[402] Copyright 2019, Wiley-VCH. d_1) A photograph of the 18 cm-wide flexible touch screen sensor fabricated with the polyethylene terephthalate (PET) being the substrate, d_2) an optical micrograph of printed parallel line patterns consisting of Ag NPs with different line widths of 5, 3, and 0.8 µm (scale bar 50 µm), d_3) the transmittance versus sheet resistance of patterned Ag NPs with different line widths in (d_1) shown as curve (i) and its comparison with transparent conducting films (i.e., (ii) copper NWs, iii) indium tin oxide (ITO), iv) Ag NWs, v) poly (3,4-ethylene dioxythiophene) polystyrene sulfonate (PEDOT: PSS), vi) SWNTs, and vii) graphene). Reproduced with permission.[295] Copyright 2016, Nature. e_1) The self-assembled monolayer MXene film onto a PET substrate of 6 × 6 cm^2 with 80% optical transmittance at 550 nm and an inset SEM image of assembled MXene NPs over a large area (scale bar 2 µm). Reproduced with permission.[120] Copyright 2019, American Chemical Society.

The pattern quantum pixel arrays displayed a wide resolution range with the highest resolution of 368 PPD (pixel per degree) with ≈100% yield (Figure 12a$_3$). The monochromatic green quantum dot LED device recorded a maximum current efficiency of 14.8 cd A^{-1} and a maximum external quantum efficiency of 3.3% (Figure 12a$_4$).

For emerging optoelectronic applications, there is a need to make high-resolution structures (<10 µm) with tightly packed 3D NPs architectures.[401] For example, C.A. Mirkin et al. first prepared the DNA-functionalized Au NPs of different shapes and sizes. Next, he assembled these NPs within PMMA templates in the LbL manner by forming the sticky-end DNA to complement the previous NPs layers.[30] The sphere-disk-cube NP architecture was fabricated, as shown in Figure 12b$_1$. Namely, the 60 nm spheres were placed on the 76 nm-edge-length cubes on top of the 105 nm-diameter and 7.5 nm-thick circular disks, arranged into the array of 200 nm spacing on 100 nm thick gold substrates. The NP architecture was coated with a thin layer of a solvent of 0–80% EtOH in H_2O to decrease the solvent polarity and average gap distance (Figure 12b$_2$). As a result, the absorption spectra of the 3D NP architecture were measured as a function of different EtOH-to-water ratios, and 75% of the increase in the average absorption spectra of the light from 550–800 nm was reported (Figure 12b$_3$).[401] The reversibility of optical properties for small and large gaps NP structure showed no deviation in the absorption spectra (Figure 12b$_4$).

The chemisorption phenomenon was utilized for manufacturing flexible transparent conductive electrodes (TCE) for printing high-resolution conductive patterns. For example, Busnaina et al. fabricated the Ag grid TCE by simple solution assembly (i.e., dip coating). The Ag line width could be as fine as 2 µm to 300 nm on a PET substrate tuned with altered wettability (i.e., hydrophobic-hydrophilic) (Figure 12c$_1$).[402] The optoelectronic properties of the TCE were characterized depending on the withdrawal speed (i.e., 0.25, 0.5, 0.75, and 1 mm min^{-1}) and thickness (i.e., 0.6 and 1.3 µm) of pattern grids. The device displayed an average transmittance of ≈93% in the visible light range (450–750 nm) with a sheet resistance of 0.8 Ω/sq (for the sample with 1.3 µm thick from a dipping withdrawing speed of 0.25 mm min^{-1}), which is suitable for most optoelectronics applications, as shown in Figure 12c$_2$-c$_3$.

Similarly, T. Hasegawa et al. manufactured a capacitive type of touch-screen sensor by surface photo-activated nanometal printing Figure 12d$_1$.[295] This technique enabled the production of Ag NPs conductive patterns of different line widths (i.e., 5, 3, and 0.8 µm) with the highest resolution of 0.8 µm (Figure 12d$_2$). TCE for touch sensor applications can be manufactured with narrow conductive metal wires, thus sensor contained lines with a width of 2 µm Ag NPs were patterned on the 18 cm-wide PET substrate. The performance (i.e., sheet resistance and transmittances) of TCE based on patterned Ag NPs was measured for different line widths, as shown in Figure 12d$_2$. The printed composites showed superior transmittance without sacrificing the sheet resistance compared to copper nanowires, silver nanowires, poly (3,4-ethylene dioxythiophene) polystyrene sulfonate (PEDOT: PSS), carbon nanotubes, or graphene materials. On the other hand, solution-based fabrication techniques, including spin and dip coating, have massive capability to produce highly conductive thin film coatings on a flat and large-area substrate. For instance, C. W. Ahn et al. assembled MXene NPs into a 10 nm-thick thin film with an optical transmittance of 80% at 550 nm, as shown in Figure 12e$_1$.[120] The interfacial assembly technique demonstrated the highly efficient material utilization from the large area assembled microstructure of MXene NPs on the target substrate with 0.1 mg mL^{-1} MXene concentration (Figure 12e$_1$ as an SEM image). Many other studies have also displayed the patterning of metallic NPs, single-walled nanotubes (SWNTs), graphene indium tin oxide (ITO), and MXene into flexible, large-area, and arbitrary-shape structures with unique functionality to produce TCE.[403–405]

4.3. Plasmonic Devices

Nanopatterning is critical for developing nanostructures for plasmonic applications. The colloidal noble metal nanoparticles are studied extensively for engineering plasmonic devices with control over the crystallographic structure and plasmonic properties.[406,407] When plasmonic NPs are organized into one, two, and three-dimensional periodic patterns, they generate the lattice plasmonic resonances as a function of the particle composition, lattice parameter, and substrate refractive index.[408] Recently, the combination of soft lithography and self-assembly approach was studied to fabricate large-scale, micro-nano structures with periodic arrangements. For example, J. Brugger et al. designed the 110 nm × 40 nm × 40 nm Au nanorod dimers separated by less than 2 nm gaps facilitated by the capillary-assisted assembly for the fabrication of plasmonic structures.[143] The plasmonic dimers' optical performance in resonance wavelength, near field intensity, and mode volumes was programmable by varying the interparticle distance (1-38 nm) (**Figure 13**a$_1$). The plasmonic response of dimer nanoantenna assembled onto a thin silicon nitride membrane was studied. The electron energy-loss spectroscopy (EELS) confirmed the coupling of the plasmonic modes in dimers, and energy mode splitting evolved from 0.11 eV (38 nm gap) to 0.5 eV (1 nm gap) (Figure 13a$_2$-13a$_3$). The EELS maps in Figure 13a$_4$-a$_5$ showed the plasmonic modes observed at the edge and center of the dimers. The simulation results also confirmed the coupling of plasmonic modes in dimer nanoantenna and energy splitting from 0.11 eV (38 nm gap) to 0.5 eV (1 nm gap) in a robust coupling regime (Figure 13a$_4$-a$_5$).

Colloidal chemistry and self-assembly have been studied for micro/nanoscale patterning of plasmonic NPs into monolayer films. For example, P.S Weiss demonstrated the patterning of plasmonic NPs into micro-nanoscale patterns of different morphologies, including islands, lines, and chiral structures by nanoparticle-chemical lift-off lithography .[57] The NP-CLL technique demonstrated the ability to pattern 50–100 nm-sized gold NPs into corners and turns (e.g., square spirals in Figure 13b$_1$) and achieved chiral activity in the visible and near-infrared (NIR) range. For example, the NIR of extinction spectra of square spiral-shaped samples was recorded with linearly and left and right circularly polarized light (Figure 13b$_2$). The circular dichroism (CD) represented the difference between the two extinction spectra and displayed the mirror activity for the clockwise (red) and counterclockwise (blue) square spirals (Figure 13b$_3$). They observed with a reduction in the size of patterned NP features to the sub-

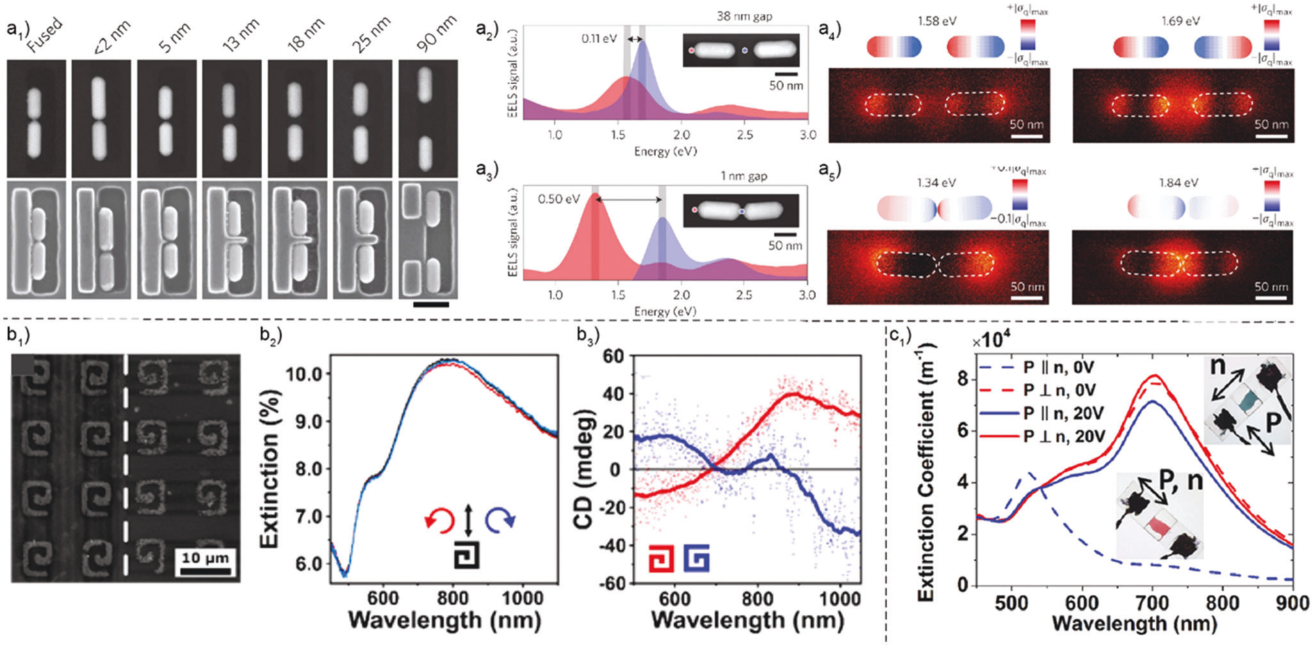

Figure 13. a_1) The SEM and in-lens image of Au nanorod (NR) dimers assembled within the adjacent traps separated by different interparticle gaps (scale bar 500 nm). a_2-a_3) The plasmonic mode coupling in NR dimers measured from scanning transmission electron microscopy electron energy-loss spectroscopy (STEM-EELS). The energy splitting was observed from a_2) 0.11 eV in weakly coupled systems at a 38 nm gap to a_3) strong coupling regime 0.5 eV at a 1 nm gap, and a_4-a_5) EELS maps and simulation results of charge distribution at the bonding and antibonding modes confirmed the near field tuning ($|\sigma_q|_{max}$ is maximum charge density). Reproduced with permission.[143] Copyright 2017, Nature. b_1) The SEM image of clockwise and counterclockwise spirals confirms the closely packed NP assembly into continuous structures, b_2) extinction spectra after illuminating a clockwise spiral with left circularity (red), right circularity (blue), and linearly (black) polarized light, and b_3) circular dichroism (CD) of clockwise (red) and counterclockwise (blue) spirals and their differences between micropatterns of two different spiral directions. Reproduced with permission.[57] Copyright 2021, American Chemical Society. c_1) The extinction coefficient spectra of 3.1 pmol mL^{-1} concentrated dispersion of Au NRs in 5CB measured with linearly polarized incident light for different polarization directions concerning director, with and without applied voltage. The inset images show the color change of the cell with a director (n) rotated with respect to the polarization direction (P). Reproduced with permission.[409] Copyright 2015, American Chemical Society.

micron scale, the optical activity (small signal-to-noise ratio and CD signal) could be enhanced to apply for a different range of applications.

Liquid crystals (LCs) have emerged as tunable bulk templates for ordering and alignment of different NPs for applications ranging from high-resolution television displays to telecommunications and sensing purposes.[409–411] In another example, I. I. Smalyukh et al. reported the anisotropic fluid (i.e., thermotropic LC) as bulk templates for assembling and organizing the metallic Au nanorods/platelets. The NPs were surface functionalized with N, N-dimethyl-N-octadecyl-3-aminopropyltrimethoxysilyl chloride to ensure the anisotropic surface interaction between the LC and NPs to generate spontaneous orientational preferences. The dispersion of gold NRs and 5CB LC (i.e., 4-Cyano-4'-pentylbiphenyl, with the chemical formula of C18H19N) exhibited orientational orders along the perpendicular direction of uniformly aligned LC. The surface polarization resonance (SPR) spectra for a high concentration larger than 3 pmol mL^{-1} for 20 × 50 nm Au NRs in 5CB showed merging in the longitudinal and transverse SPR peaks (Figure 13c_1). Additionally, compared to pure 5CB and low-concentration NRs, the high-concentration NRs provided a significant difference in the switching behavior exhibited in transmitted light when there was a rotation of the polarization of incident light and electrical switching (Figure 13c_1). The assembled NR dispersion displayed several SPR modes switchable by a field as promising candidates for plasmonic polarizers and color filters.

4.4. Anticounterfeiting Sensors and Detectors

Anti-counterfeiting technologies are added to products or their packaging to allow consumers or inspectors to check whether a product is authentic. For example, Y. Song et al. designed 3D micro colloidal structures with micro/macro hierarchical structural color patterns by asymmetric dewetting of 0D CdTe NPs ink.[290] By leveraging the adjustable morphologies obtained by asymmetric dewetting of the droplets and photonic properties of 3D microcolloidal crystals, macro/microhierarchical structures with distinctive color patterns were designed (**Figure 14**a_1). The composition, location, and morphology of single 3D structures and their combinations display reflective rainbow color patterns, offering potential application in the fabrication of multi-information carrier or anticounterfeiting materials (Figure 14a_2-a_4). 3D printing technologies demonstrated their potential for microscale patterning NPs in 3D architectures with the multi-functionalities required for various applications.

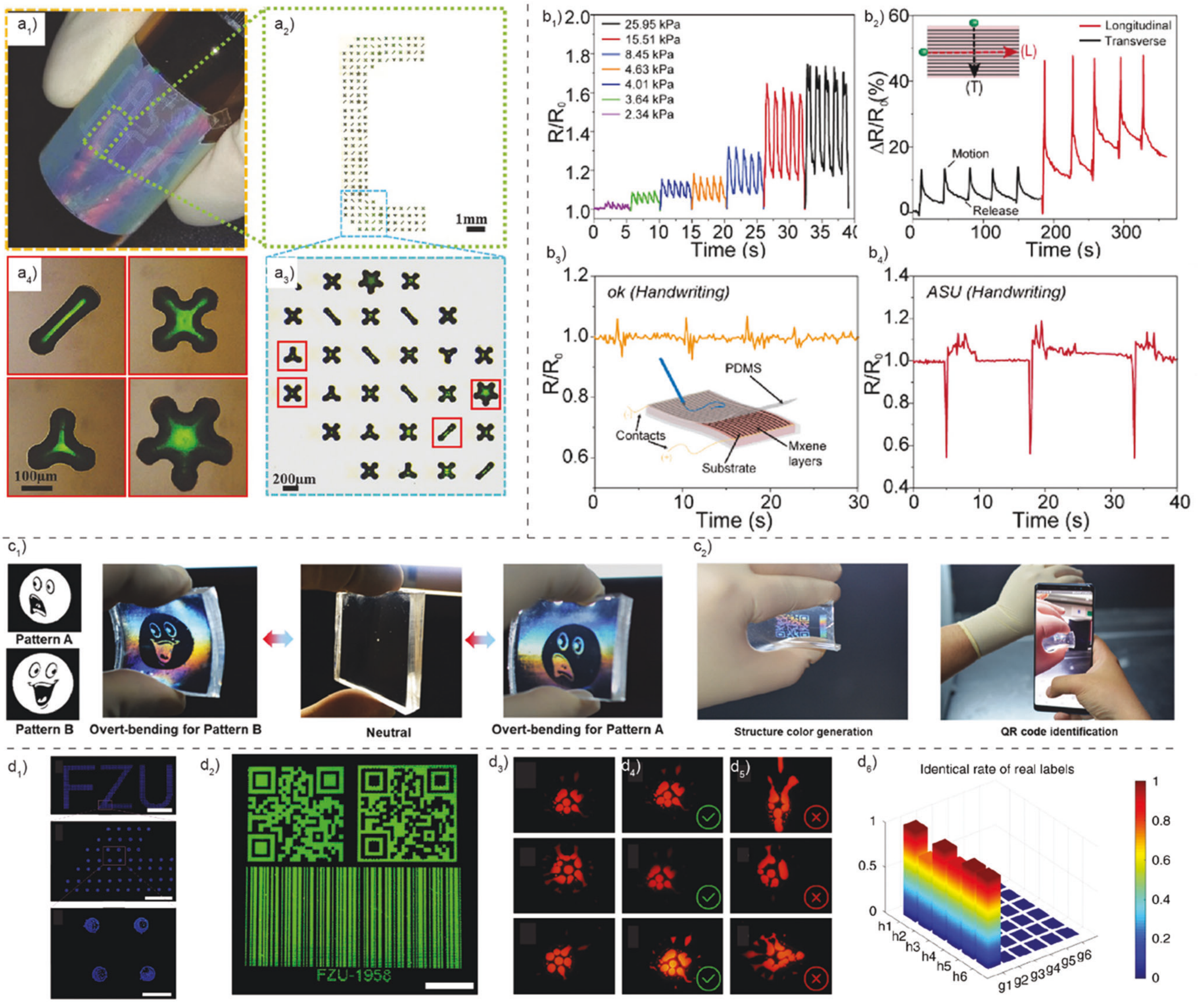

Figure 14. a$_1$) Microscale pattern of 0D microcolloidal crystals in 3D morphology formed by manipulation of TCL for the word "ICCAS" (i.e., Institute of Chemistry, Chinese Academy of Sciences) consisting of single units as a pinning pattern, a$_2$) a zoom-in optical image of the letter "C" from ICCAS, a$_3$) an enlarged optical image of 3D patterns deposited in letter "C", and a$_4$) optical image of information carrier dots of different 3D morphology including line, quadrilateral, triangle, hexagonal. Reproduced with permission.[290] Copyright 2015, Wiley-VCH. b) A sensor with nanoparticle (i.e., MXene) gratings fabricated by microfluidic deposition of the MXene ink onto 3D printed templates showed high sensitivity and selectivity, including b$_1$) the sensing response under pressure for different loading and unloading cycles from 2.34 to 25.95 kPa, b$_2$) the sensitivity to anisotropic motions in the longitudinal and transverse directions (i.e., along and perpendicular to the MXene aligned direction, respectively), and b$_3$-b$_4$) sensing to the handwriting of "ok" and "ASU" generated on the micropatterned surfaces. Reproduced with permission.[62] Copyright 2021, American Chemical Society. c$_1$) Two different patterns printed on either side of the composite substrates (i.e., containing PDMS-encapsulated SiO_2 NPs within patterns) display two different optical images under inward and outward bending, and c$_2$) a QR code printed on the PDMS and the decoding process with the mobile phone auto-detection for anticounterfeiting applications. Reproduced with permission.[412] Copyright 2020, Wiley-VCH. d$_1$) The fluorescence image of the "FCU" letter composed of a blue emission dot pattern (scale bar 4000 μm) with a locally enlarged image (scale bar is 500 μm) and a further enlarged image (scale bar 100 μm) in zoomed-in regions, d$_2$) a fluorescence image of green image of 2D QR and barcodes consisting of thousands of dot patterns (scale bar is 1 cm), d$_3$) three different single dot-composed patterning codes as security labels with d$_4$) their fluorescence images taken with different brightness, sharpness, rotation angle, magnification, and their combination conditions and d$_5$) fluorescence images of security labels not in a database were not identifiable, and d$_6$) recognition rates of labels by deep learning decoding mechanism (i.e., the axis legends with g_1-g_6 and h_1-h_6 corresponding to the label in d$_3$ and d$_4$, respectively). The blue-to-red transition in the color scale ranges from 0 to 100%, matching the score of captured images from the labels. Reproduced with permission.[179] Copyright 2019, Springer Nature.

Counterfeit products can be fakes or unauthorized replicas of genuine products, often produced to take advantage of the superior value of the imitated product, including documents and electronics. As another example of detecting signature authenticity, S. Jambhulkar et al. designed the surface patterning structures containing unidirectionally aligned 2D MXene via a hybrid 3D printing (i.e., DIW and μCLIP) approach (Figure 6a). An immediate result of the fabricated micropatterns was the directional electrical or resistive properties for sensing purposes.[62] The patterned MXene film demonstrated high sensitivity to mechanical stress (i.e., 2.34-25.95 kPa pressure and 1–50% flexural strain) due to aligned MXene morphology and the varying sensitivity towards the deformation (Figure 14b_1). The patterned films also demonstrated anisotropic sensitivity when an object is moved with constant pressure (10 N) on the surface, e.g., in the MXene alignment direction (i.e., longitudinal) or perpendicular (i.e., perpendicular) direction (Figure 14b_2). The writing characteristic on the patterned MXene film may respond to a different pressure, speed, and sequence and generate unique and complex responses (e.g., ok and ASU), which showed potential for anticounterfeiting applications (Figure 14b_3-b_4).

Initially invented based on Morse codes, bar codes have been popular methods of representing data in a visual, machine-readable form by varying the widths, spacings, and sizes of parallel lines. As one demonstration, Zhou et al. self-assembled the SiO_2 NP structure on the planar substrate using a piezoelectric drop-on-demand inkjet printer, followed by encapsulation in soft PDMS substrates.[412] They investigated the multidimensional structural coloration mechanism depending on similar optical properties and differential mechanical behavior of soft PDMS and rigid SiO_2 NPs. For example, at the neural condition, SiO_2/PDMS composite was transparent, which changed to distinct color patterns under mechanical stress (Figure 14c_1), demonstrating the structurally switchable system with covert-overt properties. They also demonstrated the application of a structurally switchable color platform for anti-forgery systems, e.g., QR codes (Figure 14c_2). These well-defined structures containing 2D and 3D hierarchical features resulted in unique collective functional properties, implying anticounterfeit applications in a simple, convenient, and mass-producible manner.

Anticounterfeiting techniques are required to be inexpensive, mass-producible, non-destructive unclonable, and convenient for authentication. Conventional security labels with microscopic features like QR codes and bar codes can be conveniently authenticated with the naked eye but are easier to counterfeit. To address this L. Qian et al. developed unclonable security labels of II-VI semiconductor core-shell quantum dots by combining the advantages of inkjet printing, portable smartphone microscope, and artificial intelligence (AI) techniques.[179] Firstly, the print substrate surface was modified by coating PMMA nanoparticles which acted as stochastic pinning points for three-phase contact lines of ink droplets.[179] Later, with the evaporation of the solvent, QDs were deposited around the pinning points forming physically unclonable flower-like dot patterns as shown in Figure 14d_1. The coating of the continuous, smooth, poorly wettable PMMA layer had shrunk and slid the TCL of the droplet toward the center, brought QDs to the center of the droplet, and prevented the formation of a coffee ring pattern.[179] The full-color security labels were generated by utilizing red, green, and blue-emission semiconductor QDs (Figure 14d_2). The image of flower-like dot patterns at various magnifications, sharpness, brightness, rotations, and a combination of these parameters was captured for decoding security labels (Figure 14d_3-d_5). Then the images were fed into trained AI for validation and the authentication outputs are shown in Figure 14d_6 with the accuracy of h_n ($n = 1, 2, \cdots, 6$) of 0.999, 0.758, 0.999, 0.909, 0.999, and 0.999, respectively. This technique demonstrated a convenient, reliable AI-based authentication strategy for easy detection of security labels.

4.5. Magnetic Devices and Robotic Microstructures

The aligned microstructure of 1D magnetic NPs exhibits anisotropic magnetic properties because of dipolar interactions. Magnetic NPs have been increasingly interested in various applications, including sensors, actuators, microbots, biomedical imaging, and microelectronics, due to their unique magnetic characteristics derived from 1D, 2D, and 3D-assembled microstructures.[16,26,365] For example, the macroscopic magnetic metasurfaces were fabricated by aligning gold nanorods into linear structures using wrinkled templates and a convective self-assembly approach (**Figure 15**a). The NP assembly into individual lines was obtained by dip coating, where the unidirectional flow of colloids (2 mg mL^{-1}) facilitated the orientation of 1D NPs along the coating withdrawing axis, as shown in Figure 15a_1. Later, the aligned building blocks were transferred onto the hydrophilized gold film by wet contact. The complete transfer of NPs with the maintained orientation onto a 5 × 5 mm substrate area was obtained by additional effects of van der Waals interaction between the gold NPs/gold film and binding groups of protein shells. The anisotropic response of the assembled unit was calculated in the forward and backward direction by the S-parameter retrieval method. Based on the predictions, the system displayed the electric and magnetic resonance at a wavelength of 721 nm due to the strong electromagnetic coupling of the plasmonic particle to the metallic film (Figure 15a_2). This wrinkled template-based NP assembly showed the potential to fabricate a functional magnetic metasurface that possessed high sensitivity to electromagnetic coupling suitable for sensing applications.

Magnetic NPs have broad applications in medical diagnostics, magnetic immunoassay, catalyst support, wastewater treatment, cancer therapy, information storage, microfluidics, magnetic cooling, and biomedical imaging. For example, D. P. Arnold et al. reported the assembly of magnetic NPs (i.e., iron oxides and cobalt ferrite) via magnetically directed assembly from magnetically patterned substrates (Figure 15b). The particles were assembled from a colloidal suspension in the higher magnetic gradient region at the boundary of magnetic poles. The in-situ NP crosslinking generated free-floating complex magnetic microstructures. The micropatterns of different shapes and sizes (75 μm wide square and 150 μm wide crosses) with a boundary line dimension of ≈230 nm in height and ≈4 μm in width were fabricated by the ≈200 mT magnetic fields (Figure 15b_1). The assembly of iron oxide NPs into magnetic microstructures depended on the assembly time and the volume fraction of NPs. As a result, the assembled microstructures displayed magnetic actuation, e.g., retained their geometric shape under the response

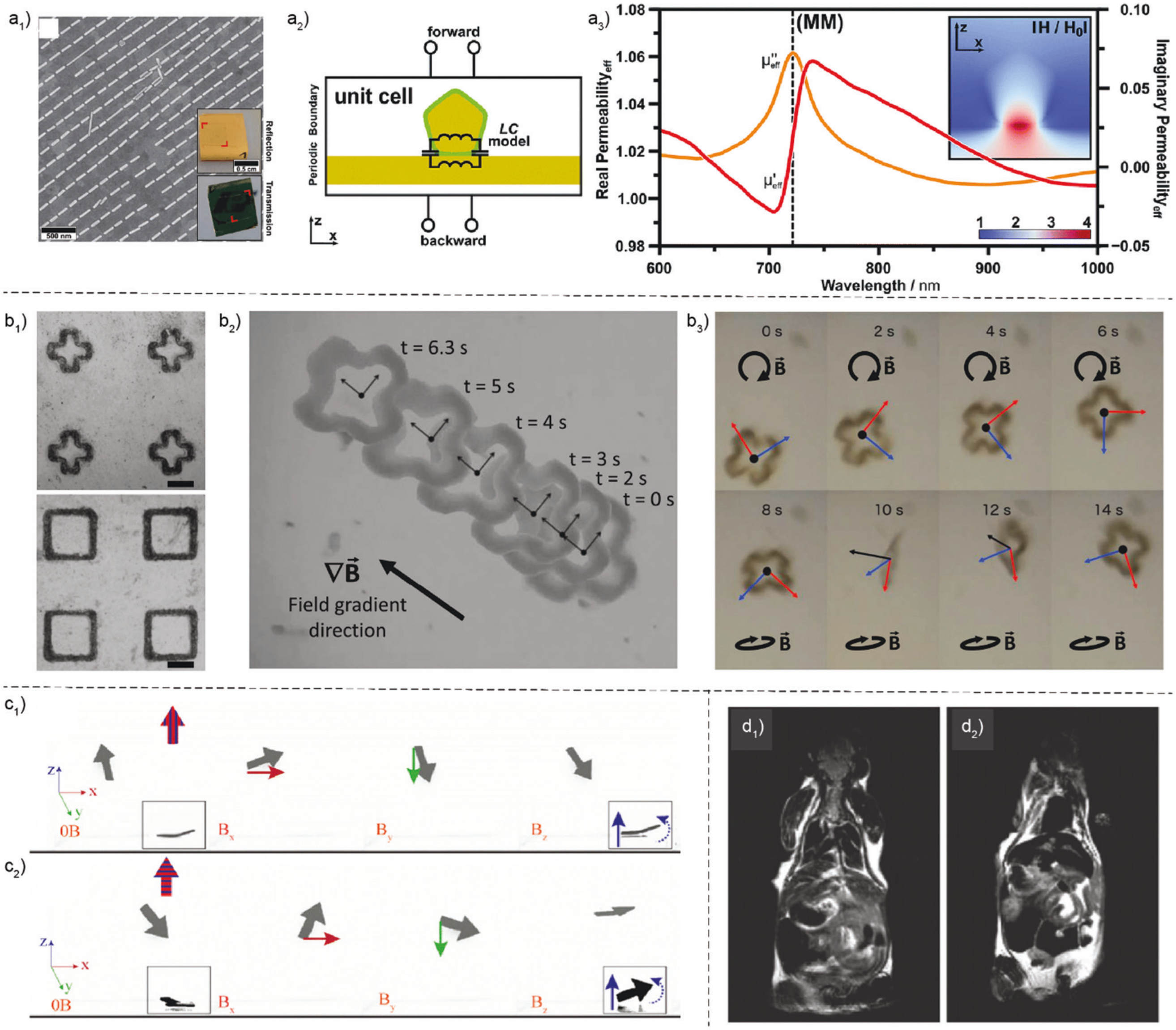

Figure 15. a$_1$) SEM image of Au NRs assembled onto a gold film substrate by template-assisted self-assembly process by dip coating the wrinkled templates (scale bar 500 nm) with the inset images of film photographs in reflection (top) and transmission (bottom) modes (scale bar 0.5 cm), a$_2$) schematic of the magnetic unit for S-parameter retrieval method with inductor and capacitor (LC) model, and a$_3$) the calculated magnetic permeability of the system (i.e., an Au film-coupled Au NRs) revealing the presence of magnetic resonance and magnetic field (inset). Reproduced with permission.[416] Copyright 2016, Royal Society of Chemistry. b$_1$) Magnetically assembled and crosslinked iron oxide NPs in microstructures of magnetic patterns from the cross (top) and square (bottom) shapes (scale bar 100 µm), b$_2$) superimposed image of the movement of a single iron oxide microstructure stimulated from a magnetic field generated by permanent magnets, and b$_3$) the rotation and flipping of iron oxide microstructure by rotating directions of applied magnetic fields. Reproduced with permission.[417] Copyright 2015, American Chemical Society. c) Magnetic actuation of 3D printed multilayer, arrow-shaped samples with stimuli-responsive behaviors to applied magnetic fields (i.e., directions represented in red, green, and blues arrows for the X, Y, and Z axis, respectively), with the printed layers c$_1$) parallel with or c$_2$) perpendicular to assembled Fe_3O_4 NPs in adjacent layers (inset images show the side view of the arrowhead). Reproduced with permission.[414] Copyright 2022, The Royal Society of Chemistry. d) The magnetic resonance image (MRI) of mouse liver tissue, d$_1$) before dosing with iron-oxide nanocrystals exhibiting normal grey contrast and d$_2$) after dosing indicating healthy liver tissue appearing black, a contrast due to the presence of assembled magnetic nanoparticles after 24 hrs. Reproduced with permission.[415] Copyright 2015, Wiley-VCH.

of the magnetic field. Furthermore, the structures showed displacement in the direction of a higher magnetic field gradient due to magnetic forces exerted on the magnetic NPs, as shown in Figure 15b$_2$. Additionally, when the direction of the applied magnetic field was changed, the microstructures displayed movement along different axes (rotation and flip) depending on the direction of magnetic field rotation (Figure 15b$_3$).

In addition to colloidal-based assembly, 3D printing enables the integration of stimuli-responsive nanomaterial into 3D objects and transforms them into 4D objects in response to environmental stimuli, suitable for various actuating and soft robotic systems.[413] For example, D. Ravichandran et al. have micropatterned 7.5 wt.% Fe_3O_4 NPs in the anisotropic fashion in multiphase, multilayer structures via Multiphase Direct Ink writing (MDIW) 3D printing.[414] This 3D printing is unique in a way that the magnetic particles and polymers used to confine the nanoparticles along a specific channel can be printed at the same time, with the iron oxide selectively distributed at specific locations. The particle orientation generated higher magnetization in the direction parallel to the NPs than perpendicular which generated anisotropic response to magnetism in a 3D space.[414] Figure 15c_1-c_2 shows the response of the arrowhead samples to the changing magnetic field (B) where the arrowhead of the sample is aligned to B (green, red, and blue arrow) when the magnetization direction is parallel to aligned NPs layers. When a magnetic force (F) was applied along with B, the sample displayed directional movements (i.e., translation and flipping motion) with precise directional control (e.g., moving ahead, backward, rotation in water, flipping in air), suggesting broad applications in wearable electronics, soft robotics, biomedical scaffolding for drug delivery, and many more.[414] In another example, R. K. Prud'homme et al. reported the assembly of 10 nm iron-oxide nanocrystals encapsulated into poly(ethylene glycol) (PEG) to make biocompatible contrast agents.[415] They could detect the 0.8 mm^3 metastatic tumor from non-small cell lung cancer in vivo in mice liver via magnetic resonance image (MRI).[415] The in vivo imaging demonstrated the ability of assembled iron-oxide nanoparticles to act as MRI and fluoresce imaging contrast agents (Figure 15d_1-d_2).

4.6. Biological and Biomedical Systems

Nanoparticle-based biosensors have been widely studied in biomolecule sensing applications, including bioreceptors for cells and tissues, biotransducers, and biodetectors for glucose, food, or cancer cells.[18,418] Some studies have focused on noble metal NPs (e.g., Au and Ag) because of superior biocompatibility, high surface energy, and robust signal amplification.[419–421] Also, the microfluidic integration of metallic NPs is suitable for biosensing applications because target analytes can be directly mixed with NPs and deposited into microchannels for SERS-based detection of biomolecules. For example, X. J. Zhang et al. developed a device by patterning Ag NPs into microfluidic devices. During the particle patterning, the solution containing target molecules of different concentrations (e.g., single-stranded DNA (1 mM -1 nM) and rhodamine B (100 μM-1 pM)) flowed into a spiral-shaped microfluidic device (**Figure 16**a_1).[219] The Raman signals were measured to calculate the SERS enhancement factor (EF). The EF values turned out to be $\approx 1.5 \times 10^8$ for DNA molecules and $\approx 4.3 \times 10^{11}$ for rhodamine B (Figure 16a_2-a_3), showing significant intensifications for picometer-level concentrations of molecules.[219]

During the pandemic, nanoparticle assembly for sensing COVID-19 antibodies has been in great demand. For example, R. Panat et al. created a sensing platform by aerosol jet 3D printing of Au NPs into 3D electrodes, followed by the assembly of rGO nanoflakes on the Au micropillars via simple drop-casting. (Figure 16b_1-b_2).[422] The 3D-printed electrode with functionalized rGO (-COOH) and viral antigens (-NH_2) was integrated into the electrochemical cell (EC) for the detection of antibodies introduced in EC by a microfluidic approach. The amidation reaction between rGO and antigen immobilized the antigen to detect antibodies by electrochemical transduction.[422] The antibodies were selectively attached to the antigen surface, generating an immunocomplex on the 3D electrode surface by antigen/antibody interactions. When the fluid with SARS-COV-2 spike S1 antigen at different molar concentrations (0.01×10^{-15}–30×10^{-9} M) was introduced in the EC, the impedimetric sensing plots of electrodes were measured (Figure 16b_3). The increase in the concentration of antibodies showed an increase in circuit impedance signal (i.e., R_{ct} charge transfer resistance) due to the fact that the binding of antibodies to antigen would obstruct the electron transfer from the electrolyte to the electrode surface (Figure 16b_4). This method showed potential for the detection of biomarkers for other infectious diseases, such as Ebola, HIV, and Zika.

The detection of sub-ppm level concentrations of volatile organic compounds (VOCs) in exhaled breath is critical for the on-time detection of illness. The most abundant VOCs in human breath are acetone, methanol, ethanol, ammonia, and their compounds are considered biomarkers of various diseases and disorders.[215,423] Therefore, S. Jambhulkar et al. demonstrated the sensing capabilities of highly dense and preferentially aligned CNF NPs (1 mg mL^{-1}) patterned on the 3D printed substrate to low concentrations of VOCs in liquid and gas form.[209,215] The CNF sensor possessed high sensitivity, a low theoretical limit of detection (sub-ppm), fast response (<30 s) and recovery (<10 min), and a wide sensing range (tens to hundreds of ppm) at RT (Figure 16c_1). The enhanced sensing performance is attributed to the fast electron transport along the CNF alignment direction and trapping of VOC molecules on 3D-printed micropattern substrates. In addition to chemical sensors, micro force sensor microelectronics is necessary for wearable human healthcare monitoring, intelligent robotics, and human-machine interface. For example, W. Yang et al. fabricated the microchannels confined MXene piezoresistive senor, benefiting from the confinement of accordion-shaped MXene NPs within channel microstructures.[424] The sensor with microchannels of different depths (0–78 μm) showed that deeper channels facilitated larger deformation and generated a stable response to different pressures ranging from 0.05 to 3.5 kPa.[424] Additionally, the device displayed a low detection limit (9 Pa), high sensitivity (99.5 kPa^{-1}), and fast response time (4 ms) which helped in the detection of human micromotions like vocal cord vibrations and wrist pulse for healthcare monitoring (Figure 16d_1-d_3).

5. Challenges and Future Perspectives

5.1. Patterning Precision at Atomic or Molecular Scale

Nanoparticle and hybrid nanoparticle-molecular assembly at the nano or molecular scale present challenges and opportunities. First, achieving precise control over the assembly process at the nano or molecular scale is a significant challenge for nanomanufacturing. Controlling factors, such as size, shape, orientation, and interparticle distances, as well as the physical or chemical properties of templates to direct nanoparticle assembly, requires

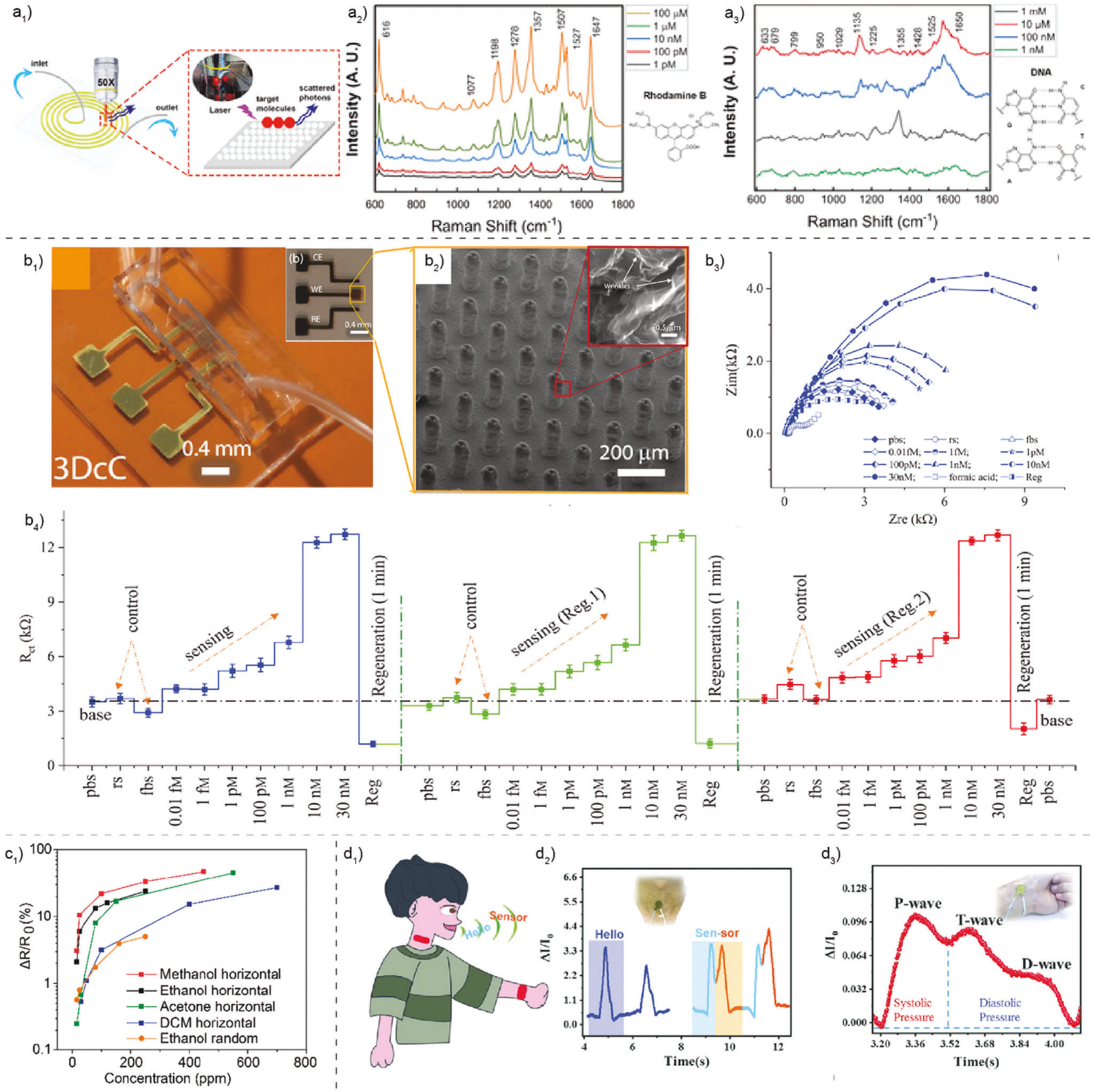

Figure 16. a$_1$) Setup of Raman measurement for detecting biomolecules by the spiral-shaped microfluidic system, with the Raman spectra of a$_2$) rhodamine B (RB) solutions at five concentrations and a$_2$) DNA solutions at four concentrations. Reproduced with permission.[219] Copyright 2021, American Chemical Society. b$_1$) An optical image of the 3D printed electrochemical cell device, b$_2$) an SEM image of 3D printed gold micropillar arrays (10 × 10) with an inset SEM image showing the morphology of a single gold micropillar coated with rGO flakes (zoomed-in image), b$_3$) the Nyquist plots of a 3D printed sensor were measured by the electrochemical impedance spectroscopy (EIS) method without and with the spike S1 antibodies at different concentrations of 0.01×10^{-15} M, 1×10^{-15} M, 1×10^{-12} M, 100×10^{-12} M, 1×10^{-9} M, 10×10^{-9} M, and 30×10^{-9} M in phosphate buffer saline (pbs) solution, and b$_4$) charge transfer resistance (R_{ct}) was calculated by fitting the Nyquist plot data to Randles equivalent circuits for each concentration of antibodies and control serum before and after each regeneration. Reproduced with permission.[422] Copyright 2021, Wiley-VCH. c$_1$) Sensing response of patterned CNF and randomly oriented film of 1 mg mL^{-1} towards various volatile organic compounds (VOC) molecules (i.e., methanol, ethanol, acetone, and dichloromethane) of different concentrations. Reproduced with permission.[209] Copyright 2020, American Chemical Society. d$_1$-d$_3$) A microchannel-confined MXene-based piezoresistive pressure sensor as a wearable device for physiological signal detections (e.g., human voice or wrist pulse). Reproduced with permission.[424] Copyright 2020, Wiley-VCH.

overcoming limitations imposed by Brownian motion, diffusion, and steric effects.[425–427] For example, achieving high-resolution features at sub-10 nm necessitates precise surface treatment procedures encompassing physical topologies and surface chemistry. To facilitate such high-resolution nanoparticle (NP) assembly on template surfaces, the utilization of prefabricated templates with NP dispersion or co-assembling polymer matrices proves beneficial. Additionally, these approaches rely on establishing long-range particle-substrate attractions that promote NP attachment to the substrate, accompanied by strong short-range attractions to immobilize the NPs at precise locations. However, these interactions are often interdependent, making the optimization of nanopatterning techniques a complex endeavor. Second, manipulating and controlling the interactions between nanoparticles or molecules and their surrounding environment (e.g., templates or confinement conditions) is challenging to control. Understanding and engineering interfacial interactions to achieve desired assembly outcomes, such as specific orientations, alignments, or surface functionalities, require careful consideration. External fields, such as electrical or magnetic, may facilitate the nanoparticle orders; however, considering the essence of fields, their influences over extremely small areas at the nanoscale or large regions at the macroscale are questionable when the short-distance forces are considered.[26,428]

These challenges present new opportunities for experimental and theoretical studies. First, continued advancements in characterization techniques, such as high-resolution microscopy, spectroscopy, and in situ monitoring, offer opportunities for better understanding and controlling nanoparticle or molecular assembly processes.[429–431] Improved characterization capabilities, especially when the environmental parameters are highly programmable, contribute to a deeper understanding of assembly mechanisms and aid in optimizing assembly outcomes no matter whether template effects are present or not. Second, simulation and modeling play a crucial role in understanding nanoparticle assembly mechanisms and procedures by providing valuable insights into the underlying processes at the atomic and molecular levels. For example, Simulation techniques, such as molecular dynamics (MD) and Monte Carlo (MC) simulations, allow researchers to visualize and predict the behavior of nanoparticles during assembly.[432,433] These simulations provide detailed information on particle trajectories, interparticle interactions, and assembly pathways not feasible to visualize in experiments, aiding in the understanding of how nanoparticles come together and form ordered structures. Simulation and modeling also provide a platform for optimizing assembly parameters, such as particle size, concentration, surface properties, and solvent conditions when external confinement prevents direct experimental observation. By systematically varying these parameters in simulations, researchers can identify the optimal conditions for achieving desired assembly structures and properties. This guides the experimental design and reduces the trial-and-error risks in the laboratory, especially considering the time-consuming tooling engineering for template manufacturing.

Last but not least, understanding the molecular-level assembly of nanostructures is crucial as it may not always reach a thermodynamic equilibrium state, with various metastable phases having lower energy than the stable state. Molecular intricacies, such as charge states at the NP/fluid/substrate interface, surface inhomogeneity, and functional properties, influence the assembly forces involving van der Waals, electrostatic, and dipole-dipole interactions.[197,434] Computational modeling methods, including Density Functional Theory (DFT)-based simulations, enable the investigation of thermodynamics and dynamics at the atomic scale.[435] Experimental techniques like X-ray scattering, TEM, and AFM complement these simulations.[436] Emerging techniques like machine learning, DFT calculations, and molecular dynamics provide valuable insights into interparticle force/torque parameters.[431,433,437] These approaches identify molecular details, interparticle forces, local response, and microstructural phases during the assembly process. Moreover, they facilitate the study of thermodynamic properties, system dynamics, and kinetics, shedding light on the mechanisms governing nanoparticle self-assembly. Simulation and modeling contribute significantly to the understanding of assembly processes by analyzing driving forces, energy barriers, and activation energies involved in nanoparticle assembly.

5.2. Patterning Scalability Across Multiscale

Scaling up nanoparticle assembly processes often introduces materials, equipment, and process control complexities. Maintaining the same level of precision and quality at a larger scale can be challenging because the nanoscale self-assembly may be spontaneous but the scalability requires longer-range orders. First, achieving uniformity and consistency in nanoparticle assembly across large areas or volumes involves many parameters. As the assembly process moves from the nano to the macroscale, the system's complexity involves handling more significant quantities of nanoparticles, managing interactions between a larger number of particles, and addressing challenges related to mass transport and fluid dynamics. Thus, the design of experiments may consider parameters, such as particle size, shape, surface properties, and their interactions with the external environment (e.g., temperature, pressure, and confinement from templates). Plus, as the assembly process is scaled up, the likelihood of defects increases, which will impact the overall quality and performance of the assembled structures. Issues such as particle aggregation, incomplete coverage, or non-uniform packing have become more prevalent. More importantly, scaling up nanoparticle assembly processes can be costly due to increased material consumption, equipment requirements, and process complexity.

Ensuring reproducibility and uniformity on a larger scale without compromising the assembly quality is essential for practical applications. First, scalable nanoparticle assembly techniques can be integrated into existing manufacturing processes, enabling the production of advanced composite materials, electronics, sensors, and other devices with enhanced performance.[426,438] For example, one potential approach for achieving large-area nanoparticle micropatterning is to combine suspension-based self-assembly with new nanofabrication techniques. This integration enables the creation of substrates with transient or transitional surface features that facilitate the assembly process. Various nanofabrication methods, including soft lithography, imprinting, e-beam lithography, dip pen lithography, electrochemical deposition, and nanolithography, can be employed to develop such substrates.[57,240,325,439–441] For example, patterns can be transferred onto substrates with controlled surface features via lithography (e.g., soft or e-beam lithography), enabling subsequent NP assembly in specific locations.[396,440] On the other hand, imprinting involves using a mold to create surface patterns by pressing it onto a substrate.[58] This technique allows for the replication of complex surface structures and can be employed to generate transient or transitional features that assist in NP assembly.

The rapid advancement of 3D printing technology has opened new possibilities for both bottom-up and top-down fabrication approaches in the creation of patterned templates that may benefit the scalability of nanoparticle assembly. This innovative technique provides a platform for manufacturing complex three-dimensional (3D) patterns, offering the potential to mimic the structural and mechanical properties of biological systems.[194,442,443] By combining 3D printing with external fields, it becomes feasible to fabricate intricate designs and control the directional orientation of nanoparticles (NPs) within the printed structures. Despite the numerous advantages of 3D printing, there are challenges associated with integrating NPs into the printing process. The interplay between the NPs and the printing parameters can affect the interface between the NPs and the printed material, potentially limiting the resolution of the patterns and the desired surface properties.[180,444] Overcoming these challenges requires careful optimization of the printing parameters, material selection, and surface treatments to ensure successful integration and achieve the desired pattern resolution and surface characteristics.

In addition to hybrid manufacturing techniques, the integration of robotics and machine learning holds significant potential for revolutionizing the efficiency of nanoparticle assembly.[15,431] The scalability of nanoparticle assembly processes can greatly benefit from advancements in automation and robotics technologies, offering several advantages, such as increased precision, consistency, and reduced reliance on human intervention. Robotic systems can be employed to perform repetitive and precise tasks involved in nanoparticle assembly, ensuring consistent and accurate placement of nanoparticles. These robotic systems can be equipped with advanced sensing capabilities to detect and adjust for variations in nanoparticle properties, ensuring high-quality assembly results. Then, machine learning algorithms can play a crucial role in optimizing the in-situ collected data. Through the analysis of vast amounts of data, machine learning models can identify patterns, optimize assembly parameters, and enhance the overall efficiency of the assembly process. These algorithms can learn from previous assembly experiences and adapt to changing conditions, enabling continuous improvement and optimization of assembly operations.

5.3. Complex 3D Micro- or Macro-patterning

Creating complex 3D micropatterns requires intricate design considerations and precise fabrication techniques. The complexity of the desired structures can pose challenges in terms of design optimization, process scalability, and fabrication repeatability, as discussed in Sections 5.1 and 5.2. Achieving uniform and consistent assembly throughout the complex 3D structure can be challenging. Factors, such as diffusion, flow dynamics, and external forces, must be carefully controlled to ensure uniform particle distribution and desired 3D assembly outcomes. For example, integrating nanoparticles with different sizes, shapes, and functionalities into complex 3D structures can include proper alignment, interconnectivity, and hierarchical organization, which is crucial for achieving desired functional properties.[139,445] Besides, contamination in basic elements can make complex 3D micropatterning susceptible to defects and impact the structural integrity and performance of the assembled structures.

Bioinspired assembly, as a quickly expanding research area, can offer significant benefits to the resolution and scalability during 3D nanoparticle assembly. By drawing inspiration from biological systems and processes, researchers can leverage nature's strategies to overcome challenges and achieve improved performance in 3D nanoparticle assembly. First, biological systems often exhibit hierarchical organization, with structures organized at multiple length scales.[446,447] By emulating this 3D hierarchical organization, nanoparticle assembly can achieve increased complexity and precision. Second, biological systems exhibit high levels of molecular recognition and specificity, allowing for precise interactions and assembly at the molecular level.[448,449] Researchers can achieve selective and controlled assembly in 3D space by incorporating similar recognition mechanisms into nanoparticle assembly, resulting in improved resolution and scalability. More importantly, biomimicry involves designing templates and surfaces that mimic natural structures or functionalities. These biomimetic structures can provide guidance and direction to nanoparticles, facilitating their 3D assembly into desired patterns and structures. Last but not least, biological systems often exhibit dynamic adaptation and response to environmental stimuli.[450–452] Dynamic assembly processes can respond to changes in external conditions as active matter, allowing for real-time adjustments and optimization during assembly.

Advanced manufacturing techniques, such as 3D printing, glancing angle deposition (GLAD), PVD, and imprinting lithography (IL), play a crucial role in facilitating the goal of 3D nanoparticle assembly. 3D printing, as mentioned in Section 5.2, offers the ability to create intricate 3D structures by sequentially depositing printing materials layer by layer. By combining 3D printing with external fields, such as magnetic or electric fields, precise control over the directional orientation of nanoparticles (NPs) can be achieved. In addition to 3D printing, advanced techniques like GLAD, PVD, and IL are being explored for the fabrication of 2D nanopatterns that can be stacked to create 3D microstructures over large areas.[59,453–455]

Chemistry plays a crucial role in 3D nanoparticle assembly by providing methods for surface functionalization, interfacial manipulation, and controlling the behavior of nanoparticles. First, surface functionalization enables the modification of nanoparticle surfaces with functional groups, ligands, or polymers (e.g., Janus, core-shell, and patchy NPs).[456–458] These surface modifications can control nanoparticle interactions and the surrounding environment, influencing their 3D assembly behavior. On top of that, interfacial manipulation allows for the creation of patterned templates with asymmetric chemical structures or wettability. By controlling the surface chemistry and free energy of the templates, specific interactions with nanoparticles can be induced, guiding their 3D assembly into desired patterns.[36,39,459] Chemistry-based coating techniques, such as droplet casting, dip coating, or spin coating, can be used to disperse nanoparticles onto patterned surfaces with a 3D layer additive protocol. Besides, by adjusting the solvent composition, pH, or concentration in colloids, the behavior of nanoparticles, such as their aggregation, dispersion, or nucleation, can be controlled during the nucleation and crystallization procedures. Last but not least, ligand exchange reactions and crosslinking processes can stabilize nanoparticle assemblies in 3D space, without which most particles will collapse without additional interparticle bonding. The 3D assembled structures can be strengthened or modified by introducing chemical reactions between nanoparticles or their ligands, enhancing their stability and functionality.

5.4. Multi-Materials to Enable Patterning Versatility

Multi-material nanoparticle assembly can enable patterning versatility and system multifunctionality but face a few challenges. First, integrating multiple materials in nanoparticle assembly requires careful consideration of their compatibility in terms of chemical interactions, solubility, and stability. Ensuring uniformity and desired ratios of materials throughout the assembly process requires precise control over the composition and distribution of different materials within the assembled structures. Managing the interfacial interactions between different materials is even more difficult than in the same-composition nanoparticles, as discussed in Section 5.3. Plus, scaling up multi-material nanoparticle assembly to larger areas while maintaining patterning versatility will mandate consistent and high-quality assembly across a large surface area (e.g., Section 5.2).

The primary methods for multilateral assembly involve patterning multi-material structures with well-controlled morphology for creating multifunctional devices. Conventional fabrication methods like nanoimprinting lithography,[460] nano transfer printing,[440] and microcontact printing[318] enable the transfer of NP patterns onto substrates, allowing for scalable and precise control of NP positioning and stability. Combining self-assembly and NP transfer processes offers opportunities to generate 2D and 3D multi-material structures with tailored properties for various applications. However, the processing speeds may be too low to achieve acceptable scalability and mass production. Many other rapid prototyping techniques, such as stamping, wrinkling, μCLIP, inkjet printing, FDM, and SLA 3D printing, have shown the ability to integrate multi-material systems and pattern different nanoparticles into 2D surface patterns or 3D complex structures.[62,65,204,439,461,209] Challenges still exist, including assembling isotropic and anisotropic building blocks, understanding underlying assembly mechanisms, and developing superstructure phase diagrams.

Nanoparticle assembly is crucial in various application areas, including polymer composites,[444] thermal management,[462] microelectronics,[102] optical devices,[463] biomedical devices,[464] magnetic systems,[465] and biological sensing/detection.[466] Take the block copolymer-nanoparticle composite as an example; the distinct morphologies exhibited by block copolymers, such as layered structures, gyroid structures, or hexagonally packed cylinders, offer confinement and organization sites for nanoparticles.[323] By utilizing selective surface modification or removing one block of the copolymer, nanoparticles can be precisely positioned and patterned within the copolymer matrix, resulting in well-defined nanostructures with controlled nanoparticle distributions. In addition to improved mechanical properties, the assembly of nanoparticles within polymers can improve electrical conductivity and thermal properties, leading to applications in conductive composites and thermal interface materials useful in heat sinks, electronic packaging, interconnects, electrodes, sensors, and data storage.[467–470] Additional applications to those mentioned in Section 4 include energy storage and conversion technologies (e.g., electrodes and electrolytes for batteries, fuel cells, and supercapacitors), catalytic structures with enhanced activity and selectivity, biosystems (e.g., drug delivery systems, imaging agents, tissue engineering scaffolds, and biosensors) and environmental sustainability (water purification, air filtration, pollutant sensing).

6. Conclusions

In conclusion, this comprehensive review has highlighted the significance of template-assisted nanoparticle assembly after a brief overview of template-less methods for NP self-assembly. The discussed methods, including capillary-induced, 3D printing-based, microfluidic-driven, chemically modified, mechanically wrinkled, and physically controlled approaches, enable the precise arrangement of nanoparticles into various morphologies on different surfaces. These deposition-based assembly methods have found applications in fields such as microelectronics, optoelectronics, plasmonics, anticounterfeiting, magnetic/robotic microstructures, and biological/biomedical systems. However, to fully harness the advantages of organized nanoparticles, it is crucial to address challenges related to high resolution, scalability, 3D complexity, new materials, and multi-material capability in micropatterning. Future research efforts should focus on advancing micro and nanomanufacturing techniques to unlock the potential of template-assisted nanoparticle assembly and pave the way for the development of next-generation devices and products with tailored structures and architectures.

Acknowledgements

The authors thank the support from NSF EAGER (award # 1902172), NSF CAREER (award # 2145895), NSF GFRP (#1000343766), ONR NEPTUNE (award # N00014-22-1-2105), AFOSR (award # FA9550-22-1-0263), BSF (award # 2020102), Arizona Biomedical Research Centre (award # RFGA2022-010-07), and ACS PRF (award # 62371-ND10).

Conflict of Interest

The authors declare no conflict of interest.

Keywords

directed assembly, micropatterning, nanoparticles, self-assembly, templates

Received: July 27, 2023
Revised: September 2, 2023
Published online: September 29, 2023

[1] N. Baig, I. Kammakakam, W. Falath, *Mater. Adv.* **2021**, *2*, 1821.

[2] in *Functional Properties of Nanostructured Materials* (Eds: R. Kassing, P. Petkov, W. Kulisch, C. Popov), Springer, Netherlands, Dordrecht **2006**.

[3] K. Shin, Y. Song, Y. Goh, K. Lee, *Iran J. Med. Sci.* **2019**, *20*, 1424.

[4] P. Wang, C. Jia, Y. Huang, X. Duan, *Matter* **2021**, *4*, 552.

[5] Z. Tang, N. A. Kotov, *Adv. Mater.* **2005**, *17*, 951.

[6] Z.-M. Dang, M.-S. Zheng, J.-W. Zha, *Small* **2016**, *12*, 1688.

[7] H. Bark, M. W. M. Tan, G. Thangavel, P. S. Lee, *Adv. Energy Mater.* **2021**, *11*, 2101387.

[8] S. Salimian, M. Montazer, A. S. Rashidi, N. Soleimani, A. Bashiri Rezaie, *J. Applied. Polymer Sci.* **2021**, *138*, 51357.

[9] R. Shenhar, T. B. Norsten, V. M. Rotello, *Adv. Mater.* **2005**, *17*, 657.

[10] D. Karnaushenko, T. Kang, V. K. Bandari, F. Zhu, O. G. Schmidt, *Adv. Mater.* **2020**, *32*, 1902994.

[11] M. Mayer, M. J. Schnepf, T. A. F. König, A. Fery, *Adv. Opt. Mater.* **2019**, *7*, 1800564.

[12] P. T. Probst, M. Mayer, V. Gupta, A. M. Steiner, Z. Zhou, G. K. Auernhammer, T. A. F. König, A. Fery, *Nat. Mater.* **2021**, *20*, 1024.

[13] M. P. Nikitin, T. A. Zdobnova, S. V. Lukash, O. A. Stremovskiy, S. M. Deyev, *Proc. Natl. Acad. Sci. U.S.A.* **2010**, *107*, 5827.

[14] I. U. Arachchige, S. L. Brock, *Acc. Chem. Res.* **2007**, *40*, 801.

[15] C. Mavroidis, A. Ferreira, C. Mavroidis, Eds., in *Nanorobotics: Current Approaches and Techniques*, Springer, New York **2013**.

[16] B. Wang, D. Liu, Y. Liao, Y. Huang, M. Ni, M. Wang, Z. Ma, Z. Wu, Y. Lu, *ACS Nano* **2022**, *16*, 20985.

[17] L. Zhang, F. Gu, J. Chan, A. Wang, R. Langer, O. Farokhzad, *Clin. Pharmacol. Ther.* **2008**, *83*, 761.

[18] S. Jiang, K. Y. Win, S. Liu, C. P. Teng, Y. Zheng, M.-Y. Han, *Nanoscale* **2013**, *5*, 3127.

[19] M. C. Roco, *Curr. Opin. Biotechnol.* **2003**, *14*, 337.

[20] M. Grzelczak, J. Vermant, E. M. Furst, L. M. Liz-Marzán, *ACS Nano* **2010**, *4*, 3591.

[21] K. Thorkelsson, P. Bai, T. Xu, *Nano Today* **2015**, *10*, 48.

[22] M. A. Boles, M. Engel, D. V. Talapin, *Chem. Rev.* **2016**, *116*, 11220.

[23] A. Sánchez-Iglesias, M. Grzelczak, T. Altantzis, B. Goris, J. Pérez-Juste, S. Bals, G. Van Tendeloo, S. H. Donaldson, B. F. Chmelka, J. N. Israelachvili, L. M. Liz-Marzán, *ACS Nano* **2012**, *6*, 11059.

[24] S. F. Tan, S. W. Chee, G. Lin, U. Mirsaidov, *Acc. Chem. Res.* **2017**, *50*, 1303.

[25] P. C. Millett, *J. Chem. Phys.* **2014**, *140*, 144903.

[26] D. Kokkinis, M. Schaffner, A. R. Studart, *Nat. Commun.* **2015**, *6*, 8643.

[27] B. Bharti, A.-L. Fameau, M. Rubinstein, O. D. Velev, *Nature Mater.* **2015**, *14*, 1104.

[28] K. Ariga, J. P. Hill, M. V. Lee, A. Vinu, R. Charvet, S. Acharya, *Sci. Technol. Adv. Mater.* **2008**, *9*, 014109.

[29] E. Auyeung, T. I. N. G. Li, A. J. Senesi, A. L. Schmucker, B. C. Pals, M. O. De La Cruz, C. A. Mirkin, *Nature* **2014**, *505*, 73.

[30] Q.-Y. Lin, J. A. Mason, Z. Li, W. Zhou, M. N. O'brien, K. A. Brown, M. R. Jones, S. Butun, B. Lee, V. P. Dravid, K. Aydin, C. A. Mirkin, *Science* **2018**, *359*, 669.

[31] B. Karagoz, L. Esser, H. T. Duong, J. S. Basuki, C. Boyer, T. P. Davis, *Polym. Chem.* **2014**, *5*, 350.

[32] Z. Jin, H. Fan, *Soft Matter.* **2014**, *10*, 9212.

[33] J. J. Martin, B. E. Fiore, R. M. Erb, *Nat. Commun.* **2015**, *6*, 8641.

[34] Y. Sahoo, M. Cheon, S. Wang, H. Luo, E. P. Furlani, P. N. Prasad, *J. Phys. Chem. B* **2004**, *108*, 3380.

[35] Y. Huang, W. Li, M. Qin, H. Zhou, X. Zhang, F. Li, Y. Song, *Small* **2017**, *13*, 1503339.

[36] P. Maury, M. Escalante, D. N. Reinhoudt, J. Huskens, *Adv. Mater.* **2005**, *17*, 2718.

[37] T. P. Bigioni, X.-M. Lin, T. T. Nguyen, E. I. Corwin, T. A. Witten, H. M. Jaeger, *Nature Mater.* **2006**, *5*, 265.

[38] A. Böker, J. He, T. Emrick, T. P. Russell, *Soft Matter.* **2007**, *3*, 1231.

[39] A. F. De Fazio, D. Misatziou, Y. R. Baker, O. L. Muskens, T. Brown, A. G. Kanaras, *Chem. Soc. Rev.* **2021**, *50*, 13410.

[40] Q. Song, Z. Xue, C. Liu, X. Qiao, L. Liu, C. Huang, K. Liu, X. Li, Z. Lu, T. Wang, *J. Am. Chem. Soc.* **2020**, *142*, 1857.

[41] Y. Lin, A. Böker, J. He, K. Sill, H. Xiang, C. Abetz, X. Li, J. Wang, T. Emrick, S. Long, Q. Wang, A. Balazs, T. P. Russell, *Nature* **2005**, *434*, 55.

[42] B. Gorain, H. Choudhury, M. Pandey, P. Kesharwani, M. M. Abeer, R. K. Tekade, Z. Hussain, *Biomed. Pharmacother.* **2018**, *104*, 496.

[43] R. Eivazzadeh-Keihan, A. Maleki, M. De La Guardia, M. S. Bani, K. K. Chenab, P. Pashazadeh-Panahi, B. Baradaran, A. Mokhtarzadeh, M. R. Hamblin, *J. Adv. Res.* **2019**, *18*, 185.

[44] M. S Onses, C. J. Thode, C.-C. Liu, S. Ji, P. L. Cook, F. J. Himpsel, P. F. Nealey, *Adv. Funct. Mater.* **2011**, *21*, 3074.

[45] A. S. Blum, C. M. Soto, C. D. Wilson, T. L. Brower, S. K. Pollack, T. L. Schull, A. Chatterji, T. Lin, J. E. Johnson, C. Amsinck, P. Franzon, R. Shashidhar, B. R. Ratna, *Small* **2005**, *1*, 702.

[46] A. Horn, S. Hiltl, A. Fery, A. Böker, *Small* **2010**, *6*, 2122.

[47] D. Wang, S. L. Capehart, S. Pal, M. Liu, L. Zhang, P. J Schuck, Y. Liu, H. Yan, M. B. Francis, J. J. De Yoreo, *ACS Nano* **2014**, *8*, 7896.

[48] K. R. Jinkins, S. M. Foradori, V. Saraswat, R. M. Jacobberger, J. H. Dwyer, P. Gopalan, A. Berson, M. S. Arnold, *Sci. Adv.* **2021**, *7*, eabh0640.

[49] L. Wang, A. M. Urbas, Q. Li, *Adv. Mater.* **2020**, *32*, 1801335.

[50] S. Julin, S. Nummelin, M. A. Kostiainen, V. Linko, *J. Nanopart. Res.* **2018**, *20*, 119.

[51] X. Fu, J. Cai, X. Zhang, W-D. Li, H. Ge, Y. Hu, *Adv. Drug Delivery Rev.* **2018**, *132*, 169.

[52] M. Drost, F. Tu, L. Berger, C. Preischl, W. Zhou, H. Gliemann, C. Wöll, H. Marbach, *ACS Nano* **2018**, *12*, 3825.

[53] D. Lebedev, G. Malyshev, I. Ryzhkov, A. Mozharov, K. Shugurov, V. Sharov, M. Panov, I. Tumkin, P. Afonicheva, A. Evstrapov, A. Bukatin, I. Mukhin, *Microfluid. Nanofluid.* **2021**, *25*, 51.

[54] H. Ding, Q. Zhang, H. Gu, X. Liu, L. Sun, M. Gu, Z. Gu, *Adv. Funct. Mater.* **2020**, *30*, 1901760.

[55] J. Ahn, S. Hong, Y.-S. Shim, J. Park, *Appl. Sci.* **2020**, *10*, 8780.

[56] R. Sakalys, K. W. Kho, T. E. Keyes, *Sens. Actuators, B* **2021**, *340*, 129970.

[57] N. Chiang, L. Scarabelli, G. A. Vinnacombe-Willson, L. A. Pérez, C. Dore, A. Mihi, S. J. Jonas, P. S. Weiss, *ACS Mater. Lett.* **2021**, *3*, 282.

[58] A. Garg, W. Nam, W. Zhou, *ACS Appl. Mater. Interfaces* **2020**, *12*, 56290.

[59] M. Obst, G. Arnauts, A. J. Cruz, M. Calderon Gonzalez, K. Marcoen, T. Hauffman, R. Ameloot, *Angewandte Chemie. Intl. Edit.* **2021**, *60*, 25668.

[60] J. Zhang, Y. Li, K. Cao, R. Chen, *Nanomanuf. Metrol.* **2022**, *5*, 191.

[61] S. Djoumi, F. Kail, P. R. I. Cabarrocas, L. Chahed, *Thin Solid Films* **2022**, *758*, 139447.

[62] S. Jambhulkar, S. Liu, P. Vala, W. Xu, D. Ravichandran, Y. Zhu, K. Bi, Q. Nian, X. Chen, K. Song, *ACS Nano* **2021**, *15*, 12057.

[63] S. Kiruthika, B. Radha, *ACS Omega* **2020**, *5*, 20739.

[64] F. Yang, P. Li, X. Li, L. Huo, J. Chen, R. Chen, W. Na, W. Tang, L. Liang, W. Su, *Appl. Surf. Sci.* **2013**, *274*, 241.

[65] C. Lu, H. Möhwald, A. Fery, *Soft Matter.* **2007**, *3*, 1530.

[66] D. Liu, W. Cai, M. Marin, Y. Yin, Y. Li, *ChemNanoMat* **2019**, *5*, 1338.

[67] S. Shi, T. P. Russell, *Adv. Mater.* **2018**, *30*, 1800714.

[68] Z. Nie, A. Petukhova, E. Kumacheva, *Nat. Nanotechnol.* **2010**, *5*, 15.

[69] A. Klinkova, R. M. Choueiri, E. Kumacheva, *Chem. Soc. Rev.* **2014**, *43*, 3976.

[70] Y.-H. Suh, D.-W. Shin, Y. T. Chun, *RSC Adv.* **2019**, *9*, 38085.

[71] Z. Lai, Y. Chen, C. Tan, X. Zhang, H. Zhang, *Chem* **2016**, *1*, 59.

[72] Y.-Z. Zhang, Y. Wang, Q. Jiang, J. K. El-Demellawi, H. Kim, H. N. Alshareef, *Adv. Mater.* **2020**, *32*, 1908486.
[73] B. Elder, R. Neupane, E. Tokita, U. Ghosh, S. Hales, Y. L. Kong, *Adv. Mater.* **2020**, *32*, 1907142.
[74] W. Feng, E. Ueda, P. A. Levkin, *Adv. Mater.* **2018**, *30*, 1706111.
[75] D. Mijatovic, J. C. T. Eijkel, A. Van Den Berg, *Lab Chip* **2005**, *5*, 492.
[76] G. A. Ozin, K. Hou, B. V. Lotsch, L. Cademartiri, D. P. Puzzo, F. Scotognella, A. Ghadimi, J. Thomson, *Mater. Today* **2009**, *12*, 12.
[77] Y. Lei, S. Yang, M. Wu, G. Wilde, *Chem. Soc. Rev.* **2011**, *40*, 1247.
[78] C. Yilmaz, A. Sirman, A. Halder, A. Busnaina, *ACS Nano* **2017**, *11*, 7679.
[79] A. Saric, A. Cacciuto, *Soft Matter.* **2013**, *9*, 6677.
[80] J. Li, A. Alfares, Y. Zheng, *iScience* **2022**, *25*, 104035.
[81] T. Udayabhaskararao, T. Altantzis, L. Houben, M. Coronado-Puchau, J. Langer, R. Popovitz-Biro, L. M. Liz-Marzán, L. Vukovic, P. Král, S. Bals, R. Klajn, *Science* **2017**, *358*, 514.
[82] A. Dong, J. Chen, P. M. Vora, J. M. Kikkawa, C. B. Murray, *Nature* **2010**, *466*, 474.
[83] K. Kim, H. S. Han, I. Choi, C. Lee, S. Hong, S.-H. Suh, L. P. Lee, T. Kang, *Nat. Commun.* **2013**, *4*, 2182.
[84] L. Song, B. B. Xu, Q. Cheng, X. Wang, X. Luo, X. Chen, T. Chen, Y. Huang, *Sci. Adv.* **2021**, *7*, eabk2852.
[85] Y. Yin, Y. Lu, B. Gates, Y. Xia, *J. Am. Chem. Soc.* **2001**, *123*, 8718.
[86] M. Niederberger, *Adv. Funct. Mater.* **2017**, *27*, 1703647.
[87] D. Falconnet, G. Csucs, H. Michelle Grandin, M. Textor, *Biomaterials* **2006**, *27*, 3044.
[88] O. Sahin, M. Ashokkumar, P. M. Ajayan, in *Fundamental Biomaterials: Metals*, Elsevier: Amsterdam, The Netherlands, **2018**, pp. 67–78.
[89] M. Verhulsel, M. Vignes, S. Descroix, L. Malaquin, D. M. Vignjevic, J.-L. Viovy, *Biomaterials* **2014**, *35*, 1816.
[90] A. Vats, N. S. Tolley, J. M. Polak, J. E. Gough, *Clin Otolaryngol* **2003**, *28*, 165.
[91] N. Ostrovsky, G. Le Saux, U. Argaman, I. Chen, T. Chen, C.-H. Chang, G. Makov, M. Schvartzman, *Langmuir* **2021**, *37*, 9098.
[92] X. Huang, S. Li, Y. Huang, S. Wu, X. Zhou, S. Li, C. L. Gan, F. Boey, C. A. Mirkin, H. Zhang, *Nat. Commun.* **2011**, *2*, 292.
[93] M. E. J. Hummel, C. Stelling, B. A. F. Kopera, F. A. Nutz, M. Karg, M. Retsch, S. Förster, *Langmuir* **2019**, *35*, 973.
[94] M. Mastrangeli, S. Abbasi, C. Varel, C. Van Hoof, J.-P. Celis, K. F. Böhringer, *J. Micromech. Microeng.* **2009**, *19*, 083001.
[95] A. Kaliyaraj Selva Kumar, Y. Zhang, D. Li, R. G. Compton, *Electrochem. Commun.* **2020**, *121*, 106867.
[96] S. Choi, S. Stassi, A. P. Pisano, T. I. Zohdi, *Langmuir* **2010**, *26*, 11690.
[97] P. He, B. Derby, *Adv. Mater. Interfaces* **2017**, *4*, 1700944.
[98] W. Han, Z. Lin, *Angew. Chem., Int. Ed.* **2012**, *51*, 1534.
[99] X. Shen, C.-M. Ho, T.-S. Wong, *J. Phys. Chem. B* **2010**, *114*, 5269.
[100] Y. Ooi, I. Hanasaki, D. Mizumura, Y. Matsuda, *Sci. Technol. Adv. Mater.* **2017**, *18*, 316.
[101] L. Li, W. Li, Q. Sun, X. Liu, J. Jiu, M. Tenjimbayashi, M. Kanehara, T. Nakayama, T. Minari, *Small* **2021**, *17*, 2101754.
[102] L. Xu, X. Li, X. Wang, Z. Zou, *Nanotechnology* **2021**, *32*, 135601.
[103] M. Szekeres, O. Kamalin, R. A. Schoonheydt, K. Wostyn, K. Clays, A. Persoons, I. Dékány, *J. Mater. Chem.* **2002**, *12*, 3268.
[104] B. G. Prevo, O. D. Velev, *Langmuir* **2004**, *20*, 2099.
[105] X. Ye, J. Huang, Y. Zeng, L-X. Sun, F. Geng, H.-J. Liu, F.-R. Wang, X.-D. Jiang, W.-D. Wu, W.-G. Zheng, *Nanomaterials* **2017**, *7*, 291.
[106] V. Lotito, T. Zambelli, *Langmuir* **2016**, *32*, 9582.
[107] K. Song, R. Polak, D. Chen, M. F. Rubner, R. E. Cohen, K. A. Askar, *ACS Appl. Mater. Interfaces* **2016**, *8*, 20396.
[108] J. Chen, Z. Xue, S. Feng, B. Tu, D. Zhao, *J. Colloid Interface Sci.* **2014**, *429*, 62.
[109] Y. Mino, S. Watanabe, M. T. Miyahara, *Langmuir* **2015**, *31*, 4121.
[110] C. García Núñez, W. T. Navaraj, F. Liu, D. Shakthivel, R. Dahiya, *ACS Appl. Mater. Interfaces* **2018**, *10*, 3058.
[111] M. Ghosh, F. Fan, K. J. Stebe, *Langmuir* **2007**, *23*, 2180.
[112] D. I. Petukhov, A. P. Chumakov, A. S. Kan, V. A. Lebedev, A. A. Eliseev, O. V. Konovalov, A. A. Eliseev, *Nanoscale* **2019**, *11*, 9980.
[113] X. Li, J. F. Gilchrist, *Langmuir* **2016**, *32*, 1220.
[114] S. Jeong, L. Hu, H. R. Lee, E. Garnett, J. W. Choi, Y. Cui, *Nano Lett.* **2010**, *10*, 2989.
[115] T. Ogi, L. B. Modesto-Lopez, F. Iskandar, K. Okuyama, *Colloids Surf. A* **2007**, *297*, 71.
[116] M. Mariano, O. Mashtalir, F. Q. Antonio, W.-H. Ryu, B. Deng, F. Xia, Y. Gogotsi, A. D. Taylor, *Nanoscale* **2016**, *8*, 16371.
[117] E. Aydin, J. K. El-Demellawi, E. Yarali, F. Aljamaan, S. Sansoni, A. U. Rehman, G. Harrison, J. Kang, A. El Labban, M. De Bastiani, A. Razzaq, E. Van Kerschaver, T. G. Allen, O. F. Mohammed, T. Anthopoulos, H. N. Alshareef, S. De Wolf, *ACS Nano* **2022**, *16*, 2419.
[118] H-L. Nie, X. Dou, Z. Tang, H. D. Jang, J. Huang, *J. Am. Chem. Soc.* **2015**, *137*, 10683.
[119] M. Tago, M. Takasaki, Y. Tokura, Y. Oaki, H. Imai, *Langmuir* **2021**, *37*, 6533.
[120] S. J. Kim, J. Choi, K. Maleski, K. Hantanasirisakul, H.-T. Jung, Y. Gogotsi, C. W. Ahn, *ACS Appl. Mater. Interfaces* **2019**, *11*, 32320.
[121] L. J. Cote, F. Kim, J. Huang, *J. Am. Chem. Soc.* **2009**, *131*, 1043.
[122] Y. Li, Z. Zhang, M. Su, Z. Huang, Z. Li, F. Li, Q. Pan, W. Ren, X. Hu, L. Li, Y. Song, *Nanoscale* **2018**, *10*, 22374.
[123] J. Feng, H. Xia, F. You, H. Mao, X. Ma, H. Tao, X. Zhao, M.-C. Wang, *J. Alloys Compd.* **2018**, *735*, 607.
[124] B. Su, Y. Wu, L. Jiang, *Chem. Soc. Rev.* **2012**, *41*, 7832.
[125] R. Bian, L. Meng, M. Zhang, L. Chen, H. Liu, *ACS Omega* **2019**, *4*, 1816.
[126] T. Brezesinski, M. Groenewolt, A. Gibaud, N. Pinna, M. Antonietti, B. Smarsly, *Adv. Mater.* **2006**, *18*, 2260.
[127] J. Annett, G. L. W. Cross, *Nature* **2016**, *535*, 271.
[128] D. Gentili, G. Foschi, F. Valle, M. Cavallini, F. Biscarini, *Chem. Soc. Rev.* **2012**, *41*, 4430.
[129] J. Huang, F. Kim, A. R. Tao, S. Connor, P. Yang, *Nature Mater* **2005**, *4*, 896.
[130] J. Xie, J. Guo, D. Wang, Y. Cang, W. Zhang, J. Zhou, B. Peng, Y. Li, J. Cui, L. Chen, G. Fytas, X. Deng, *Adv. Mater. Interfaces* **2021**, *8*, 2000222.
[131] H. S. Kim, C. H. Lee, P. K. Sudeep, T. Emrick, A. J. Crosby, *Adv. Mater.* **2010**, *22*, 4600.
[132] D.-O. Kim, M. Pack, A. Rokoni, P. Kaneelil, Y. Sun, *Soft Matter.* **2018**, *14*, 9599.
[133] S. Kinge, M. Crego-Calama, D. N. Reinhoudt, *ChemPhysChem* **2008**, *9*, 20.
[134] H. Kim, M.-W. Jung, S. Myung, D. Jung, S. S. Lee, K.-J. Kong, J. Lim, J.-H. Lee, C. Y. Park, K.-S. An, *J. Mater. Chem. C* **2013**, *1*, 1076.
[135] J. J. Giner-Casares, J. Reguera, *Nanoscale* **2016**, *8*, 16589.
[136] H. Wang, H. Li, P. Gu, C. Huang, S. Chen, C. Hu, E. Lee, J. Xu, J. Zhu, *Nanoscale* **2023**, *15*, 2018.
[137] Z. Chai, A. Childress, A. A. Busnaina, *ACS Nano* **2022**, *16*, 17641.
[138] M. S. Lee, D. W. Yee, M. Ye, R. J. Macfarlane, *J. Am. Chem. Soc.* **2022**, *144*, 3330.
[139] S. Lee, K. Sim, S Y Moon, J. Choi, Y. Jeon, J.-M. Nam, S.-J. Park, *Adv. Mater.* **2021**, *33*, 2007668.
[140] J. A. Rogers, H. H. Lee, *Unconventional Nanopatterning Techniques and Applications*, John Wiley & Sons, Inc, Hoboken, NJ, USA **2008**.
[141] Y. Chen, T. Liang, L. Chen, Y. Chen, B.-R. Yang, Y. Luo, G.-S. Liu, *Nanoscale Horiz.* **2022**, *7*, 1299.
[142] T. Kraus, L. Malaquin, H. Schmid, W. Riess, N. D. Spencer, H. Wolf, *Nat. Nanotechnol.* **2007**, *2*, 570.
[143] V. Flauraud, M. Mastrangeli, G. D. Bernasconi, J. Butet, D. T. L. Alexander, E. Shahrabi, O. J. F. Martin, J. Brugger, *Nat. Nanotechnol.* **2017**, *12*, 73.

[144] N. Aubry, P. Singh, M. Janjua, S. Nudurupati, *Proc. Natl. Acad. Sci. U.S.A.* **2008**, *105*, 3711.
[145] M. Zhang, L. Meng, H. Deng, H. Liu, *Mater. Chem. Front.* **2021**, *5*, 5247.
[146] X. Liu, M. Wei, Q. Wang, Y. Tian, J. Han, H. Gu, H. Ding, Q. Chen, K. Zhou, Z. Gu, *Adv. Mater.* **2021**, *33*, 2100332.
[147] X. Zhou, Y. Zhou, J. C. Ku, C. Zhang, C. A. Mirkin, *ACS Nano* **2014**, *8*, 1511.
[148] Y. Hu, Z. Lao, B. P. Cumming, D. Wu, J. Li, H. Liang, J. Chu, W. Huang, M. Gu, *Proc. Natl. Acad. Sci. USA* **2015**, *112*, 6876.
[149] S.-K. Wu, T.-P. Tang, W. J. Tseng, *J. Mater. Sci.* **2008**, *43*, 6453.
[150] Z. Lao, D. Pan, H. Yuan, J. Ni, S. Ji, W. Zhu, Y. Hu, J. Li, D. Wu, J. Chu, *ACS Nano* **2018**, *12*, 10142.
[151] J. B. Lee, H. Walker, Y. Li, T. W. Nam, A. Rakovich, R. Sapienza, Y. S. Jung, Y. S. Nam, S. A. Maier, E. Cortés, *ACS Nano* **2020**, *14*, 17693.
[152] R. Liu, Y. Liu, J. Chen, Q. Kang, L. Wang, W. Zhou, Z. Huang, X. Lin, Y. Li, P. Li, X. Feng, G. Wu, Y. Ma, W. Huang, *Nano Energy* **2017**, *33*, 325.
[153] Y. Lin, Z. Su, E. Balizan, Z. Niu, Q. Wang, *Langmuir* **2010**, *26*, 12803.
[154] B. Charlot, F. Bardin, N. Sanchez, P. Roux, S. Teixeira, E. Schwob, *Biomicrofluidics* **2014**, *8*, 014103.
[155] T. Chen, B. M. Reinhard, *Adv. Mater.* **2016**, *28*, 3522.
[156] S. Ni, J. Leemann, H. Wolf, L. Isa, *Faraday Discuss.* **2015**, *181*, 225.
[157] N. Thomas, S. Shivkumar, E. Mani, *Phys. Chem. Chem. Phys.* **2020**, *22*, 14201.
[158] M. Collet, S. Salomon, N. Y. Klein, F. Seichepine, C. Vieu, L. Nicu, G. Larrieu, *Adv. Mater.* **2015**, *27*, 1268.
[159] Y. Sharma, A. Dhawan, *J. Phys. Commun.* **2019**, *3*, 115013.
[160] C. Hanske, E. H. Hill, D. Vila-Liarte, G. González-Rubio, C. Matricardi, A. Mihi, L. M. Liz-Marzán, *ACS Appl. Mater. Interfaces* **2019**, *11*, 11763.
[161] I. Kim, J. Mun, W. Hwang, Y. Yang, J. Rho, *Microsyst. Nanoeng.* **2020**, *6*, 65.
[162] H. Li, J. Wu, X. Qi, Q. He, C. Liusman, G. Lu, X. Zhou, H. Zhang, *Small* **2013**, *9*, 382.
[163] J. Wu, H. Li, X. Qi, Q. He, B. Xu, H. Zhang, *Small* **2014**, *10*, 2239.
[164] S. Jeon, J. Lee, R. Park, J. Jeong, M. C. Shin, S. U. Eom, J. Park, S. W. Hong, *Nanomaterials* **2020**, *10*, 1468.
[165] S. Ni, L. Isa, H. Wolf, *Soft Matter.* **2018**, *14*, 2978.
[166] M. Asbahi, Z. Dong, F. Wang, M. S. M. Saifullah, J. K. W. Yang, K. S. L. Chong, *Nanoscale* **2017**, *9*, 9886.
[167] J. Liang, Y. Yan, Y. S. Zhao, *Acc. Mater. Res.* **2021**, *2*, 340.
[168] J. Feng, Q. Song, B. Zhang, Y. Wu, T. Wang, L. Jiang, *Adv. Mater.* **2017**, *29*, 1703143.
[169] Z. Lao, Y. Hu, C. Zhang, L. Yang, J. Li, J. Chu, D. Wu, *ACS Nano* **2015**, *9*, 12060.
[170] J. Shin, S. Han, S. Noh, Y.-T. Yu, J. S. Kim, *Nanotechnology* 505201, **2021**, *32*, 04LT01.
[171] M. Su, Z. Huang, Y. Huang, S. Chen, X. Qian, W. Li, Y. Li, W. Pei, H. Chen, F. Li, Y. Song, *Adv. Mater.* **2017**, *29*, 1605223.
[172] J. M. Jafferson, D. Chatterjee, *Mater. Today Proc.* **2021**, *46*, 1349.
[173] J. P. Rolland, J. M. DeSimone, *US2016/0046072A1*.
[174] X. Peng, X. Kuang, D. J. Roach, Y. Wang, C. M. Hamel, C. Lu, H. J Qi, *Addit. Manuf.* **2021**, *40*, 101911.
[175] S. A. Deomore, S. J. Raykar, *Mater. Today Proc.* **2021**, *44*, 2562.
[176] S. C. Ligon, R. Liska, J. Stampfl, M. Gurr, R. Mülhaupt, *Chem. Rev.* **2017**, *117*, 10212.
[177] M. A. S. R. Saadi, A. Maguire, N. T. Pottackal, M. S. H Thakur, M. M. Ikram, A. J Hart, P. M. Ajayan, M. M. Rahman, *Adv. Mater.* **2022**, *34*, 2108855.
[178] R. Singh, A. Gupta, O. Tripathi, S. Srivastava, B. Singh, A. Awasthi, S. K. Rajput, P. Sonia, P. Singhal, K. K. Saxena, *Mater. Today Proc.* **2020**, *26*, 3058.
[179] Y. Liu, F. Han, F. Li, Y. Zhao, M. Chen, Z. Xu, X. Zheng, H. Hu, J. Yao, T. Guo, W. Lin, Y. Zheng, B. You, P. Liu, Y. Li, L. Qian, *Nat. Commun.* **2019**, *10*, 2409.
[180] W. Xu, S. Jambhulkar, D. Ravichandran, Y. Zhu, M. Kakarla, Q. Nian, B. Azeredo, X. Chen, K. Jin, B. Vernon, D. G. Lott, J. L. Cornella, O. Shefi, G. Miquelard-Garnier, Y. Yang, K. Song, *Small* **2021**, *17*, 2100817.
[181] L.-C. Zhang, Y. Liu, S. Li, Y. Hao, *Adv. Eng. Mater.* **2018**, *20*, 1700842.
[182] A. M. E. Arefin, N. R. Khatri, N. Kulkarni, P. F. Egan, *Polymers* **2021**, *13*, 1499.
[183] D. Ravichandran, W. Xu, M. Kakarla, S. Jambhulkar, Y. Zhu, K. Song, *Addit. Manuf.* **2021**, *47*, 102322.
[184] S.-J. Lee, M. Nowicki, B. Harris, L. G. Zhang, *Tissue Eng., Part A* **2017**, *23*, 491.
[185] M. L. Shofner, K. Lozano, F. J. Rodríguez-Macías, E. V. Barrera, *J. Appl. Polym. Sci.* **2003**, *89*, 3081.
[186] Q. Zhang, F. Zhang, S. P. Medarametla, H. Li, C. Zhou, D. Lin, *Small* **2016**, *12*, 1702.
[187] Q. Zhang, F. Zhang, X. Xu, C. Zhou, D. Lin, *ACS Nano* **2018**, *12*, 1096.
[188] X. Li, Y. Yang, Y. Zhang, T. Wang, Z. Yang, Q. Wang, X. Zhang, *Mater. Des.* **2020**, *191*, 108606.
[189] J. H. Kim, W. S. Chang, D. Kim, J. R. Yang, J. T. Han, G.-W. Lee, J. T Kim, S. K. Seol, *Adv. Mater.* **2015**, *27*, 157.
[190] M. Su, Z. Huang, Y. Li, X. Qian, Z. Li, X. Hu, Q. Pan, F. Li, L. Li, Y. Song, *Adv. Mater.* **2018**, *30*, 1703963.
[191] K. E. Roskov, K. A. Kozek, W.-C. Wu, R. K. Chhetri, A. L. Oldenburg, R. J. Spontak, J. B. Tracy, *Langmuir* **2011**, *27*, 13965.
[192] Y. L. Kong, I. A. Tamargo, H. Kim, B. N. Johnson, M. K. Gupta, T.-W. Koh, H-A. Chin, D. A. Steingart, B. P. Rand, M. C. Mcalpine, *Nano Lett.* **2019**, *19*, 2187.
[193] L. Lu, P. Guo, Y. Pan, *J. Manuf. Sci. Eng.* **2017**, *139*, 071008.
[194] A. Sydney Gladman, E. A. Matsumoto, R. G. Nuzzo, L. Mahadevan, J. A. Lewis, *Nature Mater.* **2016**, *15*, 413.
[195] W. Xu, S. Jambhulkar, Y. Zhu, D. Ravichandran, M. Kakarla, B. Vernon, D. G. Lott, J. L. Cornella, O. Shefi, G. Miquelard-Garnier, Y. Yang, K. Song, *Composites, Part B* **2021**, *223*, 109102.
[196] J.-U. Park, M. Hardy, S. J. Kang, K. Barton, K. Adair, D. K. Mukhopadhyay, C. Y. Lee, M. S. Strano, A. G. Alleyne, J. G. Georgiadis, P. M. Ferreira, J. A. Rogers, *Nature Mater.* **2007**, *6*, 782.
[197] D. Luo, C. Yan, T. Wang, *Small* **2015**, *11*, 5984.
[198] M. Striccoli, *Science* **2017**, *357*, 353.
[199] L. Alison, S. Menasce, F. Bouville, E. Tervoort, I. Mattich, A. Ofner, A. R. Studart, *Sci. Rep.* **2019**, *9*, 409.
[200] F. Klein, B. Richter, T. Striebel, C. M. Franz, G. V. Freymann, M. Wegener, M. Bastmeyer, *Adv. Mater.* **2011**, *23*, 1341.
[201] M. E Hossain Bhuiyan, S. Moreno, C. Wang, M. Minary-Jolandan, *ACS Appl. Mater. Interfaces* **2021**, *13*, 19271.
[202] D. E. Yunus, S. Sohrabi, R. He, W. Shi, Y. Liu, *J. Micromech. Microeng.* **2017**, *27*, 045016.
[203] W. Zhu, J. Li, Y. J. Leong, I. Rozen, X. Qu, R. Dong, Z. Wu, W. Gao, P. H. Chung, J. Wang, S. Chen, *Adv. Mater.* **2015**, *27*, 4411.
[204] E. B. Joyee, A. Szmelter, D. Eddington, Y. Pan, *ACS Appl. Mater. Interfaces* **2020**, *12*, 42357.
[205] S. Abdolhosseinzadeh, R. Schneider, A. Verma, J. Heier, F. Nüesch, C. (J.). Zhang, *Adv. Mater.* **2020**, *32*, 2000716.
[206] E. Quain, T. S. Mathis, N. Kurra, K. Maleski, K. L. Van Aken, M. Alhabeb, H. N. Alshareef, Y. Gogotsi, *Adv. Mater. Technol.* **2019**, *4*, 1800256.
[207] Y. Shao, L. Wei, X. Wu, C. Jiang, Y. Yao, B. Peng, H. Chen, J. Huangfu, Y. Ying, C. J. Zhang, J. Ping, *Nat. Commun.* **2022**, *13*, 3223.
[208] Y. Han, J. Dong, *Adv. Mater. Technol.* **2018**, *3*, 1700268.
[209] S. Jambhulkar, W. Xu, D. Ravichandran, J. Prakash, A. N. Mada Kannan, K. Song, *Nano Lett.* **2020**, *20*, 3199.

[210] B. F. Porter, N. Mkhize, H. Bhaskaran, *Microsyst. Nanoeng.* **2017**, *3*, 17054.

[211] A. Reiser, M. Lindén, P. Rohner, A. Marchand, H. Galinski, A. S. Sologubenko, J. M. Wheeler, R. Zenobi, D. Poulikakos, R. Spolenak, *Nat. Commun.* **2019**, *10*, 1853.

[212] A. Bagheri, J. Jin, *ACS Appl Polym Mater* **2019**, *1*, 593.

[213] M. Pagac, J. Hajnys, Q.-P. Ma, L. Jancar, J. Jansa, P. Stefek, J. Mesicek, *Polymers* **2021**, *13*, 598.

[214] J. R. Tumbleston, D. Shirvanyants, N. Ermoshkin, R. Janusziewicz, A. R. Johnson, D. Kelly, K. Chen, R. Pinschmidt, J. P. Rolland, A. Ermoshkin, E. T. Samulski, J. M. Desimone, *Science* **2015**, *347*, 1349.

[215] S. Jambhulkar, W. Xu, R. Franklin, D. Ravichandran, Y. Zhu, K. Song, *J. Mater. Chem. C* **2020**, *8*, 9495.

[216] I. Liashenko, J. Rosell-Llompart, A. Cabot, *Nat. Commun.* **2020**, *11*, 753.

[217] H. Lee, B. Seong, J. Kim, Y. Jang, D. Byun, *Small* **2014**, *10*, 3918.

[218] G. Xin, W. Zhu, Y. Deng, J. Cheng, L. T. Zhang, A. J. Chung, S. De, J. Lian, *Nat. Nanotechnol.* **2019**, *14*, 168.

[219] Y. Nie, C. Jin, J. X. J. Zhang, *ACS Sens.* **2021**, *6*, 2584.

[220] C. L. Hansen, E. Skordalakes, J. M. Berger, S. R. Quake, *Proc. Natl. Acad. Sci. U.S.A.* **2002**, *99*, 16531.

[221] S. Takayama, E. Ostuni, P. Leduc, K. Naruse, D. E. Ingber, G. M. Whitesides, *Nature* **2001**, *411*, 1016.

[222] J. Son, R. Samuel, B. K. Gale, D. T. Carrell, J. M. Hotaling, *Biomicrofluidics* **2017**, *11*, 054106.

[223] A. R. Jafek, S. Harbertson, H. Brady, R. Samuel, B. K. Gale, *Anal. Chem.* **2018**, *90*, 7190.

[224] A. Bange, H. B Halsall, W. R. Heineman, *Biosens. Bioelectron.* **2005**, *20*, 2488.

[225] M. Safdar, J. Jänis, S. Sánchez, *Lab Chip* **2016**, *16*, 2754.

[226] M. T. Guo, A. Rotem, J. A. Heyman, D. A. Weitz, *Lab Chip* **2012**, *12*, 2146.

[227] K. F. Lei, in *Detection Science* (Eds: F. H. Labeed, H. O. Fatoyinbo), Royal Society Of Chemistry, Cambridge **2014**, pp. 1–28.

[228] J. Hwang, Y. H. Cho, M. S. Park, B. H Kim, *Int. J. Precis. Eng. Manuf.* **2019**, *20*, 479.

[229] N. Bhattacharjee, A. Urrios, S. Kang, A. Folch, *Lab Chip* **2016**, *16*, 1720.

[230] A. I. Shallan, P. Smejkal, M. Corban, R. M. Guijt, M. C. Breadmore, *Anal. Chem.* **2014**, *86*, 3124.

[231] M. Zeraatkar, D. Filippini, G. Percoco, *Micromachines* **2019**, *10*, 298.

[232] E. A. Guzzi, M. W. Tibbitt, *Adv. Mater.* **2020**, *32*, 1901994.

[233] R. D. Sochol, E. Sweet, C. C. Glick, S. Venkatesh, A. Avetisyan, K. F. Ekman, A. Raulinaitis, A. Tsai, A. Wienkers, K. Korner, K. Hanson, A. Long, B. J. Hightower, G. Slatton, D. C. Burnett, T. L. Massey, K. Iwai, L. P. Lee, K. S. J. Pister, L. Lin, *Lab Chip* **2016**, *16*, 668.

[234] F. Kotz, P. Risch, K. Arnold, S. Sevim, J. Puigmartí-Luis, A. Quick, M. Thiel, A. Hrynevich, P. D. Dalton, D. Helmer, B. E. Rapp, *Nat. Commun.* **2019**, *10*, 1439.

[235] M. Layani, X. Wang, S. Magdassi, *Adv. Mater.* **2018**, *30*, 1706344.

[236] D. Wu, L.-G. Niu, S.-Z. Wu, J. Xu, K. Midorikawa, K. Sugioka, *Lab Chip* **2015**, *15*, 1515.

[237] G. Weisgrab, A. Ovsianikov, P. F. Costa, *Adv. Mater. Technol.* **2019**, *4*, 1900275.

[238] J.-H. Kim, J.-W. Park, *ACS Appl. Mater. Interfaces* **2018**, *10*, 9704.

[239] R. Paul, Y. Zhao, D. Coster, X. Qin, K. Islam, Y. Wu, Y. Liu, *Nat. Commun.* **2023**, *14*, 4520.

[240] J. Chen, Y. Zhou, D. Wang, F. He, V. M. Rotello, K. R. Carter, J. J. Watkins, S. R. Nugen, *Lab Chip* **2015**, *15*, 3086.

[241] K. T. M. Tran, T. D. Nguyen, *J. Sci.: Adv. Mater. Devices* **2017**, *2*, 1.

[242] L. E. Freed, G. C. Engelmayr, J. T. Borenstein, F. T. Moutos, F. Guilak, *Adv. Mater.* **2009**, *21*, 3410.

[243] X. Gu, I. Gunkel, T. P. Russell, *Philos Trans A Math Phys Eng Sci* **2013**, *371*, 20120306.

[244] L. Zhang, W. Wang, X.-J. Ju, R. Xie, Z. Liu, L.-Y. Chu, *RSC Adv.* **2015**, *5*, 5638.

[245] D. J. Guckenberger, T. E. De Groot, A. M. D. Wan, D. J. Beebe, E. W. K. Young, *Lab Chip* **2015**, *15*, 2364.

[246] E. Ermis, Z. Bagheri, E. Behroodi, H. Latifi, M. Rahimifard, E. Ajorlou, *J. Sci.: Adv. Mater. Devices* **2022**, *7*, 100404.

[247] E. Azarsa, M. Jeyhani, A. Ibrahim, S. S. H. Tsai, M. Papini, *Biomicrofluidics* **2020**, *14*, 044103.

[248] H. V. Nguyen, K. Y Kim, H. Nam, S. Y. Lee, T. Yu, T. S. Seo, *Lab Chip* **2020**, *20*, 3293.

[249] D. Ogonczyk, J. Wegrzyn, P. Jankowski, B. Dabrowski, P. Garstecki, *Lab Chip* **2010**, *10*, 1324.

[250] S. Scott, Z. Ali, *Micromachines* **2021**, *12*, 319.

[251] B. Gale, A. Jafek, C. Lambert, B. Goenner, H. Moghimifam, U. Nze, S. Kamarapu, *Inventions* **2018**, *3*, 60.

[252] T-Y. Lin, T. Do, P. Kwon, P. B. Lillehoj, *Lab Chip* **2017**, *17*, 241.

[253] F. Akther, S. B. Yakob, N.-T. Nguyen, H. T. Ta, *Biosensors* **2020**, *10*, 182.

[254] C. J. Bettinger, E. J. Weinberg, K. M. Kulig, J. P. Vacanti, Y. Wang, J. T. Borenstein, R. Langer, *Adv. Mater.* **2006**, *18*, 165.

[255] M. Liu, R. He, J. Yang, W. Zhao, C. Zhou, *ACS Appl. Mater. Interfaces* **2016**, *8*, 7709.

[256] K. L. Wlodarczyk, D. P. Hand, M. M Maroto-Valer, *Sci. Rep.* **2019**, *9*, 20215.

[257] R. Ye, D. K. James, J. M. Tour, *Adv. Mater.* **2019**, *31*, 1803621.

[258] F. Yu, P. Li, H. Shen, S. Mathur, C.-M. Lehr, U. Bakowsky, F. Mücklich, *Biomaterials* **2005**, *26*, 2307.

[259] X. Li, H. Li, J. Liu, X. Qi, X. Zeng, *Appl. Surf. Sci.* **2004**, *233*, 51.

[260] C. Iliescu, H. Taylor, M. Avram, J. Miao, S. Franssila, *Biomicrofluidics* **2012**, *6*, 016505.

[261] P. Sarma, P. K. Patowari, *MNS* **2018**, *10*, 137.

[262] Y. Geng, S. Ling, J. Huang, J. Xu, *Small* **2020**, *16*, 1906357.

[263] K. Sugioka, J. Xu, D. Wu, Y. Hanada, Z. Wang, Y. Cheng, K. Midorikawa, *Lab Chip* **2014**, *14*, 3447.

[264] P. Serra, A. Piqué, *Adv. Mater. Technol.* **2019**, *4*, 1800099.

[265] Y. Cao, X. Zeng, Z. Cai, J. Duan, in *Advances in Laser Materials Processing*, Elsevier, Woodhead Publishing, Swaston, United Kingdom, **2010**, pp. 629–670.

[266] Y. Hwang, O. H. Paydar, R. N. Candler, *Sens. Actuators, A* **2015**, *226*, 137.

[267] B.-B. Xu, H. Xia, L.-G. Niu, Y.-L. Zhang, K. Sun, Q.-D. Chen, Y. Xu, Z.-Q. Lv, Z.-H. Li, H. Misawa, H-B. Sun, *Small* **2010**, *6*, 1762.

[268] J. Zhu, Z. Hu, C. Song, N. Yi, Z. Yu, Z. Liu, S. Liu, M. Wang, M. G. Dexheimer, J. Yang, H. Cheng, *Mater. Today Phys.* **2021**, *18*, 100377.

[269] P. A. Kralchevsky, N. D. Denkov, *Curr. Opin. Colloid Interface Sci.* **2001**, *6*, 383.

[270] P. Lambert, A. Delchambre, *Langmuir* **2005**, *21*, 9537.

[271] M. Trebbin, D. Steinhauser, J. Perlich, A. Buffet, S. V. Roth, W. Zimmermann, J. Thiele, S. Förster, *Proc. Natl. Acad. Sci. USA* **2013**, *110*, 6706.

[272] M. Akella, J. J. Juárez, *ACS Omega* **2018**, *3*, 1425.

[273] S.-X. Li, H. Xia, Y.-S. Xu, C. Lv, G. Wang, Y.-Z. Dai, H-B. Sun, *Nanoscale* **2019**, *11*, 4925.

[274] Y. L. Kong, F. Boulogne, H. Kim, J. Nunes, J. Feng, H. A. Stone, *Langmuir* **2015**, *31*, 12560.

[275] M. K. Kim, B. G. Cha, J. Kim, *Chem. Mater.* **2022**, *34*, 4437.

[276] G. F. Trindade, F. Wang, J. Im, Y. He, A. Balogh, D. Scurr, I. Gilmore, M. Tiddia, E. Saleh, D. Pervan, L. Turyanska, C. J. Tuck, R. Wildman, R. Hague, C. J. Roberts, *Commun Mater* **2021**, *2*, 47.

[277] J. Liu, W. Fang, S. Gao, Y. Chen, S. Chen, C. Hu, S. Cai, Z. Liu, X. Liu, *Mater. Des.* **2020**, *192*, 108753.

[278] M. Solsona, J. C. Vollenbroek, C. B. M. Tregouet, A.-E. Nieuwelink, W. Olthuis, A. Van Den Berg, B. M. Weckhuysen, M. Odijk, *Lab Chip* **2019**, *19*, 3575.

[279] M. V. Bandulasena, G. T. Vladisavljevic, O. G. Odunmbaku, B. Benyahia, *Chem. Eng. Sci.* **2017**, *171*, 233.

[280] Y. Lin, E. Balizan, L. A Lee, Z. Niu, Q. Wang, *Angew. Chem., Int. Ed.* **2010**, *49*, 868.

[281] L. Jiang, N. S. Korivi, in *Nanolithography*, Elsevier, Woodhead Publishing, Swaston, United Kingdom, **2014**, pp. 424–443.

[282] S. Kumar, S. Kumar, M. A Ali, P. Anand, V. V. Agrawal, R. John, S. Maji, B. D. Malhotra, *Biotechnol. J.* **2013**, *8*, 1267.

[283] Y. Song, B. Lin, T. Tian, X. Xu, W. Wang, Q. Ruan, J. Guo, Z. Zhu, C. Yang, *Anal. Chem.* **2019**, *91*, 388.

[284] J. Aleman, T. Kilic, L. S. Mille, S. R Shin, Y. S Zhang, *Nat. Protoc.* **2021**, *16*, 2564.

[285] E. Ueda, P. A. Levkin, *Adv. Mater.* **2013**, *25*, 1234.

[286] T.-S. Wong, S. H. Kang, S. K. Y. Tang, E. J. Smythe, B. D. Hatton, A. Grinthal, J. Aizenberg, *Nature* **2011**, *477*, 443.

[287] T. Ding, Q. Zhao, S. K. Smoukov, J. J. Baumberg, *Adv. Opt. Mater.* **2014**, *2*, 1098.

[288] R. D. Deegan, O. Bakajin, T. F. Dupont, G. Huber, S. R. Nagel, T. A. Witten, *Nature* **1997**, *389*, 827.

[289] K. Tufail Chaudhary, in *Thin Films* (Ed: A. Esther Ares), IntechOpen, London, United Kingdom, **2021**.

[290] L. Wu, Z. Dong, M. Kuang, Y. Li, F. Li, L. Jiang, Y. Song, *Adv. Funct. Mater.* **2015**, *25*, 2237.

[291] T. Furuta, M. Sakai, T. Isobe, S. Matsushita, A. Nakajima, *Langmuir* **2011**, *27*, 7307.

[292] N. Denkov, O. Velev, P. Kralchevski, I. Ivanov, H. Yoshimura, K. Nagayama, *Langmuir* **1992**, *8*, 3183.

[293] C. Thornton, *J. Phys. D: Appl. Phys.* **1991**, *24*, 1942.

[294] X. Xing, Z. Man, J. Bian, Y. Yin, W. Zhang, Z. Lu, *Nat. Commun.* **2020**, *11*, 6002.

[295] T. Yamada, K. Fukuhara, K. Matsuoka, H. Minemawari, J. ʼ. Tsutsumi, N. Fukuda, K. Aoshima, S. Arai, Y. Makita, H. Kubo, T. Enomoto, T. Togashi, M. Kurihara, T. Hasegawa, *Nat. Commun.* **2016**, *7*, 11402.

[296] D. V. Talapin, J.-S. Lee, M. V. Kovalenko, E. V. Shevchenko, *Chem. Rev.* **2010**, *110*, 389.

[297] Y. Yin, A. P Alivisatos, *Nature* **2005**, *437*, 664.

[298] in *Handbook of Nanofabrication* (Ed: G. P. Wiederrecht), Elsevier, Amsterdam, Boston **2010**.

[299] B. Bhushan, *Springer Handbook of Nanotechnology*, Springer, Berlin Heidelberg, New York, NY **2017**.

[300] J. Yin, C. Lu, *Soft Matter.* **2012**, *8*, 6528.

[301] S. S. Raj, R. M. Mathew, Y. Nair, Aruna S. T., Vinod T. P., *ChemistrySelect* **2022**, *7*, 202200714.

[302] G. Lee, M. Zarei, Q. Wei, Y. Zhu, S. G. Lee, *Small* **2022**, *18*, 2203491.

[303] H. Schott, *Journal of Macromolecular Science, Part B* **1992**, *31*, 1.

[304] M. Byun, C. D. Santangelo, R. C. Hayward, *Soft Matter.* **2013**, *9*, 8264.

[305] J. Yoon, J. Kim, R. C. Hayward, *Soft Matter.* **2010**, *6*, 5807.

[306] J. Kim, J. A. Hanna, R. C. Hayward, C. D. Santangelo, *Soft Matter.* **2012**, *8*, 2375.

[307] F. Li, H. Hou, J. Yin, X. Jiang, *Sci. Adv.* **2018**, *4*, eaar5762.

[308] S. Deng, V. Berry, *Mater. Today* **2016**, *19*, 197.

[309] C.-M. Chen, S. Yang, *Polym. Int.* **2012**, *61*, 1041.

[310] B. A. Junisu, I. C-Y. Chang, C.-C. Lin, Y.-S. Sun, *Langmuir* **2022**, *38*, 3907.

[311] C. Hanske, M. Tebbe, C. Kuttner, V. Bieber, V. V. Tsukruk, M. Chanana, T. A. F. König, A. Fery, *Nano Lett.* **2014**, *14*, 6863.

[312] A. Schweikart, A. Fery, *Microchim. Acta* **2009**, *165*, 249.

[313] J. Genzer, J. Groenewold, *Soft Matter.* **2006**, *2*, 310.

[314] H. Jiang, D.-Y. Khang, J. Song, Y. Sun, Y. Huang, J. A. Rogers, *Proc. Natl. Acad. Sci. U.S.A.* **2007**, *104*, 15607.

[315] T. Kraus, D. Brodoceanu, N. Pazos-Perez, A. Fery, *Adv. Funct. Mater.* **2013**, *23*, 4529.

[316] D. Schletz, J. Schultz, P. L. Potapov, A. M. Steiner, J. Krehl, T. A. F. König, M. Mayer, A. Lubk, A. Fery, *Adv. Optical Mater.* **2021**, *9*, 2001983.

[317] S. Nagashima, S. M. Yoon, D. H Kim, A. Nakatani, M.-W. Moon, *Adv Materials Inter* **2022**, *9*, 2102243.

[318] X. Wang, M. Sperling, M. Reifarth, A. Böker, *Small* **2020**, *16*, 1906721.

[319] J. Lee, J. Seo, D. Kim, S. Shin, S. Lee, C. Mahata, H.-S. Lee, B.-W. Min, T. Lee, *ACS Appl. Mater. Interfaces* **2014**, *6*, 9053.

[320] Y. Yu, C. Ng, T. A. F. König, A. Fery, *Langmuir* **2019**, *35*, 8629.

[321] H. Feng, X. Lu, W. Wang, N.-G. Kang, J. Mays, *Polymers* **2017**, *9*, 494.

[322] S. Krishnamoorthy, C. Hinderling, H. Heinzelmann, *Mater. Today* **2006**, *9*, 40.

[323] Y.-C. Tseng, S. B. Darling, *Polymers* **2010**, *2*, 470.

[324] F. Wang, P. Altschuh, L. Ratke, H. Zhang, M. Selzer, B. Nestler, *Adv. Mater.* **2019**, *31*, 1806733.

[325] J. Bang, U. Jeong, D. Y Ryu, T. P. Russell, C. J. Hawker, *Adv. Mater.* **2009**, *21*, 4769.

[326] J. K. Kim, S. Y. Yang, Y. Lee, Y. Kim, *Prog. Polym. Sci.* **2010**, *35*, 1325.

[327] M. P. Kim, G.-R. Yi, *Front. Mater.* **2015**, *2*, https://doi.org/10.3389/fmats.2015.00045.

[328] A. H. Gröschel, A. H. E. Müller, *Nanoscale* **2015**, *7*, 11841.

[329] G. Pound-Lana, P. Bézard, C. Petit-Etienne, S. Cavalaglio, G. Cunge, B. Cabannes-Boué, G. Fleury, X. Chevalier, M. Zelsmann, *ACS Appl. Mater. Interfaces* **2021**, *13*, 49184.

[330] Z. Liu, H. Huang, T. He, *Small* **2013**, *9*, 505.

[331] J. Malmström, J. Travas-Sejdic, *J. Appl. Polym. Sci.* **2014**, *131*, n/a.

[332] N. Eren, O. Burg, E. Michman, I. Popov, R. Shenhar, *Polymer* **2022**, *245*, 124727.

[333] E. H. Tadd, J. Bradley, R. Tannenbaum, *Langmuir* **2002**, *18*, 2378.

[334] Q. Zhang, S. Gupta, T. Emrick, T. P. Russell, *J. Am. Chem. Soc.* **2006**, *128*, 3898.

[335] M. Li, C. K. Ober, *Mater. Today* **2006**, *9*, 30.

[336] J. P. Spatz, T. Herzog, S. Mößmer, P. Ziemann, M. Möller, *Adv. Mater.* **1999**, *11*, 149.

[337] R. S. Kane, R. E. Cohen, R. Silbey, *Chem. Mater.* **1996**, *8*, 1919.

[338] N. C. Bigall, B. Nandan, E. B Gowd, A. Horechyy, A. Eychmüller, *ACS Appl. Mater. Interfaces* **2015**, *7*, 12559.

[339] X. Li, K. H. A. Lau, D. H. Kim, W. Knoll, *Langmuir* **2005**, *21*, 5212.

[340] J. Q. Lu, T. E. Kopley, N. Moll, D. Roitman, D. Chamberlin, Q. Fu, J. Liu, T. P. Russell, D. A. Rider, I. Manners, M. A. Winnik, *Chem. Mater.* **2005**, *17*, 2227.

[341] K. Temple, K. Kulbaba, K. N. Power-Billard, I. Manners, K. A. Leach, T. Xu, T. P. Russell, C. J. Hawker, *Adv. Mater.* **2003**, *15*, 297.

[342] M. Park, P. M. Chaikin, R. A. Register, D. H. Adamson, *Appl. Phys. Lett.* **2001**, *79*, 257.

[343] J. I. Abes, R. E. Cohen, C. A. Ross, *Chem. Mater.* **2003**, *15*, 1125.

[344] E. Michman, M. Langenberg, R. Stenger, M. Oded, M. Schvartzman, M. Müller, R. Shenhar, *ACS Appl. Mater. Interfaces* **2019**, *11*, 35247.

[345] N. Yan, X. Liu, J. Zhu, Y. Zhu, W. Jiang, *ACS Nano* **2019**, *13*, 6638.

[346] S. Kang, D. Y Ryu, E. Ringe, R. J. Hickey, S.-J. Park, *ACS Nano* **2020**, *14*, 12203.

[347] L. Wang, Y. Yang, X. Shen, T. Li, J. Hu, D. Yang, A. Dong, *Nanoscale* **2018**, *10*, 11196.

[348] A. C. Mendes, E. T. Baran, R. L. Reis, H. S. Azevedo, *WIREs Nanomed. Nanobiotechnol.* **2013**, *5*, 582.

[349] A. Popelka, J. Bhadra, A. Abdulkareem, P. Kasak, Z. Spitalsky, S. W Jang, N. Al-Thani, *Sens. Actuators, A* **2020**, *301*, 111727.

[350] S. Noh, H. Y. Gong, H. J. Lee, W.-G. Koh, *Materials* **2021**, *14*, 308.

[351] S. Zhang, W. Li, M. Elsayed, J. Peng, Y. Chen, Y. Zhang, Y. Zhang, M. Shayegannia, W. Dou, T. Wang, Y. Sun, N. P. Kherani, S. L. Neale, A. R. Wheeler, *Small* **2021**, *17*, 2103702.

[352] X. Li, L. Chen, Y. Ma, D. Weng, Z. Li, L. Song, X. Zhang, G. Yu, J. Wang, *Adv. Funct. Mater.* **2022**, *32*, 2205462.
[353] W. Wei, F. Bai, H. Fan, *Angew. Chem., Int. Ed.* **2019**, *58*, 11956.
[354] L. R. Macfarlane, H. Shaikh, J. D Garcia-Hernandez, M. Vespa, T. Fukui, I. Manners, *Nat. Rev. Mater.* **2020**, *6*, 7.
[355] Z. Hu, F. Huang, Y. Cao, *Small Methods* **2017**, *1*, 1700264.
[356] D.-S. Kim, J.-Y. Jung, S. Seo, J.-H. Kim, *Appl. Surf. Sci.* **2023**, *611*, 155756.
[357] L. Dai, P. He, S. Li, *Nanotechnology* **2003**, *14*, 1081.
[358] J. B. Edel, A. A. Kornyshev, A. R. Kucernak, M. Urbakh, *Chem. Soc. Rev.* **2016**, *45*, 1581.
[359] H. Yoshikawa, A. Hironou, Z. Shen, E. Tamiya, *ACS Appl. Mater. Interfaces* **2016**, *8*, 23932.
[360] Y. Zhang, Z. Liang, A. P Zhang, H.-Y. Tam, *Adv. Opt. Mater.* **2021**, *9*, 2001368.
[361] B. Liu, X. Lu, Z. Qiao, L. Song, Q. Cheng, J. Zhang, A. Zhang, Y. Huang, T. Chen, *Langmuir* **2018**, *34*, 13047.
[362] H. Kang, J. W. Lee, Y. Nam, *ACS Appl. Mater. Interfaces* **2018**, *10*, 6764.
[363] H. Kim, G. Kwon, C. Park, J. You, W. Park, *Micromachines* **2022**, *13*, 168.
[364] Z. Yang, J. Wei, K. Gizynski, M.-G. Song, B. A. Grzybowski, *Nat. Commun.* **2017**, *8*, 1564.
[365] V. Vieille, R. Pétrot, O. Stéphan, G. Delattre, F. Marchi, M. Verdier, O. Cugat, T. Devillers, *Adv. Mater. Technol.* **2020**, *5*, 2000535.
[366] W. Xue, T. Cui, *Sens. Actuators, A* **2007**, *136*, 510.
[367] Z. Duan, Y. Zhu, Z. Hu, J. Zhang, D. Liu, X. Luo, M. Gao, L. Lei, X. Wang, G. Zhao, *Ceram. Int.* **2020**, *46*, 27080.
[368] S. Park, J. Kwon, J. Lim, W. Shin, Y. Lee, H. Lee, H.-J. Kim, S. Han, J. Yeo, S. Ko, S. Hong, *Nanomaterials* **2018**, *8*, 645.
[369] F. Chen, W. Zhou, H. Yao, P. Fan, J. Yang, Z. Fei, M. Zhong, *Green Chem.* **2013**, *15*, 3057.
[370] T. Meng, Q.-Q. Xu, Z.-H. Wang, Y.-T. Li, Z.-M. Gao, X.-Y. Xing, T.-Z. Ren, *Electrochim. Acta* **2015**, *180*, 104.
[371] M. P. Cecchini, V. A. Turek, A. Demetriadou, G. Britovsek, T. Welton, A. A. Kornyshev, J. D. E. T. Wilton-Ely, J. B. Edel, *Adv. Opt. Mater.* **2014**, *2*, 966.
[372] H. Yockell-Lelièvre, F. Lussier, J.-F. Masson, *J. Phys. Chem. C* **2015**, *119*, 28577.
[373] Q. He, H. G. Sudibya, Z. Yin, S. Wu, H. Li, F. Boey, W. Huang, P. Chen, H. Zhang, *ACS Nano* **2010**, *4*, 3201.
[374] E. Nagelli, R. Naik, Y. Xue, Y. Gao, M. Zhang, L. Dai, *Nanotechnology* **2013**, *24*, 444010.
[375] K. Kang, D. Yang, J. Park, S. Kim, I. Cho, H-H. Yang, M. Cho, S. Mousavi, K. H. Choi, I. Park, *Sens. Actuators, B* **2017**, *250*, 574.
[376] T. Hun, Y. Liu, Y. Guo, Y. Sun, Y. Fan, W. Wang, *Microsyst. Nanoeng.* **2020**, *6*, 86.
[377] D. J. Trojanowska, G. Suarato, C. Braccia, A. Armirotti, F. Fiorentini, A. Athanassiou, G. Perotto, *ACS Appl. Nano Mater.* **2022**, *5*, 15272.
[378] J. Guo, S. Ling, W. Li, Y. Chen, C. Li, F. G. Omenetto, D. L. Kaplan, *Adv. Funct. Mater.* **2018**, *28*, 1800228.
[379] C.-C. Lin, J.-J. Chang, M.-C. Yung, W.-C. Huang, S.-Y. Chen, *ACS Biomater. Sci. Eng.* **2020**, *6*, 1144.
[380] A. Sharma, M. Thakur, M. Bhattacharya, T. Mandal, S. Goswami, *Biotechnol. Rep.* **2019**, *21*, e00316.
[381] D. Fu, D. Liu, L. Zhang, L. Sun, *Chin. Chem. Lett.* **2020**, *31*, 3195.
[382] J. Ahn, J. Ko, S. Lee, J. Yu, Y. Kim, N. L. Jeon, *Adv. Drug Delivery Rev.* **2018**, *128*, 29.
[383] Z. Wang, P. Zhang, B. Kirkland, Y. Liu, J. Guan, *Soft Matter.* **2012**, *8*, 7630.
[384] T. Burdyny, J. Riordon, C.-T. Dinh, E. H. Sargent, D. Sinton, *Nanoscale* **2016**, *8*, 2107.
[385] X. Li, K. Peng, H. Chen, Z. Wang, *Sci. Rep.* **2018**, *8*, 11663.
[386] D. M. Fragua, R. Abargues, P. J. Rodriguez-Canto, J. F. Sanchez-Royo, S. Agouram, J. P. Martinez-Pastor, *Adv. Mater. Interfaces* **2015**, *2*, 1500156.
[387] W. Luo, J. Xu, G. Li, G. Niu, K. W. Ng, F. Wang, M. Li, *Langmuir* **2022**, *38*, 7129.
[388] J. C. Huie, *Smart Mater. Struct.* **2003**, *12*, 264.
[389] C. Chen, Q. Song, W. Lu, Z. Zhang, Y. Yu, X. Liu, R. He, *RSC Adv.* **2021**, *11*, 37917.
[390] J. Li, Q.-Q. Yang, Y.-X. Hu, M.-C. Liu, C. Lu, H. Zhang, L.-B. Kong, W-W. Liu, W.-J. Niu, K. Zhao, Y.-C. Wang, F. Cheng, Z. M. Wang, Y.-L. Chueh, *ACS Sustainable Chem. Eng.* **2019**, *7*, 18375.
[391] Y. Yan, S. C. Warren, P. Fuller, B. A. Grzybowski, *Nat. Nanotechnol.* **2016**, *11*, 603.
[392] P. Xu, H. Yanagi, *Chem. Mater.* **1999**, *11*, 2626.
[393] J. Kim, I. Hwang, M. Kim, H. Jung, H. Bae, Y. Lee, *ACS Appl. Mater. Interfaces* **2022**, *14*, 5807.
[394] R. Vogel, P. Meredith, I. Kartini, M. Harvey, J. D. Riches, A. Bishop, N. Heckenberg, M. Trau, H. Rubinsztein-Dunlop, *ChemPhysChem* **2003**, *4*, 595.
[395] L. Dai, *Adv. Appl. Ceram.* **2008**, *107*, 177.
[396] F. M. Wisser, B. Schumm, G. Mondin, J. Grothe, S. Kaskel, *J. Mater. Chem. C* **2015**, *3*, 2717.
[397] T. W. Nam, M. Kim, Y. Wang, G. Y. Kim, W. Choi, H. Lim, K. M. Song, M.-J. Choi, D. Y. Jeon, J. C. Grossman, Y. S. Jung, *Nat. Commun.* **2020**, *11*, 3040.
[398] V. L. Colvin, M. C. Schlamp, A. P. Alivisatos, *Nature* **1994**, *370*, 354.
[399] A. P. Alivisatos, *Science* **1996**, *271*, 933.
[400] Y. Shu, X. Lin, H. Qin, Z. Hu, Y. Jin, X. Peng, *Angew. Chem.* **2020**, *132*, 22496.
[401] in *Nano-Optoelectronics* (Ed: M. Grundmann), Springer, Berlin Heidelberg, Berlin, Heidelberg **2002**.
[402] S. A. Abbasi, Z. Chai, A. Busnaina, *Adv. Mater. Interfaces* **2019**, *6*, 1900898.
[403] Y. S. Zhao, H. Fu, A. Peng, Y. Ma, D. Xiao, J. Yao, *Adv. Mater.* **2008**, *20*, 2859.
[404] N. Maity, R. Ghosh, A. K. Nandi, *Langmuir* **2018**, *34*, 7585.
[405] M. M. Stylianakis, *Nanomaterials* **2020**, *10*, 520.
[406] L. Wang, M. Hasanzadeh Kafshgari, M. Meunier, *Adv. Funct. Mater.* **2020**, *30*, 2005400.
[407] I. Tokarev, S. Minko, *Soft Matter.* **2012**, *8*, 5980.
[408] V. G. Kravets, A. V. Kabashin, W. L. Barnes, A. N. Grigorenko, *Chem. Rev.* **2018**, *118*, 5912.
[409] Y. Zhang, Q. Liu, H. Mundoor, Y. Yuan, I. I. Smalyukh, *ACS Nano* **2015**, *9*, 3097.
[410] H. Qi, T. Hegmann, *ACS Appl. Mater. Interfaces* **2009**, *1*, 1731.
[411] J. Prakash, A. Kumar, S. Chauhan, *Liquids* **2022**, *2*, 50.
[412] Q. Zhou, J. G. Park, J. Bae, D. Ha, J. Park, K. Song, T. Kim, *Adv. Mater.* **2020**, *32*, 2001467.
[413] J. Siminska-Stanny, M. Niziol, P. Szymczyk-Ziółkowska, M. Brozyna, A. Junka, A. Shavandi, D. Podstawczyk, *Addit. Manuf.* **2022**, *49*, 102506.
[414] D. Ravichandran, R. J. Ahmed, R. Banerjee, M. Ilami, H. Marvi, G. Miquelard-Garnier, Y. Golan, K. Song, *J. Mater. Chem. C* **2022**, *10*, 13762.
[415] N. M. Pinkerton, M. E. Gindy, V. L. Calero-Ddelc, T. Wolfson, R. F. Pagels, D. Adler, D. Gao, S. Li, R. Wang, M. Zevon, N. Yao, C. Pacheco, M. J. Therien, C. Rinaldi, P. J. Sinko, R. K. Prud'homme, *Adv. Healthcare Mater.* **2015**, *4*, 1376.
[416] M. Mayer, M. Tebbe, C. Kuttner, M. J. Schnepf, T. A. F. König, A. Fery, *Faraday Discuss.* **2016**, *191*, 159.
[417] C. Velez, I. Torres-Díaz, L. Maldonado-Camargo, C. Rinaldi, D. P. Arnold, *ACS Nano* **2015**, *9*, 10165.
[418] G. Doria, J. Conde, B. Veigas, L. Giestas, C. Almeida, M. Assunção, J. Rosa, P. V. Baptista, *Sensors* **2012**, *12*, 1657.

[419] S. Zeng, K.-T. Yong, I. Roy, X.-Q. Dinh, X. Yu, F. Luan, *Plasmonics* **2011**, *6*, 491.
[420] P. Tan, H. Li, J. Wang, S. C. B. Gopinath, *Biotechnol. Appl. Biochem.* **2020**, *68*, 1236.
[421] Y. Li, H. J. Schluesener, S. Xu, *Gold Bull* **2010**, *43*, 29.
[422] M. A Ali, C. Hu, S. Jahan, B. Yuan, M. S. Saleh, E. Ju, S.-J. Gao, R. Panat, *Adv. Mater.* **2021**, *33*, 2006647.
[423] S. Dragonieri, M. P. Van Der Schee, T. Massaro, N. Schiavulli, P. Brinkman, A. Pinca, P. Carratú, A. Spanevello, O. Resta, M. Musti, P. J. Sterk, *Lung Cancer* **2012**, *75*, 326.
[424] Y. Gao, C. Yan, H. Huang, T. Yang, G. Tian, D. Xiong, N. Chen, X. Chu, S. Zhong, W. Deng, Y. Fang, W. Yang, *Adv. Funct. Mater.* **2020**, *30*, 1909603.
[425] N. Abid, A. M. Khan, S. Shujait, K. Chaudhary, M. Ikram, M. Imran, J. Haider, M. Khan, Q. Khan, M. Maqbool, *Adv. Colloid Interface Sci.* **2022**, *300*, 102597.
[426] Z. Cai, Z. Li, S. Ravaine, M. He, Y. Song, Y. Yin, H. Zheng, J. Teng, A. Zhang, *Chem. Soc. Rev.* **2021**, *50*, 5898.
[427] L. Wang, C. Gong, X. Yuan, G. Wei, *Nanomaterials* **2019**, *9*, 285.
[428] Y. Yang, X. Li, M. Chu, H. Sun, J. Jin, K. Yu, Q. Wang, Q. Zhou, Y. Chen, *Sci. Adv.* **2019**, *5*, eaau9490.
[429] S. Pujals, N. Feiner-Gracia, P. Delcanale, I. Voets, L. Albertazzi, *Nat. Rev. Chem.* **2019**, *3*, 68.
[430] J. Zhang, Q. Liu, W. Wu, J. Peng, H. Zhang, F. Song, B. He, X. Wang, H. H.-Y. Sung, M. Chen, B. S. Li, S. H. Liu, J. W. Y. Lam, B. Z. Tang, *ACS Nano* **2019**, *13*, 3618.
[431] L. Yao, Z. Ou, B. Luo, C. Xu, Q. Chen, *ACS Cent. Sci.* **2020**, *6*, 1421.
[432] E. O. Fetisov, J. I. Siepmann, *J. Phys. Chem. B* **2016**, *120*, 1972.
[433] N. Martsinovich, A. Troisi, *J. Phys. Chem. C* **2010**, *114*, 4376.
[434] J. N. Israelachvili, *Intermolecular and Surface Forces*, Elsevier, Academic Press, Amsterdam **2011**.
[435] Z. Shou, G. A. Buxton, A. C. Balazs, *Compos. Interfaces* **2003**, *10*, 343.
[436] F. Schulz, I. Lokteva, W. J. Parak, F. Lehmkühler, *Part. Part. Syst. Charact.* **2021**, *38*, 2100087.
[437] L. Zhang, J. Lin, S. Lin, *Macromolecules* **2007**, *40*, 5582.
[438] E. V. Amadi, A. Venkataraman, C. Papadopoulos, *Nanotechnology* **2022**, *33*, 132001.
[439] B. Bao, J. Jiang, F. Li, P. Zhang, S. Chen, Q. Yang, S. Wang, B. Su, L. Jiang, Y. Song, *Adv. Funct. Mater.* **2015**, *25*, 3286.
[440] N. A. Abu Hatab, J. M. Oran, M. J. Sepaniak, *ACS Nano* **2008**, *2*, 377.
[441] X. Ke, B. Lu, J. Hao, J. Zhang, H. Qiao, Z. Zhang, C. Xing, W. Yang, B. Zhang, J. Tang, *ChemPhysChem* **2012**, *13*, 3786.
[442] K. Varaprasad, C. Karthikeyan, M. M. Yallapu, R. Sadiku, *Int. J. Biol. Macromol.* **2022**, *212*, 561.
[443] H. Ravanbakhsh, G. Bao, Z. Luo, L. G. Mongeau, Y. S Zhang, *ACS Biomater. Sci. Eng.* **2021**, *7*, 4009.
[444] D. Ravichandran, W. Xu, S. Jambhulkar, Y. Zhu, M. Kakarla, M. Bawareth, K. Song, *ACS Appl. Mater. Interfaces* **2021**, *13*, 52274.
[445] Z. Li, Q. Fan, Y. Yin, *Chem. Rev.* **2022**, *122*, 4976.
[446] J. Ren, Y. Wang, Y. Yao, Y. Wang, X. Fei, P. Qi, S. Lin, D. L. Kaplan, M. J. Buehler, S. Ling, *Chem. Rev.* **2019**, *119*, 12279.
[447] Z. Liu, Z. Zhang, R. O. Ritchie, *Adv. Funct. Mater.* **2020**, *30*, 1908121.
[448] Y. Zhao, Z. Zhang, Z. Pan, Y. Liu, *Exploration* **2021**, *1*, 20210089.
[449] A. Levin, T. A. Hakala, L. Schnaider, G. J. L. Bernardes, E. Gazit, T. P. J. Knowles, *Nat. Rev. Chem.* **2020**, *4*, 615.
[450] Q. Gao, P. Pan, G. Shan, M. Du, *Macromol. Mater. Eng.* **2021**, *306*, 2100379.
[451] Y. Lin, C. Zhang, W. Tang, Z. Jiao, J. Wang, W. Wang, Y. Zhong, P. Zhu, Y. Hu, H. Yang, J. Zou, *Adv. Sci.* **2021**, *8*, 2102539.
[452] Y. S. Lui, W. T. Sow, L. P. Tan, Y. Wu, Y. Lai, H. Li, *Acta Biomater.* **2019**, *92*, 19.
[453] M. Hwang, S. Jo, J.-W. Baek, W. Lee, K.-Y. Jung, H. Lee, B. Yeom, *Adv. Opt. Mater.* **2023**, 2300045.
[454] F. Pfeiffer, N. M. Felix, C. Neuber, C. K. Ober, H.-W. Schmidt, *Adv. Funct. Mater.* **2007**, *17*, 2336.
[455] H. Ikeda, S. Fujino, T. Kajiwara, *J. Am. Ceram. Soc.* **2011**, *94*, 2319.
[456] R. Deng, H. Li, J. Zhu, B. Li, F. Liang, F. Jia, X. Qu, Z. Yang, *Macromolecules* **2016**, *49*, 1362.
[457] H. Duan, T. Malesky, J. Wang, C.-H. Liu, H. Tan, M.-P. Nieh, Y. Lin, J. He, *Nanoscale* **2022**, *14*, 7364.
[458] D. T. Thanh Le, D. D Trung, N. D. Chinh, B. T. Thanh Binh, H. S. Hong, N. Van Duy, N. D. Hoa, N. Van Hieu, *Curr. Appl. Phys.* **2013**, *13*, 1637.
[459] C.-A. Fustin, G. Glasser, H. W. Spiess, U. Jonas, *Adv. Mater.* **2003**, *15*, 1025.
[460] A. Capitaine, M. Bochet-Modaresialam, P. Poungsripong, C. Badie, V. Heresanu, O. Margeat, L. Santinacci, D. Grosso, E. Garnett, B. Sciacca, *ACS Nano* **2023**, *17*, 9361.
[461] S. Jambhulkar, D. Ravichandran, B. Sundaravadivelan, K. Song, *J. Mater. Chem. C* **2023**, *11*, 4333.
[462] Q. Ngo, B. A. Cruden, A. M. Cassell, G. Sims, M. Meyyappan, J. Li, C. Y. Yang, *Nano Lett.* **2004**, *4*, 2403.
[463] A. Nisar, H. Hapuarachchi, L. Lermusiaux, J. H. Cole, A. M. Funston, *ACS Appl. Nano Mater.* **2022**, *5*, 3213.
[464] S. Cao, J. Shao, L. K. E. A. Abdelmohsen, J. C. M. Van Hest, *Aggregate* **2022**, *3*, https://doi.org/10.1002/agt2.128.
[465] E. Saleh, P. Woolliams, B. Clarke, A. Gregory, S. Greedy, C. Smartt, R. Wildman, I. Ashcroft, R. Hague, P. Dickens, C. Tuck, *Addit. Manuf.* **2017**, *13*, 143.
[466] M. Magro, F. Vianello, *Nanomaterials* **2019**, *9*, 1608.
[467] K. Deng, Z. Luo, L. Tan, Z. Quan, *Chem. Soc. Rev.* **2020**, *49*, 6002.
[468] W. Zhao, Y. Yan, X. Chen, T. Wang, *The Innovation* **2022**, *3*, 100253.
[469] A. Elsaidy, J. P. Vallejo, V. Salgueiriño, L. Lugo, *J. Mol. Liq.* **2021**, *344*, 117727.
[470] L. Qiu, N. Zhu, Y. Feng, E. E. Michaelides, G. Zyla, D. Jing, X. Zhang, P. M. Norris, C. N. Markides, O. Mahian, *Phys. Rep.* **2020**, *843*, 1.

Sayli Jambhulkar is a graduated Ph.D. student from Arizona State University (ASU) in System Engineering. Currently, she is working as Pathfinding Packaging R&D Engineer at Intel Corporation, Chandler. Dr. Jambhulkar's research interests include 3D printing, nanoparticle alignment, surface micropatterning, and advanced semiconductor packaging. Sayli Jambhulkar has been recipient of Excellence in Graduate Polymer Research Award by American Chemical Society (ACS) 2022, TPS PhD Completion Fellowship Award for Fall 2022 ($ 12100), and Outstanding Graduate Research Award by Graduate and Professional Association (GPSA) ASU for Spring 2022.

Kenan Song is currently holding an Associate Professor position at the University of Georgia (UGA) and is affiliated with Arizona State University. Dr. Song's research interest includes the processing-structure-property relationships, especially advanced manufacturing, characterization, simulation, and application of polymer-based nanoparticle-filled composites for energy, sustainability, health, and smart systems. Kenan Song has been the recipient of the NSF CAREER Award (2022), ACS PMSE Young Investigator Award (2022), SAMPE North America Young Professionals Emerging Leadership Award (YPELA) (2022), and, DHS New Investigator Award (NIA).